

Comparison of hyperpolarization techniques for ultralow-field magnetic resonance

Dissertation

der Mathematisch-Naturwissenschaftlichen Fakultät
der Eberhard Karls Universität Tübingen
zur Erlangung des Grades eines
Doktors der Naturwissenschaften
(Dr. rer. nat.)

vorgelegt von
Paul Fehling
aus Tübingen

Tübingen
2021

Gedruckt mit Genehmigung der Mathematisch-Naturwissenschaftlichen Fakultät der Eberhard Karls Universität Tübingen.

Tag der mündlichen Qualifikation:

28.03.2022

Dekan:

Prof. Dr. Thilo Stehle

1. Berichterstatter:

Prof. Dr. Klaus Scheffler

2. Berichterstatter:

Prof. Dr. Dr. Fritz Schick

Contents

Abbreviations and Symbols	iii
1 Zusammenfassung	1
2 Summary	2
3 List of summarized publications	3
4 Personal contributions	4
5 Introduction	6
5.1 Nuclear magnetic resonance	6
5.2 Ultralow-field magnetic resonance	7
5.2.1 High-field magnetic resonance	7
5.2.2 Ultralow-field challenges	7
5.2.3 Ultralow-field benefits and achievements	8
5.3 Hyperpolarization	8
5.3.1 Signal amplification by reversible exchange	9
5.3.2 Overhauser dynamic nuclear polarization	10
6 Objectives	12
7 Results and discussion	13
7.1 Summary of publication 1	13
7.2 Summary of publication 2	16
7.3 Summary of publication 3	20
7.4 Summary of publication 4	22
7.5 Discussion of results	27
8 Conclusion and outlook	30
8.1 Conclusion	30
8.2 Outlook	31
Acknowledgements	32
Bibliography	33
Appendix	37

Abbreviations and Symbols

Abbreviations

AM	atomic magnetometer
AUP	area under peak
COSY	correlation spectroscopy
DNP	dynamic nuclear polarization
d-DNP	dissolution dynamic nuclear polarization
FID	free induction decay
LAC	level anticrossing
MR	magnetic resonance
MRI	magnetic resonance imaging
MRS	magnetic resonance spectroscopy
NMR	nuclear magnetic resonance
ODNP	Overhauser dynamic nuclear polarization
oH_2	ortho-hydrogen
OMRI	Overhauser enhanced magnetic resonance imaging
PHIP	para-hydrogen induced polarization
pH_2	para-hydrogen
QC	quantum coherence
RF	radiofrequency
SABRE	signal amplification by reversible exchange
alt-SABRE	alternating signal amplification by reversible exchange
SABRE-SHEATH	SABRE in shield enables alignment transfer to heteronuclei
CASH-SABRE	catalyst-separated hyperpolarization via SABRE
SNR	signal-to-noise ratio
SQUID	superconducting quantum interference device
ULF	ultralow-field
3FP	3-fluoropyridine

Symbols / parameters

B_p	magnetic prepolarization field
B_0	external magnetic field, precession field
B_1	alternating excitation field
E	signal enhancement
E_{\max}	maximum enhancement
f	leakage factor (ODNP)
$FWHM$	full width at half maximum, linewidth of spectral peaks
G_x, G_y	magnetic field gradients in x- or y-direction (for phase encoding)
G_z	magnetic field gradient in z-direction (for frequency encoding)
I	nuclear spin
\vec{M}, M	sample magnetization
MW	molecular weight
P	Power
$P_{1/2}$	half-power, RF-power needed to reach half of E_{\max} (ODNP)
p	spin polarization
S	electron spin
S_g	total spin of two spin system
$ S_0\rangle$	singlet state
s	saturation of the electron spin transision (ODNP)
$S_B^{1/2}$	magnetic field noise
s_{\max}	maximum saturation at the limit of $P \rightarrow \infty$ (ODNP)
t_{Bp}	prepolarization time
T_{HP}	hyperpolarization buildup time
t_1	evolution time of COSY sequence
T_1	longitudinal relaxation time
$T_{1,0}$	longitudinal relaxation time of sample without spin probes (ODNP)
T_2	transverse relaxation time
$ T_-\rangle, T_0\rangle, T_+\rangle$	triplet state substates
V_Φ	SQUID assembly transfer function (voltage)
W	transition probability
$ \alpha\rangle, \beta\rangle$	Zeeman basis spin states
$\gamma, \gamma_e, \gamma_H$	gyromagnetic ratio (general / of electrons / of protons)
ξ	coupling factor (ODNP)
Φ_0	magnetic flux quantum
$\varphi_1, \varphi_2, \varphi_{rec}$	variable phases of COSY sequence
$\omega_0, \omega_e, \omega_H$	Larmor frequency (general / of electrons / of protons)

1 Zusammenfassung

Magnetresonanzuntersuchungen (MR-Untersuchungen) sind in einer Vielzahl von Anwendungen verbreitet. Beispielsweise bietet MR-Spektroskopie (MRS) eine Möglichkeit zur zerstörungsfreien Strukturanalyse und MR-Tomographie (MRI) ist ein gängiges medizinisches Bildgebungsverfahren. Konventionelle MR-Systeme sind teuer und sperrig, da sie große Magnetspulen nutzen, um hohe Felder und Signalamplituden zu erzeugen. Das hier vorgestellte Projekt vereint einen Ultraniederfeld-Ansatz (ULF-Ansatz) mit zwei signalverstärkenden Methoden, um diese Probleme zu umgehen.

Zuerst wurde das experimentelle ULF-MR-Setup mit seinem offenen Spulensystem aufgebaut und getestet. Ein supraleitendes Quanteninterferometer (SQUID) als Sensor ermöglicht die quantitative Messung des MR-Signals. Experimente mit SABRE-basierter (Signal Amplification By Reversible Exchange) MRS und ODNP-verstärkter (Overhauser Dynamic Nuclear Polarization) MRI wurden durchgeführt. Die Ergebnisse zeigen zukünftige Anwendungen auf und betonen den gegenseitigen Nutzen: Der ULF-Ansatz profitiert von der Signalverstärkung. Gleichzeitig tragen die Versuche zur genaueren Untersuchung und Weiterentwicklung der Hyperpolarisationsmethoden bei.

Als Nächstes wurden simultane Messungen von SABRE-verstärkten Fluor- und Protonensignalen durchgeführt und der Einfluss verschiedener Messparameter auf die Hyperpolarisation untersucht. Mithilfe von Korrelationsspektroskopie wurde der SABRE-Polarisationstransfer weiter erforscht. Die Studien zeigen die vielfältigen Einsatzmöglichkeiten des Systems auf und weisen die Hyperpolarisation von Mehrfach-Spin-Zuständen durch SABRE nach.

Der letzte Teil der Arbeit konzentrierte sich auf die ODNP-Methode. Freie Radikale wurden genutzt, um die Kernspinpolarisation zu erhöhen und das MR-Signal zu verstärken. In einer breit angelegten Studie wurden die ODNP-bezogenen Eigenschaften verschiedener Nitroxidradikale charakterisiert, was die Untersuchung der Zusammenhänge zwischen chemisch-physikalischen Attributen und den Hyperpolarisationseigenschaften der Radikale ermöglichte. Die Ergebnisse bilden einen Katalog hyperpolarisierender Kontrastmittel und können in Zukunft als Referenz für die Auswahl oder Weiterentwicklung freier Radikale dienen, besonders in Bezug auf deren Funktionalisierung im biologischen Kontext.

In der Einordnung der Ergebnisse werden die mögliche Anwendung und die zukünftige Ausrichtung der Forschung für beide Hyperpolarisationsmethoden diskutiert. Während sich die Anwendungsmöglichkeiten stark unterscheiden, versprechen beide Ansätze eine erhebliche Verbesserung von Signalstärke und Kontrast für Magnetresonanzuntersuchungen in ultraniederen und höheren Magnetfeldern.

2 Summary

Magnetic resonance (MR) studies are well established in numerous industrial, medical and scientific applications. Examples include MR spectroscopy (MRS), which is utilized for non-destructive chemical analysis, and MR imaging (MRI), which is a common non-invasive, medical imaging technique with great contrast in soft tissue. Conventional systems are bulky and expensive, because large magnet coils are utilized to generate high magnetic fields and signal amplitudes. The project presented in this thesis seeks to address these issues by combining the use of ultralow magnetic fields (ULF), with two signal enhancing hyperpolarization techniques.

First, the experimental ULF-MR setup was established. It employs an open magnet coil assembly in combination with a superconducting quantum interference device (SQUID) as sensor, allowing for the quantitative measurement of the MR signal. Spectroscopic signal amplification by reversible exchange (SABRE) experiments and Overhauser dynamic nuclear polarization (ODNP) enhanced MRI showcased the successful implementation of these hyperpolarization techniques, and the imaging capabilities of the system. The results outline future applications and emphasize how the ultralow-field approach benefits from enhanced signal amplitude by hyperpolarization methods, while in turn facilitating the investigation and refinement of these techniques.

Next, the simultaneous SABRE enhanced measurement of fluor and proton spins was performed. After investigating the influence of some measurement parameters on signal enhancement, correlation spectroscopy was utilized for a more detailed examination of the polarization transfer mechanisms. The studies demonstrated the capability of the system to perform multinuclear correlation spectroscopy experiments and the results are proof for the hyperpolarization of multiple-spin states by SABRE.

The last part of this thesis focused on ODNP. With this technique, free radicals can facilitate an increase in nuclear spin polarization, enhancing the MR signal. Here, the polarization transfer efficacy of a broad range of nitroxide radicals was characterized. The comprehensive study allowed for a correlation of chemico-physical features with hyperpolarization-related properties. The results provide a catalog of polarizing agents and give direction for predicting and optimizing free radical performance in the future, especially for the development of functionalized polarizing agents.

Reviewing the results allowed for a discussion of future utilization and direction of research for both hyperpolarization techniques. While possible applications differ greatly, they both share the prospect of profoundly enhancing MR signal and contrast in not only ultralow-fields but also in higher field regimes.

3 List of summarized publications

Publication 1

K. Buckenmaier, M. Rudolph, **P. Fehling**, T. Steffen, C. Back, R. Bernard, R. Pohmann, J. Bernarding, R. Kleiner, D. Kölle, M. Plaumann, K. Scheffler

Mutual benefit achieved by combining ultralow-field magnetic resonance and hyperpolarizing techniques

Review of Scientific Instruments, 89(12), 125103 (2018)

DOI: 10.1063/1.5043369

Publication 2

K. Buckenmaier, M. Rudolph, C. Back, T. Misztal, U. Bommerich, **P. Fehling**, D. Kölle, R. Kleiner, H. A. Mayer, K. Scheffler, J. Bernarding, M. Plaumann

SQUID-based detection of ultra-low-field multinuclear NMR of substances hyperpolarized using signal amplification by reversible exchange

Scientific reports, 7(1), 1-9 (2017)

DOI: 10.1038/s41598-017-13757-7

Publication 3

K. Buckenmaier, K. Scheffler, M. Plaumann, **P. Fehling**, J. Bernarding, M. Rudolph, C. Back, D. Kölle, R. Kleiner, J. B. Hövener, A. N. Pravdivtsev

Multiple Quantum Coherences Hyperpolarized at Ultra-Low Fields

ChemPhysChem, 20(21), 2823 (2019)

DOI: 10.1002/cphc.201900757

Publication 4

P. Fehling, K. Buckenmaier, S. A. Dobrynin, D. A. Morozov, Y. F. Polienko, Y. V. Khoroshunova, Y. Borozdina, P. Mayer, J. Engelmann, K. Scheffler, G. Angelovski, I. A. Kirilyuk

The effects of nitroxide structure upon ¹H Overhauser dynamic nuclear polarization efficacy at ultralow-field

The Journal of Chemical Physics, 155(14), 144203 (2021)

DOI: 10.1063/5.0064342

4 Personal contributions

Publication 1

K. Buckenmaier and M. Rudolph designed and constructed the SQUID-detection setup, the ULF-NMR system and the pH_2 reaction chamber setup. They wrote most of the manuscript. T. Steffen built the current source for the frequency encoding gradient. C. Back built the parahydrogen generator. R. Bernard, and R. Pohmann assisted with the *ex vivo* measurements. J. Bernarding helped with supplying chemicals and advised on the pH_2 experiments. R. Kleiner and D. Kölle advised on the SQUID based detection setup. M. Plaumann helped with supplying chemicals and with performing pH_2 experiments. K. Scheffler advised on the MR setup and NMR measurement scheme. K. Buckenmaier and I took part in performing all pH_2 and *ex vivo* ODNP measurements. I designed and constructed all gradient coils and the prepolarization coil, wrote parts of the data reconstruction software and took part in writing the manuscript.

Publication 2

K. Buckenmaier and M. Rudolph designed and constructed the SQUID-detection setup, the ULF-NMR system and the pH_2 reaction chamber. D. Koelle, R. Kleiner advised on the SQUID setup. C. Back designed and built the parahydrogen generator. U. Bommerich, T. Misztal, H. A. Mayer, J. Bernarding and M. Plaumann were involved in supplying the chemicals. K. Scheffler advised on the MRS scheme. K. Buckenmaier, M. Plaumann wrote most of the manuscript. K. Buckenmaier, M. Plaumann and I performed all measurements. I wrote software for the MRS data reconstruction and took part in its evaluation.

Publication 3

K. Buckenmaier and M. Rudolph designed and constructed the SQUID-detection setup, the ULF-NMR system and the pH_2 reaction chamber. K. Scheffler advised on the MRS scheme. M. Plaumann and J. Bernarding supplied the chemicals. C. Back designed and built the parahydrogen generator. D. Koelle and R. Kleiner advised on the SQUID setup. J. B. Hövener and A. N. Pravdivtsev were responsible for the simulations. K. Buckenmaier and A. N. Pravdivtsev wrote most of the manuscript and K. Buckenmaier, M. Plaumann and I performed the experiments and evaluated the data.

Publication 4

S. A. Dobrynin, D. A. Morozov, Y. F. Polienko, Y. V. Khoroshunova, Y. Borzdina, G. Angelovski and I. Kirilyuk synthesized and prepared most of the chemicals. J. Engelmann and I. Kirilyuk advised on sample preparation and interpretation of the results. K. Scheffler advised on the MR setup. K. Buckenmaier and P. Mayer performed some of the measurements and helped with data evaluation. K. Buckenmaier and I. Kirilyuk wrote parts of the manuscript. I performed most of the measurements, evaluated the datasets and wrote the majority of the manuscript.

5 Introduction

This chapter introduces the reader to some selected basic concepts of nuclear magnetic resonance, the two hyperpolarization methods used in this work, as well as the concept of ultralow-field magnetic resonance and tries to outline the current state of the respective research fields.

5.1 Nuclear magnetic resonance

In magnetic resonance (MR) experiments on paramagnetic samples in an external magnetic field B_0 , the sample magnetization \vec{M} gives rise to the measured signal. It relates to the spin polarization p , which results from the populations of the two Zeeman eigenstates $|\alpha\rangle$ and $|\beta\rangle$ of the observed spins. In thermal equilibrium, the magnetization aligns with the external field, and its magnitude additionally depends on the gyromagnetic ratio γ of the observed spins:

$$|\vec{M}| \propto \gamma p \propto \gamma^2 B_0 \quad (5.1)$$

If \vec{M} is deflected from the equilibrium orientation, it will precess around the field axis with the Larmor frequency $\omega_0 = -\gamma B_0$ and will regain its equilibrium state on a timescale described by the longitudinal and transverse relaxation times T_1 and T_2 .

Such deflection from the field direction can be achieved by a radiofrequency pulse B_1 , matching the respective Larmor frequency. Additional spatial information can be encoded by employing magnetic field gradients.

The most prominent applications of magnetic resonance are magnetic resonance spectroscopy (MRS), where information about the types of spins within a given sample is extracted, and magnetic resonance imaging (MRI) where multidimensional imaging of samples, subjects or patients is performed.

For a more profound introduction to nuclear magnetic resonance (NMR), Levitt provides an extensive discussion of spin dynamics and Brown et al. describe the principles and methods of magnetic resonance imaging in great detail. This short summary follows their descriptions.[1, 2]

5.2 Ultralow-field magnetic resonance

5.2.1 High-field magnetic resonance

Equation 5.1 elucidates the linear field dependency of the signal generating quantity $|\dot{M}|$. The induction coils commonly used for signal detection in high-field MR measure the time derivative of the magnetization. In this case the additional dependency of the induced voltage on the field-dependent Larmor frequency results in a quadratic relation to the field. This highlights one of the benefits of employing high magnetic fields for magnetic resonance experiments, leading to remarkable success in clinical and research applications due to high signal intensities and spatial resolutions. However, raising the field strength also introduces technical and physical challenges. Increased system size, high costs, and susceptibility artifacts in the presence of metals are just a few high-field MR issues.[3]

5.2.2 Ultralow-field challenges

In magnetic resonance, the low-field regime is defined as $B_0 < 0.5T$ and the ultralow-field (ULF) regime as $B_0 < 10mT$. [3] As is emphasized by equation 5.1, the main challenge for MR experiments at ultralow fields is the inherently low signal to noise ratio (SNR). This problem can be tackled from three different angles. First, by increasing the magnetization, second by efficiently making use of the available signal and third by lowering the external noise in the experiment.

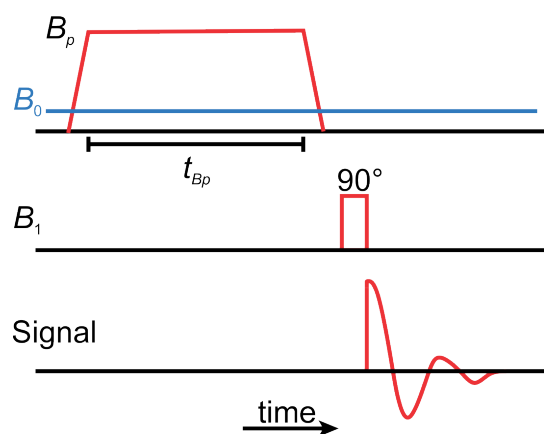


FIGURE 5.1: Schematic of a prepolarized FID sequence.

Prepolarization is a common method to artificially increase the sample magnetization in ULF-MR experiments. As figure 5.1 depicts for the case of a free induction decay (FID) sequence, the external field is increased beyond the precession field B_0 for a duration of the prepolarization time t_{B_p} and adiabatically switched off right before the actual MR pulse sequence. The time scale of the prepolarization field B_p ramp down is much shorter than longitudinal relaxation. This results in measurements with B_0 -Larmor frequencies at almost B_p -magnetization levels. Since B_p does not affect the precession of the spins, the requirements on B_p field homogeneity are lower than for B_0 , allowing for simpler coil geometries.

The next aspect for consideration is signal detection. Section 5.2.1 illustrates that a sensor with a linear relation between measurable magnetic flux density and output voltage is superior to induction coils in a low- or ultralow-field setting. Magnetometers

like superconducting quantum interference devices (SQUID) or atomic magnetometers (AM) provide this feature and especially due to their lower field noise SQUID assemblies tend to be more suited to the ULF regime than conventional Faraday induction coils.[4]

The last approach to achieving sufficient SNR is lowering the noise. Electromagnetic shielding against exterior alternating and constant fields offers a solution to this issue and gradiometric sensor configurations can additionally help reduce the influence of such remote noise sources.[3, 5] Besides external noise sources, sensor noise and sample noise also play a relevant role. Sensor noise of conventional Faraday detection coils decreases below sample or body noise levels in high field MRI applications. In the ultralow-field regime, the sensor noise usually exceeds body noise, making it the limiting factor in these settings and putting even more emphasis on sensor selection.[4]

5.2.3 Ultralow-field benefits and achievements

Multiple advantages can be achieved in ULF-MR setups, by omitting the large, superconducting magnet coils needed for field generation in high-field MR applications. The ULF-setups are much cheaper, more mobile, and their coil systems are more open compared to conventional high-field machines.[5] This also makes them more adaptive to include novel approaches and methods. Due to the low fields, susceptibility issues become negligible. Experiments in the vicinity of metals become possible [6] and compatibility with other techniques, devices and imaging modalities is improved.[7] The lower fields also allow for the use of a wider range of detectors like SQUIDs. This enables multinuclear measurements due to their broadband detection characteristics [see **publication 1** and **publication 2**]. Lastly, MRI contrast mostly relates to T_1 and T_2 relaxation times. These parameters are field dependent, thus producing a different contrast in a field range that is different to the more conventional high-field approach.[5]

Low- and ultralow-field MRI experiments have been discussed and performed since the 1980s, [8] with ongoing technological progress in recent years. Prepolarized ULF-MRI currently is a common approach with recent *in vivo* results of human and animal brain imaging. While anatomical structures are well distinguishable with spatial resolutions about of 1-4mm, the experiments yielded relatively narrow field of views and measurement duration was between 40-70 minutes.[9]

5.3 Hyperpolarization

Hyperpolarization is a state of increased nuclear spin polarization beyond the thermal equilibrium. Besides prepolarization, it offers another way to boost the MR signal. Nuclear spins can be hyperpolarized by transferring spin order from external sources such as parahydrogen, unpaired electrons or optical polarization onto the targeted nuclear spins. The numerous hyperpolarization methods include for example parahydrogen-induced polarization (PHIP) or dynamic nuclear polarization (DNP) techniques.[10] The

yield of a hyperpolarization method can be quantified by determining the resulting spin-polarization p (stated in %), or by comparing the signal amplitude of hyperpolarized with thermally polarized measurements to form the signal enhancement E . Signal amplification by reversible exchange (SABRE), a parahydrogen based approach, and Overhauser dynamic nuclear polarization (ODNP) are the two techniques used for this work. They will be described in more detail below.

Most liquid phase hyperpolarization methods need polarizing agents or polarized substrate present in the measured sample or subject. The general non-invasiveness of MRI measurements therefore is lost. However, the use of these agents or substrates offers some benefits. In addition to plain signal enhancement, their targeted distribution or functionalization can also produce specific contrast. Depending on the hyperpolarization method, target nuclear spins are not confined to ^1H -nuclei, but spins of ^{13}C , ^{15}N , ^{19}F and others can also be hyperpolarized.[10]

5.3.1 Signal amplification by reversible exchange

When two particles with spins $1/2$ combine, the total spin S_g can be $S_g = 0$ or $S_g = 1$. The $S_g = 0$ singlet state $|S_0\rangle$ does not exhibit degeneracy. In contrast, the $S_g = 1$ state has three substates $|T_-\rangle$, $|T_0\rangle$ and $|T_+\rangle$ and is therefore named triplet state.[1]

Hydrogen molecules in the triplet state are called orthohydrogen ($o\text{H}_2$). In standard laboratory conditions, the Boltzman distribution results in almost equal population of all four states. Here, $o\text{H}_2$ is more common ($\sim 75\%$), while singlet state or parahydrogen ($p\text{H}_2$) is found at only $\sim 25\%$ natural abundance. Flowing hydrogen gas through an appropriate catalyst at cryogenic temperatures can shift this distribution to $> 95\%$ $p\text{H}_2$,[11] after which the singlet states are relatively stable.[12]

PHIP techniques exploit the highly ordered spin state of $p\text{H}_2$ by transferring spin alignment to the spins of a target substrate. In hydrogenative PHIP methods, a hydrogen molecule permanently binds to the target molecule, making the process irreversible. In contrast, SABRE is a non-hydrogenative approach that employs a polarization transfer catalyst.[14] As depicted in figure 5.2, two hydrides of $p\text{H}_2$ and three substrates bind to the catalyst, where the polarization transfer can occur. It can take place, because the symmetry of the hydrides is broken by a difference in J-coupling to the substrate.[13, 14] The hyperpolarization process depends on the complex interplay of multiple spins and their J-couplings.[14] For now, let us employ a simplified model, only considering a collective state of the two $p\text{H}_2$ hydrides and one target substrate nuclear spin (e.g. protons) in a mT field range. The spin order transfer process itself is based on level anticrossings (LAC) of the collective states of

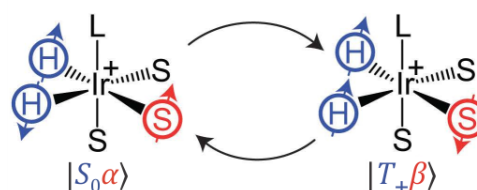


FIGURE 5.2: SABRE polarization transfer from Hydrides H (blue) via Ir^+ catalyst to target substrate S (red). Adapted from Barskiy et al. [13] with permission.

the three spins. The populations of states $|S_0\alpha\rangle$ and $|S_0\beta\rangle$ are almost equal in the beginning. If the LAC conditions (e.g. J-coupling and field strength) are met, $|S_0\alpha\rangle$ population is transferred to $|T_+\beta\rangle$, overpopulating the $|\beta\rangle$ state of the target spin, thus increasing its polarization. After the polarization transfer took place, the hydrides and the hyperpolarized substrate detach from the catalyst and the process can be repeated.

SABRE is performed by introducing $p\text{H}_2$ gas into a liquid solution that contains catalyst and substrate molecules. The method can achieve up to 10^5 -fold signal enhancements. Its possible applications are spectroscopic analysis as well as MR-imaging. While research on topics like SABRE-SHEATH (SABRE in SHield Enables Alignment Transfer to Heteronuclei)[15] aims at further improving spin polarization levels by modifying the field-cycled SABRE scheme, other groups focus more immediately on the biocompatibility of the method. Here progress has been made in terms of catalyst aqueous solubility,[16] while catalyst-separated hyperpolarization via SABRE[17] also provides a pathway towards *in vivo* applications.

5.3.2 Overhauser dynamic nuclear polarization

Overhauser dynamic nuclear polarization (ODNP) relies on the Overhauser effect,[18] predicting a polarization transfer from electron- to nuclear spins under the condition of saturating the electron spin resonance. The relation between the gyromagnetic ratios or Larmor frequencies of electron and proton spins respectively is the foundation for this approach, as $\left|\frac{\gamma_e}{\gamma_H}\right| = \left|\frac{\omega_e}{\omega_H}\right| \approx 660$. Following equation 5.1, the electron spin polarization is greater than the proton nuclear spin polarization, which turns the described polarization transfer into a tool for proton spin hyperpolarization in liquids.

The requirements for this technique are the presence of unpaired electrons together with the target substrate nuclei and the electromagnetic irradiation with a radiofrequency-pulse (RF-pulse) at the electron Larmor frequency. If the electron spin S and the target nuclear spin I are close enough for significant dipole-dipole interaction, the RF-excitation pulse will saturate the transition of the system from the ground state $|\alpha_S\alpha_I\rangle$ to $|\beta_S\alpha_I\rangle$. Cross-relaxation processes within the system will lead to transitions to the $|\beta_S\alpha_I\rangle$ and $|\beta_S\beta_I\rangle$ states (see figure 5.3), resulting in an enhancement of the nuclear spin polarization p .

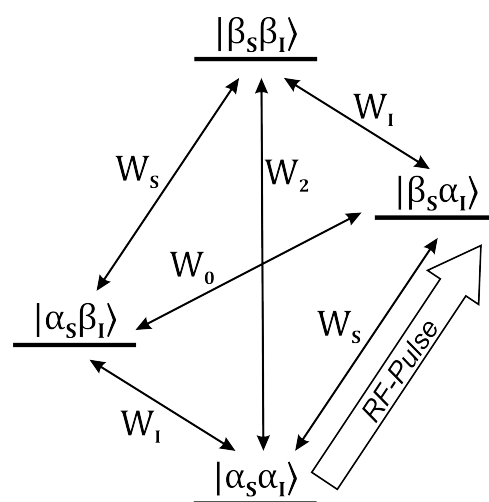


FIGURE 5.3: Four energy levels of a two-spin system with RF-excitation and transition probabilities W , as described by Solomon [19].

This enhancement is characterized by the coupling factor ξ , the leakage factor f and the saturation s of the electron transition.[20, 21] ξ relates to the type of interaction between the spins and its correlation time. The leakage factor $f = 1 - \frac{T_1}{T_{1,0}}$ depends on

longitudinal relaxation times of the sample with (T_1) and without ($T_{1,0}$) spin probes (i.e. the molecule containing the free radical). The saturation $s(P)$ depends on the power P of the excitation pulse and the electron relaxation. Together they determine the signal enhancement for a sample at a given power:

$$E(p) = 1 - \xi f \left| \frac{\omega_e}{\omega_H} \right| s(P) \quad (5.2)$$

We can introduce the maximum possible enhancement E_{\max} at unlimited power and the half-power $P_{1/2}$ needed to reach $E_{\max}/2$ for a more intuitive description of the power dependent enhancement for a given sample:

$$E(P) = \frac{(E_{\max} - 1)P}{P_{1/2} + P} + 1 \quad (5.3)$$

This power dependency is depicted in figure 5.4 together with an example of an ODNP enhanced NMR sequence to measure this relation.

In practice, the unpaired electrons are commonly supplied in the form of free radical molecules in aqueous solution. Additional intramolecular interactions and resulting hyperfine splittings for the electron spin states can further complicate the previously described two spin system, but the underlying cross-relaxation principle for the polarization transfer remains the same.[22]

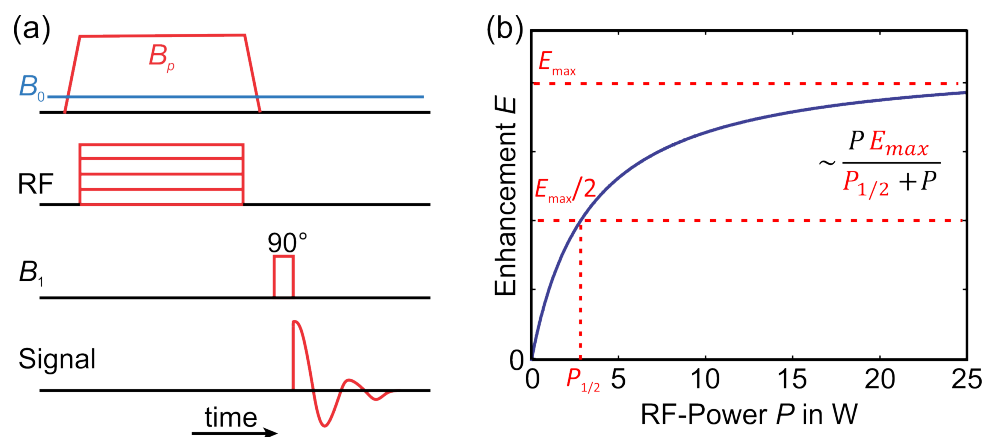


FIGURE 5.4: (a) ODNP enhanced NMR sequence, (b) power dependency of ODNP enhancement

Due to limitations on RF-pulse penetration depth, *in situ* ODNP at high fields is possible yet difficult and limited to small sample volumes.[23] To circumvent this issue, most groups employ low-field and ultralow-field MR setups, enabling the successful implementation of *in vivo* Overhauser-enhanced MRI (OMRI) on small animals.[24–27] Spin probe biocompatibility and stability poses another challenge. Recent developments either revolve around improving the OMRI methodology and instrumentation [27–29] or on spin probe design and characterization.[30–36]

6 Objectives

The main objective of the presented work was to establish an ultralow-field magnetic resonance spectroscopy and imaging setup for the investigation of hyperpolarization methods and to explore, develop and compare some of these methods.

The specific objective of **publication 1** was to provide a detailed description of the setup and its capabilities. Its capacity for multinuclear SABRE experiments, which is utilized in **publication 2** and **publication 3**, was demonstrated in two types of measurements. Most notably, features allowing for *in situ* hyperpolarization by ODNP and gradient coils enabling three-dimensional MR-imaging were constructed and tested. They were used for *ex vivo* ODNP enhanced MR imaging on a rat carcass, with the aim of proving the viability of *in vivo* OMRI experiments in the ULF-MR setup.

Besides exploring SABRE as a technique for raising the SNR at ULF, **publication 2** aimed at using the broadband detector in order to perform multinuclear NMR spectroscopy, facilitating the investigation of polarization transfer mechanisms in SABRE experiments and raising questions about the underlying processes and physical principles.

The goal of **publication 3** was to perform a more detailed investigation into the questions raised by **publication 2**. It sought clarity about the composition of SABRE spectra and two-dimensional correlation spectroscopy was implemented in SABRE experiments to investigate the hyperpolarization of multiple-spin states.

The use of free radicals enables ODNP enhanced MR experiments not only in the ULF regime. The measurements described in **publication 4** aimed at investigating the impact of the chemical features of nitroxide radicals on the ODNP polarization transfer efficacy. The goal was to better understand the hyperpolarization process, but also to create a reference for spin probe selection in future ODNP experiments. The study therefore aimed at providing a catalogue of possible radicals and giving direction for future spin probe design, especially when aiming for *in vivo* applications.

7 Results and discussion

7.1 Summary of publication 1

Mutual benefit achieved by combining ultralow-field magnetic resonance and hyperpolarizing techniques

Besides providing solutions to multiple high-field MRI problems like costs, size or susceptibility artifacts, the ultralow-field MR approach also offers the possibility of using highly sensitive broadband detectors. These sensors enable multinuclear detection schemes as well as the direct measurement of MR signal strength. Hyperpolarization techniques, such as SABRE or ODNP, offer an approach to solving the SNR issue of the ULF concept. The simplicity and high adaptability of ULF-setups facilitates the technical implementation of such hyperpolarization techniques. The ULF regime is ideal for performing SABRE and ODNP experiments. It provides the opportunity to investigate the underlying polarization transfer mechanisms and to compare the suitability of different chemicals as polarizing agents. The publication describes the technical instrumentation as well as the measurement and data analysis scheme of our SQUID-based ULF MRS and MRI setup and showcases its performance in exemplary measurements including SABRE hyperpolarized NMR-spectroscopy and ODNP enhanced MR-imaging.

The heart of the system is a SQUID-based magnetometer, containing a SQUID-based current sensor and a gradiometric pickup coil. It is placed inside a low-noise ($S_B^{1/2} \leq 0.5 \text{ fT/Hz}^{1/2}$) liquid helium dewar (Cryoton type LH-11.5-NTE) with a hot-to-cold distance of $d_{hc} = 12 \text{ mm}$ close to the sample. A superconducting second-order axial gradiometer is coupled to a Magnicon single-stage current sensor (type C6L1), producing a joint system transfer function of $V_\Phi = 0.44V/\Phi_0$ with the magnetic flux quantum Φ_0 . The SQUID electronics (Magnicon XXF-1) connect the SQUID to the computer and control the flux-locked loop during operation.

All measurement sequences are programmed through a LabVIEW based MR-sequence software. A National Instruments analog-to-digital converter / digital-to-analog converter device provides the control signals of the measurement sequence to the current sources, relays and the SQUID and is also used for data acquisition.

The system contains six different coils, depicted in figure 7.1 and described in table 7.1. Three different RF-field coils for exciting the electrons in ODNP experiments are made from single wire loops with a diameter of 30mm, which can be tuned to cover a combined resonance frequency range of 80 MHz to 250 MHz.

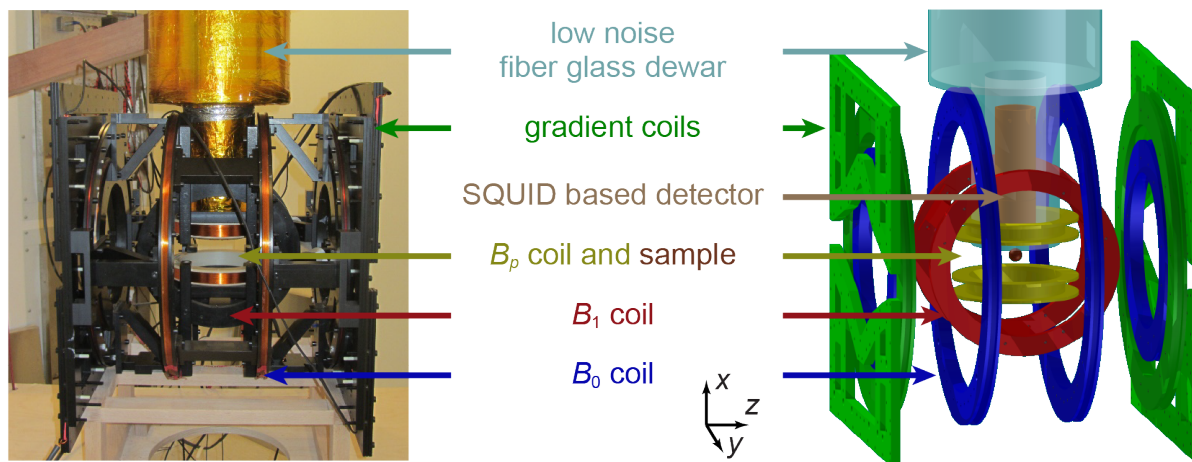


FIGURE 7.1: Photography and schematic of the coil system together with the fiberglass dewar.

field	concept	coils	turns	radius [mm]	coeff.	amplifier
B_0	Tetracoil [37]	4	80/121	161.6/248.5	0.6	HighFinesse BCS
B_1	Helmholtz	2	4	186.5	0.025	Toellner TOE 7621-60
B_p	Helmholtz	2	356	83	2.58	Kepeco BOP 100-4 ML
G_z	Maxwell	2	30		0.45	improved from ref. [38]
G_x	Planar [39]	4	20	-	0.183	Hubert A1110-16-QE
G_y	Planar [39]	4	20	-	0.183	Hubert A1110-16-QE
RF	Loop	1	1	30	-	Frankonia FLH-50A

TABLE 7.1: Coil properties of the ULF-MR coil system. Turns per coil element. Coeff. in mT/A (field coils "B") or mT/Am (gradient coils "G").

The SQUID and the coil system are set inside a multilayered shielding chamber (Vacuumschmelze, Vacoshield magnetically shielded room), to reduce the impact of noise from constant and alternating external fields. In order to reduce unwanted current noise from the amplifiers, mechanical relays and feedthrough low-pass filters (Tesch 02000203 and Tesch 02000207) are employed on all coils. The dewar is wrapped in silver plated mylar foil to shield the SQUID from the RF-pulses necessary for ODNP-excitation.

SABRE measurements require a constant supply of pH_2 , which is provided by a pH_2 -generator with a dip-stick design. When cooling the catalyst cartridge to temperatures just above 21K it can achieve pH_2 concentrations $\geq 90\%$. To produce continuous hyperpolarization, the pH_2 is introduced into a specifically designed hyperpolarization chamber through an inlet at the bottom of the chamber. It can escape through an outlet at the top, leading to a liquid collection basin, from which any escaped liquid is fed back into the chamber, prolonging refilling intervals.

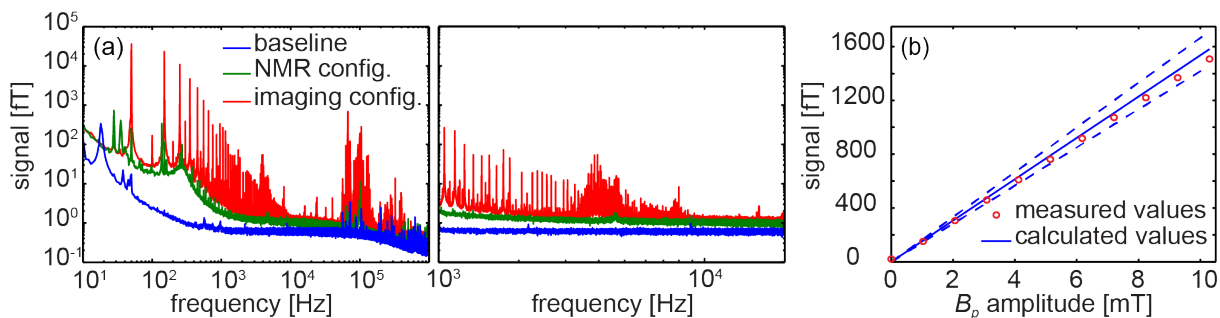


FIGURE 7.2: (a) Noise spectra of the system for different system configurations (b) Comparison of MR signal strength [fT] in experiment (red) and calculation (blue), including sample offsets of $\pm 1\text{mm}$ (dashed)

The magnetic field noise level in the range of interest above 5kHz strongly depends on the system configuration during operation, as presented in figure 7.2(a). The noise level of the gradiometric SQUID assembly alone is $S_B^{1/2} \approx 0.6 \text{ fT/Hz}^{1/2}$ and with coils in place it is raised to $S_B^{1/2} \approx 1.1 \text{ fT/Hz}^{1/2}$. The B_0 current source and the B_p , B_1 , G_x and G_y amplifiers do not affect the noise significantly in the region of interest due to relays and filters. The G_z amplifier increases the noise level to $S_B^{1/2} \approx 1.4 \text{ fT/Hz}^{1/2}$ during operation.

The SQUID-based unit enables quantitative measurements of the MR-signal in fT. Figure 7.2(b) demonstrates, that exemplary measurements on a water phantom matched the calculated values for this sample.

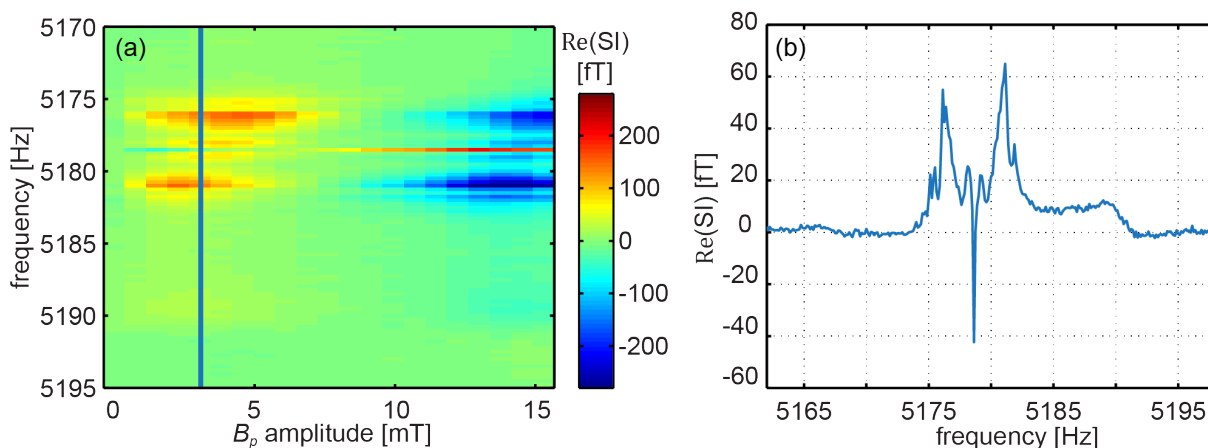


FIGURE 7.3: (a) B_p dependency of SABRE-enhanced 3-fluoropyridine spectra (b) high-resolution spectrum at $B_p = 3\text{mT}$ (blue line in (a))

To showcase the SABRE capabilities, two kinds of measurements were performed on a 3-fluoropyridin (3FP) sample with a Crabtree catalyst. Varying the B_p amplitude of a prepolarized FID sequence (see fig. 5.1) yields the B_p -dependency of the spectra as depicted in fig. 7.3(a). A single high-resolution spectrum at fixed $B_p = 3 \text{ mT}$ is also

presented in fig 7.3(b), achieving a spectral resolution < 0.5 Hz. These measurements give an example for the different types of SABRE-based measurements the system is capable of performing.

To prove the feasibility of future *in vivo* ODNP experiments, we present results, where carboxy proxyl radicals were injected into a rat carcass, allowing for *ex vivo* ODNP-enhanced imaging at ultralow fields. The acquisition of these three-dimensional images with isotropic 1mm resolution with 37×37 phase encoding steps took 60 minutes. The anatomical structure fits well to comparison measurements from a commercial 3T MRI scanner.

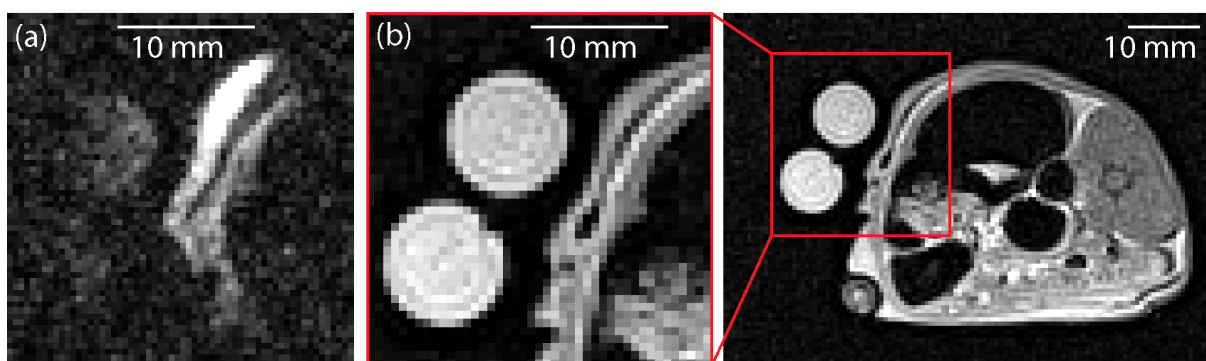


FIGURE 7.4: *Ex vivo* MR-images of a rat, taken (a) with ODNP enhancement in the ULF-MRI system (b) in a commercial 3T MRI-scanner.

In this publication we showcased the capability of the SQUID based ULF-MRI perform various types of MR measurements. The open coil geometry enables the implementation and investigation of hyperpolarization techniques like SABRE and ODNP and the system is ideal for the characterization and quantitative comparison of polarization transfer agents. We demonstrated the imaging capability of the setup and established the feasibility of future hyperpolarized *in vivo* experiments.

7.2 Summary of publication 2

SQUID-based detection of ultralow-field multinuclear NMR of substances hyperpolarized using signal amplification by reversible exchange

In quest of boosting signal amplitude for MR experiments, multiple parahydrogen induced polarization (PHIP) methods have been explored in recent years. SABRE is the only PHIP variant that allows for continuous hyperpolarization. The ULF-regime enables the implementation of SQUID-based multinuclear detection and the field cycling approach with variable B_p helps to exploit the optimal field range for SABRE polarization transfer. The goal of the study was to determine the dependency of the polarization transfer on polarization field amplitude and pulse duration, as well as the investigation of polarization transfer between ^1H and ^{19}F nuclei within the substrate.

The SABRE methodology of the study followed the description in the introduction (section 5.3.1) and in **publication 1** (summarized in section 7.1). The experiments were conducted in an earlier version of the SQUID-based ULF-MR system described in **publication 1**. All measurements were performed by varying the parameters of a prepolarized free-induction-decay pulse sequence, depicted in figure 5.1, with a precession field strength of $150\mu\text{T}$. Integration of the acquired NMR-spectrum over a sufficient frequency range (ca. 20Hz) around the resonance frequency yields the area under peak (AUP).

The same Iridium based $[\text{Ir}(\text{COD})(\text{IMes})(\text{Cl})]$ catalyst, dissolved in methanol with either 3,5-bis(trifluoromethyl)pyridine, ethyl-5-fluoronicotinic acid or 3-fluoropyridine as substrate (chemical structures in figure 7.7), was employed in all experiments. All substrates contain varying numbers of ^{19}F and ^1H nuclei, allowing for a comparison of their respective hyperpolarizability and for the investigation of polarization transfer between their spins.

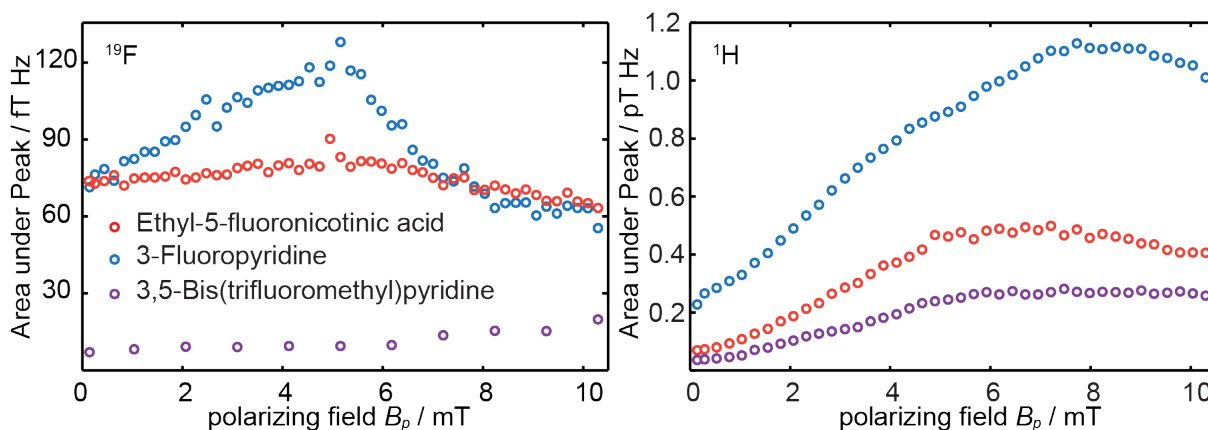


FIGURE 7.5: Area under Peak of ^{19}F (left) and ^1H (right) NMR-signals in dependency of B_p polarizing field strength for all three substrates

Sweeping the B_p from $144\mu\text{T}$ up to 10.3mT and plotting the AUP over B_p allows for a comparison of the field dependency for different substrates and nuclei. Figure 7.5 shows, that five of the six cases exhibit a clear field dependency and that the maximum enhancement of the ^1H signal is greater than for ^{19}F in all substrates. 3-fluoropyridine shows the strongest and 3,5-bis(trifluoromethyl)pyridine the weakest dependency. The optimal hyperpolarization field strength is higher for ^1H than for ^{19}F nuclei. Examining the real part of the signal reveals that it is split into multiple peaks with correlated amplitudes with only one exception that two of the ^{19}F side peaks of ethyl-5-fluoronicotinic acid undergo a phase flip during the sweeping of B_p .

The next type of measurements aimed at the impact of the polarization time t_{B_p} on the signal enhancement. t_{B_p} was swept from 0.1s to 10.1s at the optimal B_p amplitude determined from figure 7.5. As shown in figure 7.6, a buildup function is fitted to the plot of AUP over t_{B_p} , yielding the time dependency of the sample magnetization M with the sample specific buildup time T_{HP} , summarized in table 7.2. 3-fluoropyridine

Substrate	Nucleus	$T_{HP}[s]$
Ethyl-5-fluoronicotinic acid	^{19}F	2.4 ± 0.5
3-Fluoropyridine	^{19}F	9.4 ± 3.9
3,5-Bis(trifluoromethyl)pyridine	^{19}F	-
Ethyl-5-fluoronicotinic acid	^1H	3.4 ± 0.5
3-Fluoropyridine	^1H	9.7 ± 2.4
3,5-Bis(trifluoromethyl)pyridine	^1H	3.9 ± 1.0

TABLE 7.2: Buildup times T_{HP} for different substrates and nuclei

has the longest T_{HP} with a negligible difference between the two nuclei. The buildup time for ^{19}F is shorter than for ^1H in ethyl-5-fluoronicotinic acid and the buildup of ^1H 3,5-bis(trifluoromethyl)pyridine hyperpolarization takes slightly longer than in ethyl-5-fluoronicotinic acid. Due to the field independency of ^{19}F hyperpolarization in 3,5-bis(trifluoromethyl)pyridine (see figure 7.5) its T_{HP} could not be determined, since the polarization transfer happens even before the respective B_p pulse.

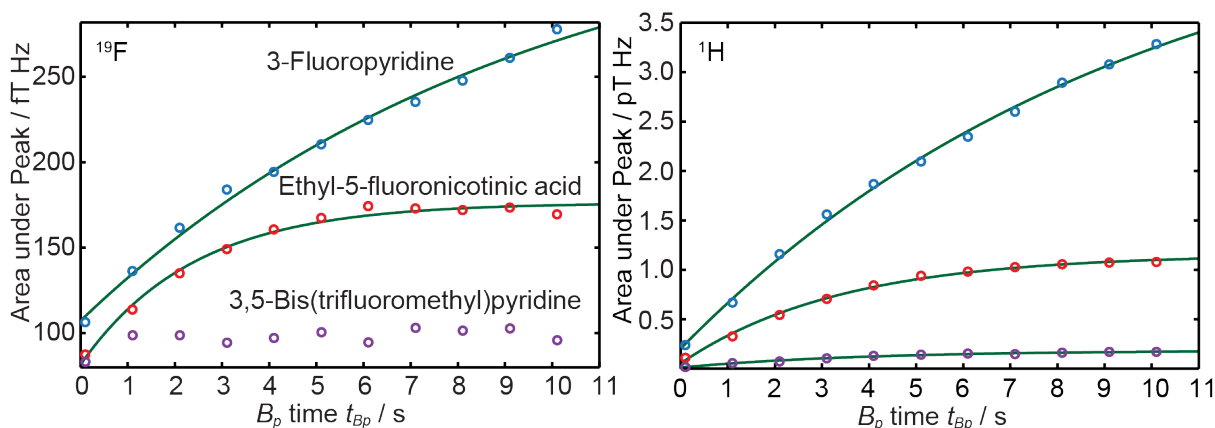


FIGURE 7.6: Area under Peak of ^{19}F (left) and ^1H (right) NMR-signals in dependency of the polarization time t_{Bp} for all three substrates with buildup function fits in green

Optimized B_p pulse amplitudes and durations from the first measurements in combination with a number of ≥ 50 averages were utilized to acquire high-resolution SABRE spectra of both nuclei in all three substrates. The spectra were also simulated, showing a close resemblance between thermal simulations and hyperpolarized experimental data (figure 7.7). Except for 3,5-bis(trifluoromethyl)pyridine, where no J-coupling was observed, the spectra resolve multiple J-coupling resonances for both nuclei. While resonance positions are mostly consistent between the two datasets, the amplitudes differ and the orientation of the central ^1H peak is flipped in the experimental data. This shows, that SABRE can greatly impact signal amplitudes without affecting the general spectral structure. The central ^1H peak flip was hypothesized to stem from hyperpolarized methanol. In **publication 3** this interpretation was refuted. It results from the superposition of hyperpolarized signals from substrate, hydrogen and catalyst molecules.

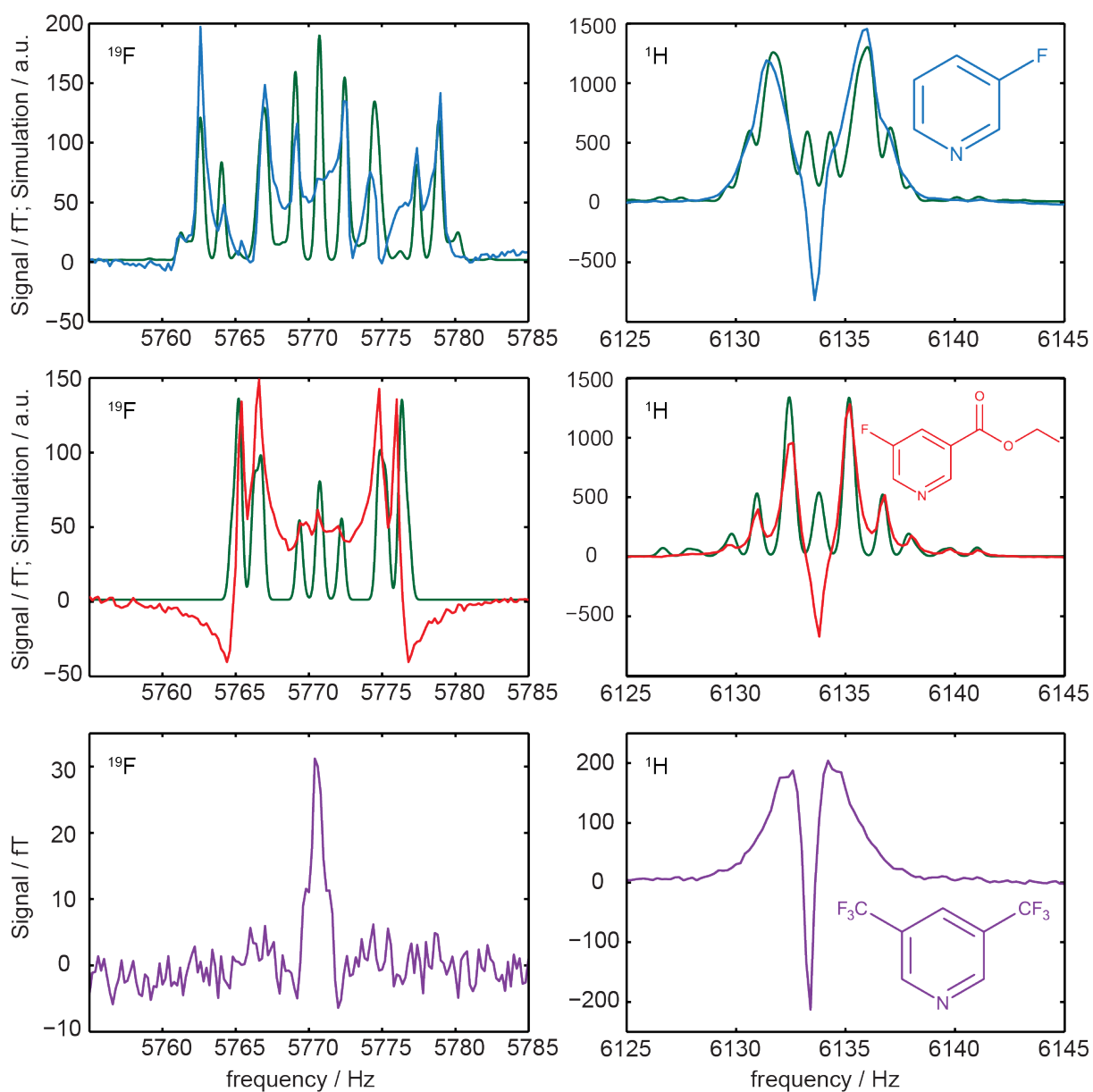


FIGURE 7.7: SABRE enhanced ^{19}F (left) and ^1H (right) spectra at ULF of 3-fluoropyridine (top), ethyl-5-fluoronicotinic acid (middle) and 3,5-bis(trifluoromethyl)pyridine (bottom). Simulations in green and experimental data in blue, red and purple.

The experiments emphasize that there is more to the polarization transfer process than J-coupling, which can not singularly account for the difference in field dependency of the signal enhancement for the two nuclei. While J-coupling may only facilitate an indirect polarization transfer to substrate ^{19}F through substrate protons, additional mechanisms have to be responsible for the observed phenomenon. A direct polarization transfer to ^{19}F , or proton-proton exchange reactions may explain the results, but require further investigation.

The study additionally is a proof of concept for the detection of hyperpolarized multinuclear spectra with a SQUID-based ULF-NMR setup. The increase of SNR by continuous SABRE hyperpolarization enables the use of the broadband detector at ultralow fields, making these types of measurements possible and facilitating a deeper insight into the workings of SABRE polarization transfer.

7.3 Summary of publication 3

Multiple Quantum Coherences Hyperpolarized at Ultra-Low Fields

SABRE is a parahydrogen based method, which works best in low and ultralow fields and continuously transfers high $p\text{H}_2$ spin order onto a target substrate. The goal of the study was to employ simulations and correlation spectroscopy (COSY) experiments in order to investigate the hyperpolarized spin states and to better understand the underlying processes responsible for the spin polarization transfer.

In previous studies (**publication 2**), the composition of the measured ^1H signal was not yet fully understood. The ^1H spectra of the 3-fluoropyridine substrate, of H_2 and of the [rIMesCODCl] catalyst were simulated separately. A comparison to the experimental data indicates that the measured spectrum is a superposition of all three components.

COSY is a powerful tool for generating two-dimensional (2D) correlation maps which reveal the quantum coherences (QCs) of spin ensembles. The COSY sequence consists of a variable evolution time t_1 between two 90° B_1 pulses of variable phases φ_1 and φ_2 before the data acquisition block with receiver phase φ_{rec} . A SABRE hyperpolarization phase was added before the first B_1 pulse. Sweeping the t_1 time produces a signal matrix and applying a 2D Fourier transform yields the 2D spectrum.

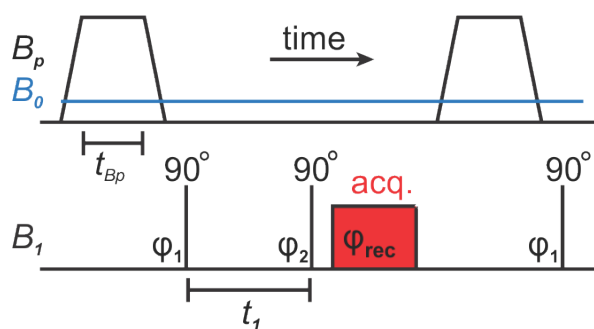


FIGURE 7.8: Schematic of a prepolarized COSY sequence

In 3FP, the four ^1H nuclear spins combine with the ^{19}F spin to a 5 spin-1/2 system. This spin system was simulated for all measurements performed within the study, to gain a better understanding of the results by comparing experimental and simulated data. The simulations predicted 15 separate groups of peaks for a simple hyperpolarized COSY measurement, with the experimental COSY map revealing 11 groups of peaks (due to low Amplitude of higher order QCs), relating to quantum coherences up to the third order, thus indicating that 3-spin orders are populated.

Aliasing of the signal due to experimental confinements on measurement duration and spectral width caused peaks from different QCs to overlap in the first measurement. Through phase cycling with various combinations of φ_1 and φ_{rec} , specific QCs can be selected, yielding four different COSY spectra, that separate all previously overlapped peaks, as depicted in figure 7.9.

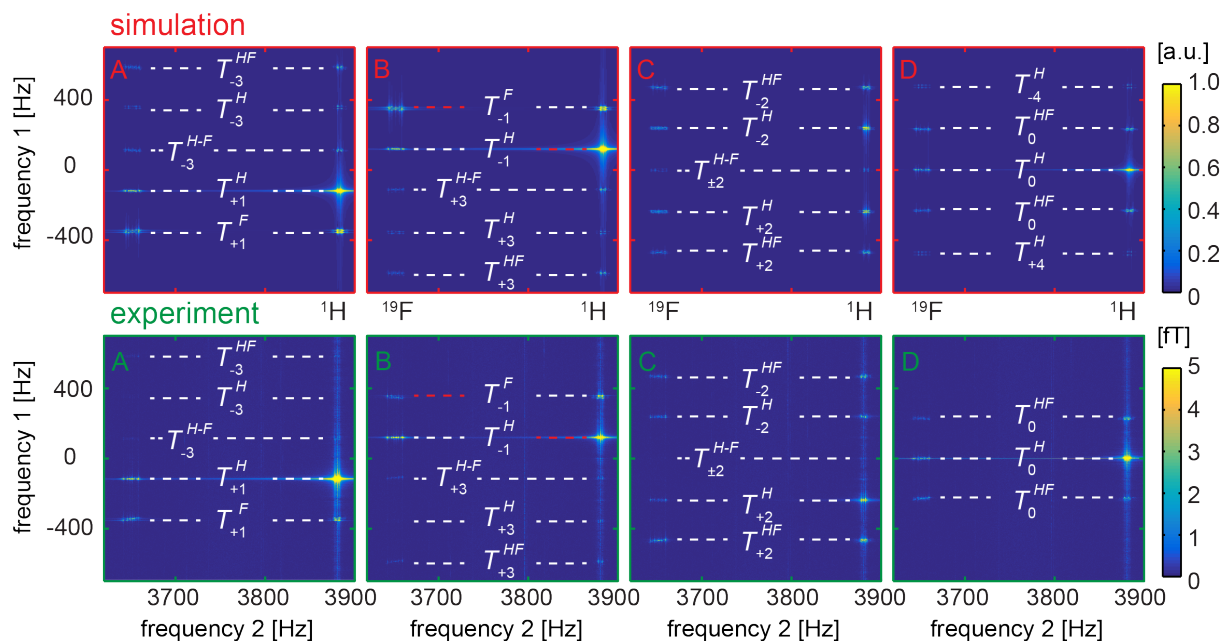


FIGURE 7.9: Simulated (top) and measured (bottom) coherence selective COSY spectra of 3FP, achieved by four different phase cycling schemes (A-D). The respective quantum coherences T are denoted with the coherence order in the subscript and the active nuclei in the superscript.

Simulation and experimental data matched well, but QCs above the third order were concealed by the system noise and thus not detected in the experiments. The ULF COSY 2D spectrum for a thermal Zeeman polarization was simulated, yielding QCs up to the first order, confirming that the detected high-order QCs were specific to a high-order spin state population from SABRE hyperpolarization.

The experiments provide evidence of the hyperpolarization of homo- and heteronuclear multiple-spin states in ULF SABRE experiments. They demonstrate, that COSY at ULF, especially with the application of the phase cycling scheme and with multinuclear detection, is a powerful tool to investigate QCs of multiple-spin systems. The results confirm the distribution of polarization between all strongly-coupled spins of the system at low magnetic fields and contribute to the future development of the SABRE method.

7.4 Summary of publication 4

The effects of nitroxide structure upon ^1H Overhauser dynamic nuclear polarization efficacy at ultralow-field¹

The *in vivo* application of Overhauser DNP is one promising approach to signal enhancement in Ultralow-field MRI experiments due to its easy implementation and sufficient excitation pulse penetration depth in this field range. Several *in vivo* OMRI experiments in the low- and ultralow field range have already been reported by different groups.[24–27] For these experiments, the unpaired electrons of free radicals are utilized to serve as a source for electron spin polarization. The choice of radical as polarizing agent is a critical factor to the maximum achievable signal enhancement, but radicals may also have to meet biological and economic requirements. Nitroxides are one of the most common spin probes for ODPN experiments and several derivatives have been investigated before. Here we present a systematic study of 26 different nitroxide radicals in search of chemical properties that constitute an effective polarization transfer agent.

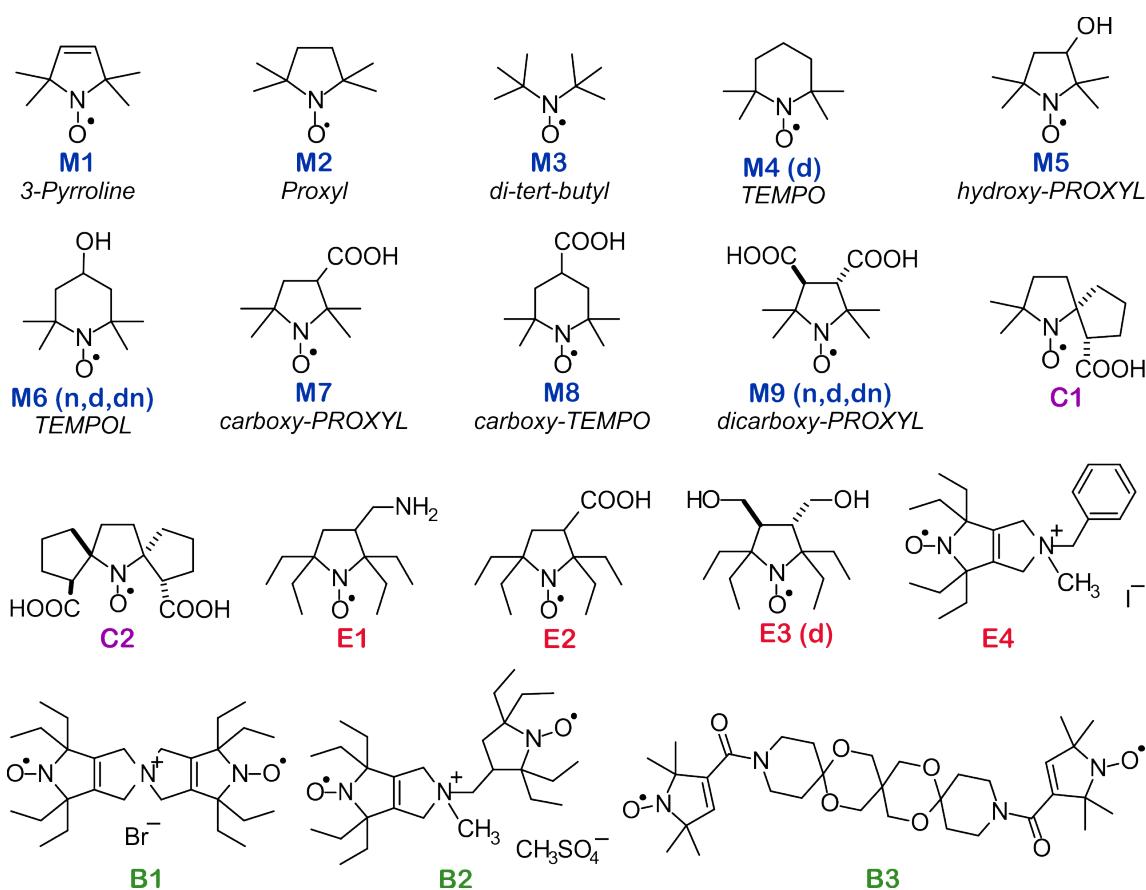


FIGURE 7.10: Chemical structure of the nitroxide radicals characterized for **publication 4**. "n", "d" and "dn" indicates the inclusion of derivatives with ^{15}N -labelling, deuteration, or both respectively in the study.

¹This section contains corrected values. More information is provided in ref. [40] and in the appendix.

There are multiple ways to characterize and describe the efficiency of the ODNP polarization transfer in liquids. While the coupling factor ξ and leakage factor f are independent of spin probe concentration and RF-power, the maximum achievable enhancement E_{\max} and the half-power $P_{1/2}$ needed to reach $E_{\max}/2$ are more dependent on experimental conditions, but offer a more intuitive description and comparison of spin probe performance (compare section 5.3.2 and figure 5.4).

The set of characterized compounds mostly contained, but was not limited to pyrrolidines (with a five membered ring) and piperidines (with a six membered ring) with either tetramethyls or tetraethyls as substituents next to the nitroxide group and varying substituents at the remaining positions of the ring structure. Additional variations included ^{15}N -labelling, deuteration (in the following both are denoted as "modified") or biradical structures. Commercially available compounds like TEMPO, TEMPOL or 3-carboxy-PROXYL provide a point of reference to other studies in literature.[26, 41, 42]

Radical	B_p [mT]	$P_{1/2}$ [W]	E_{\max}		$FWHM$ [μT]		MW [g/mol]	
M1	2.27	6.0 ± 0.2	-154.6	± 13.4	54.0	± 0.6	140.2	
M2	2.27	4.8 ± 0.1	-166.1	± 6.7	44.7	± 0.5	142.2	
M3	2.14	3.9 ± 0.2	-165.7	± 10.0	39.9	± 0.6	144.2	
M4	2.12	6.2 ± 0.3	-153.7	± 5.6	55.1	± 0.6	156.3	
M5	2.30	4.9 ± 0.2	-134.6	± 12.3	47.0	± 0.5	158.2	
M6	2.15	7.2 ± 0.3	-138.7	± 6.8	61.9	± 0.9	172.2	
M7	2.28	5.4 ± 0.2	-134.4	± 5.7	50.6	± 0.6	185.2	
M8	2.14	6.2 ± 0.3	-117.7	± 6.7	60.1	± 1.0	200.3	
M9	2.30	4.4 ± 0.2	-102.9	± 4.1	48.6	± 1.1	228.2	
M4d	2.13	4.7 ± 0.2	-178.2	± 8.3	43.6	± 0.5	174.4	
M6n	2.64	5.6 ± 0.2	-163.0	± 11.5	58.5	± 0.8	173.2	
M6d	2.15	4.2 ± 0.2	-161.2	± 5.0	40.6	± 0.4	188.3	
M6dn	2.64	3.7 ± 0.2	-191.1	± 6.8	38.6	± 0.4	189.3	
M9n	2.75	3.1 ± 0.2	-131.9	± 5.6	47.5	± 2.3	229.2	
M9d	2.29	2.8 ± 0.1	-117.8	± 8.8	36.7	± 5.9	242.3	
M9dn	2.74	1.1 ± 0.1	-123.3	± 2.0	37.3	± 0.9	243.3	
E1	2.40	9.5 ± 0.6	-96.7	± 3.5	117.2	± 11.0	228.4	
E2	2.37	8.2 ± 0.4	-96.3	± 3.1	104.3	± 4.8	241.3	
E3	2.42	10.9 ± 0.9	-81.2	± 4.8	130.1	± 10.1	258.4	
E3d	2.42	9.2 ± 0.4	-98.6	± 5.6	75.7	± 1.4	269.4	
E4	2.36	6.4 ± 0.3	-114.5	± 4.6	62.1	± 2.8	342.5	
C1	2.30	4.9 ± 0.3	-105.9	± 10.2	74.1	± 4.7	212.3	
C2	2.39	8.2 ± 0.4	-82.2	± 7.8	94.0	± 2.4	280.3	
B1*	3.66	$\gg 5$...	< -10	...	> 700	...	458.7
B2*	3.22	$\gg 5$...	< -8	...	> 500	...	462.7
B3B3	2.29	17.7 ± 0.7	-86.2	± 3.5	76.5	± 1.8	630.8	

TABLE 7.3: Spin probe properties and measured ODNP results.

*values could not be properly determined due to strong line broadening

Besides their well known chemical features like the molecular weight MW and their chemical structure, the ODNP-related properties of each compound were determined and compared. This included the leakage factor f , the spectral linewidth $FWHM$, the product of coupling factor and maximum saturation $\xi \times s_{\max}$, the maximum enhancement E_{\max} and the half-power $P_{1/2}$

All measurements were performed in the SQUID based ULF system described in **publication 1**. B_0 was set to $92\mu\text{T}$ and a new RF-coil with a 16.1mm diameter was tuned to $\omega_e = 120 \pm 1\text{MHz}$. The radicals were solved in PBS at $\text{pH} = 7.3$ and measured in sample containers with a volume of 1.2ml. To prepare the characterization, the polarization buildup time T_{HP} was measured. $T_1(B_p)$ was determined to calculate the leakage factor f and measuring the dependency of the enhancement on the RF-power provided $P_{1/2}$, E_{\max} and the product of $\xi \times s_{\max}$. Lastly, varying B_p and scaling the datapoints with the respective non-hyperpolarized signal amplitude yields the enhancement spectrum, from which $FWHM$ can be determined.

Of all nitroxides, small perdeuterated and ^{15}N -labelled pyrrolidines fared best, but the large dataset presented in table 7.3 allows for several more general observations.

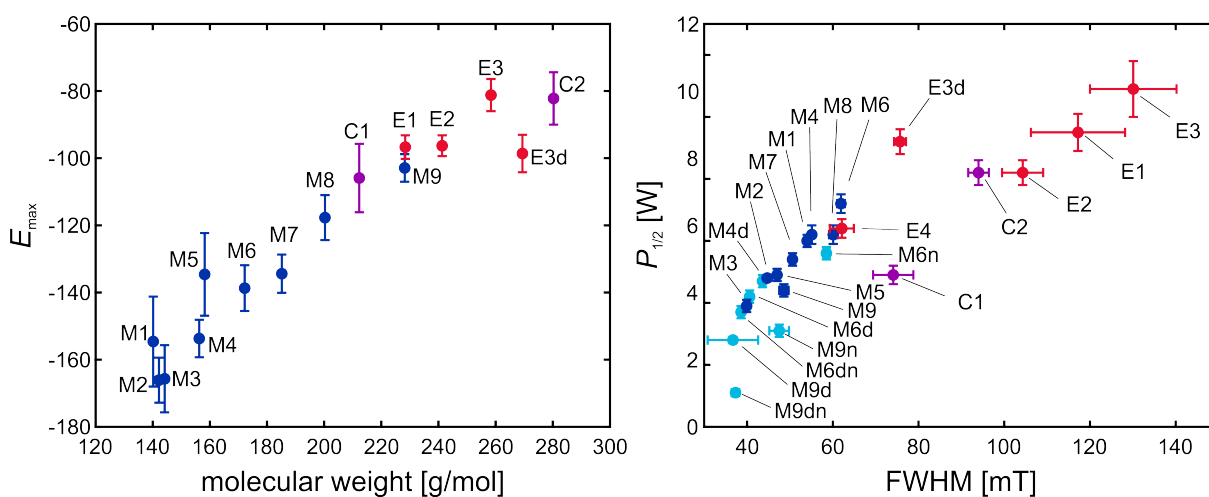


FIGURE 7.11: Results for monoradical nitroxides, plotting E_{\max} vs. molecular weight (a) and $P_{1/2}$ vs. linewidth (b), with both plots showing correlations between the respective parameters.

A clear correlation of E_{\max} of the unmodified monoradical nitroxides to the MW is visible in figure 7.11 (a). Size and weight of a molecule affect its translational diffusion and rotational tumbling, with a lower weight resulting in faster diffusion, which positively affects $|E_{\max}|$. $FWHM$ and $P_{1/2}$ may also be influenced by MW , since faster rotational tumbling could average out anisotropic contributions to the spectral linewidth, but such influence is not distinguishable in the dataset.

Another correlation is found between $P_{1/2}$ and $FWHM$. Independent of its cause, a broadening of the lineshape will lower s_{\max} , which increases $P_{1/2}$, leading to the clear

trend in figure 7.11 (b). The finite homogeneity of the polarizing field confines the measurable lower limit of the $FWHM$.

The type of substituents next to the nitroxide group had a significant influence on $FWHM$ and $P_{1/2}$. Several pyrrolidines with geminal ethyl substituents at position 2 and 5 ("E"-compounds) were compared to derivatives with tetraethyl substituents ("M"-compounds). In general, tetraethyl nitroxides showed increased $FWHM$ and $P_{1/2}$, due to stronger unresolved hyperfine coupling. The two exceptions, **M3d** and **M4** further support this point, both providing explanations for a lowered intramolecular coupling. Figure 7.12 illustrates the effect, comparing spectra of two equivalents where only the neighboring substituents are interchanged. The tetraethyl compounds also exhibit lower $|E_{\max}|$, but the differences are sufficiently explained by the previously discussed impact of MW , depicted in fig. 7.11.

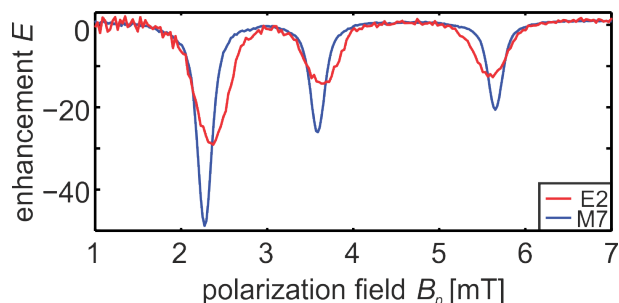


FIGURE 7.12: ODNP-spectra of compounds E2 and M7, with the tetraethyl compound exhibiting significant line broadening.

While the data does not indicate an influence of the heterocyclic ring structure on E_{\max} , the pyrrolidones exhibited lower $FWHM$ and $P_{1/2}$ than piperidines. This could be explained by a difference in unresolved intramolecular interactions for the two ring systems, or by different conformational flexibilities.

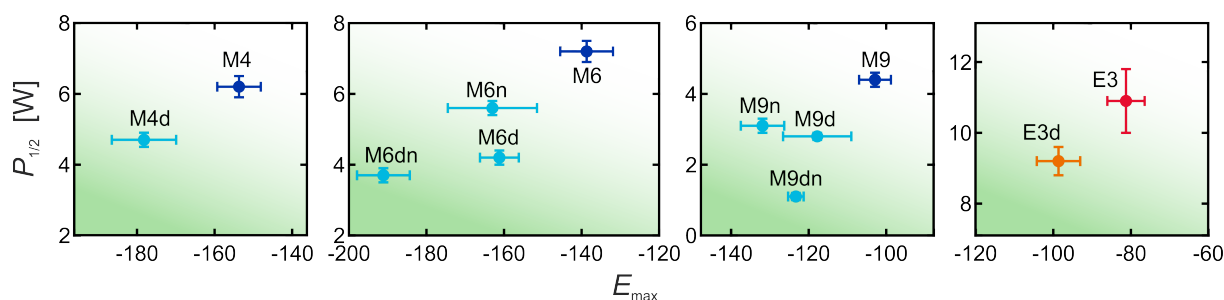


FIGURE 7.13: $P_{1/2}$ and E_{\max} of modified derivatives compared to unmodified counterparts, showing improvements for all modifications.

Eight different modified (deuterated and/or ^{15}N -labelled) nitroxides were investigated. All of them showed significant improvements in E_{\max} and $P_{1/2}$ compared to their unmodified analogues. The lower hyperfine coupling of deuterium, compared to hydrogen, lowers intramolecular coupling, thus reducing $FWHM$ and $P_{1/2}$. Electrons of ^{15}N nitroxides exhibit less hyperfine lines than in naturally more abundant ^{14}N nitroxides, reducing their ESR transitions. Together with increased electron relaxation times, this improves E_{\max} and $P_{1/2}$ in the ^{15}N -labelled derivatives, as fig. 7.13 shows.

We also investigated the difference between three biradical compounds and similar monoradical spin probes, with the results depending strongly on the molecular structure and the resulting intramolecular spin-spin interactions. Biradicals with strong interactions between the two electron spins (**B1** and **B2**) exhibited extensive spectral broadening to a degree where the three nitroxide peaks are indistinguishable in figure 7.14, when compared to a similar monoradical spin probe (**E4**). The resulting $P_{1/2}$ is an order of magnitude greater than with comparable monoradicals. The biradical **B3** emphasizes this point, since it shows much lower $FWHM$ and $P_{1/2}$ due to a greater distance between the two electron spins.

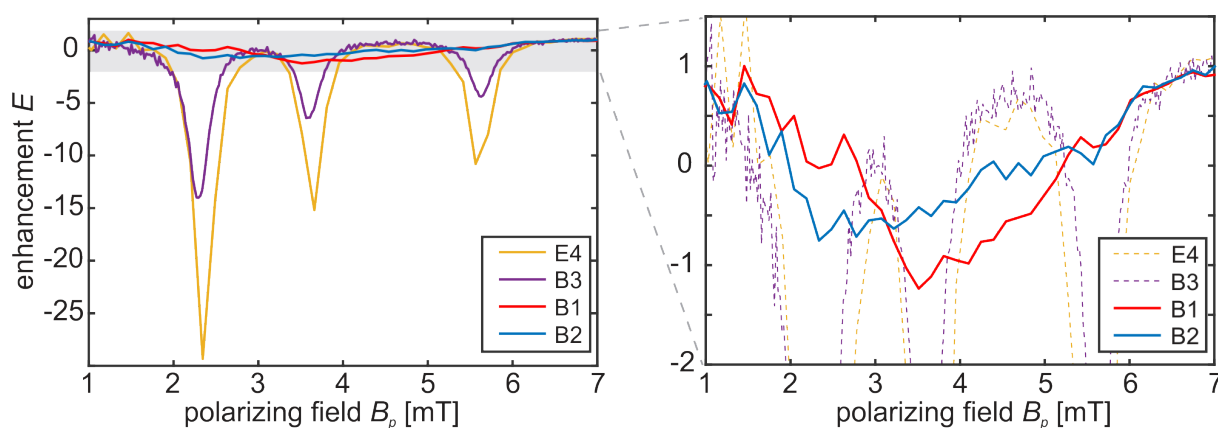


FIGURE 7.14: Spectra of biradicals compared to E4.

The ionic charge of nitroxides in buffered aqueous solution did not produce a detectable effect.

The aim of the study was to improve the understanding of the influences on the ODNP-efficacy of nitroxide spin probes in order to predict and optimize spin probe design for *in vivo* applications. To achieve sufficient SNR, these applications require high $|E_{\max}|$, combined with low $P_{1/2}$ to prevent excessive tissue heating.

$|E_{\max}|$ seems to be optimized by increased spin probe mobility, which can be achieved employing low molecular weights. Deuteration and ^{15}N -labelling provide further improvements. $P_{1/2}$ is strongly affected by the spectral lineshape. Preventing or reducing intra- and intermolecular spin-spin interactions ensures narrow lines and a low $P_{1/2}$. While unresolved hyperfine couplings from tetraethyl substituents or electron spin-spin interactions in biradicals introduce line broadening, deuteration and ^{15}N -labelling provide measures to counteract such effects.

Apart from trying to prevent tissue heating through low $P_{1/2}$, our study explicitly disregards the biological context with issues like spin probe toxicity, stability against reduction or retention in the organism. These topics can be addressed by employing macromolecular structures, possibly using them as functionalized delivery systems. While the added chemical environment could impact the ODNP properties, our study provides a reference and good starting point for selecting spin probe candidates for the incorporation into macromolecules.

7.5 Discussion of results

All four of the summarized publications highlight the main theme of **publication 1**. Not only does the ultralow-field MR approach profit from the enhanced SNR in hyperpolarized measurements, but the ULF setup in turn enables the implementation of numerous unique types of experiments, facilitating the exploration and optimization of the hyperpolarization techniques. The presented results showcase the flexibility of the system. It has been adapted to perform SABRE and ODNP hyperpolarization, multinuclear detection, multidimensional correlation spectroscopy, spacially resolved imaging and quantitatively comparable characterization measurements of polarizing agents. This track record demonstrates that modifications for novel hyperpolarization techniques and measurement schemes can easily be accommodated.

Some limitations have to be considered for measurements in the presented ULF-MR system. While the SQUID sensor is vital in terms of sensitivity and detection bandwidth, it also brings challenges. The inclusion of new components into the system always implicates the possibility of adding disturbances to the SQUID signal, which need to be circumvented or mitigated. The spacial sensitivity profile of the gradiometric SQUID assembly, which resembles a conventional surface coil, impacts the maximum sample volume or maximum field of view for MR-images. Complex sensor coil assemblies, which can produce a more uniform sensitivity profile, are harder to implement, but could be used to address the issue.

As can be seen in **publication 2** and **publication 3**, the ULF regime is ideal for the quick and easy investigation of SABRE polarization transfer and for the comparison of different catalysts and substrates. Once $p\text{H}_2$ is available from a commercial or a home-built $p\text{H}_2$ -generator, the experimental realization of the method is manageable and inexpensive. The polarization transfer process based on the high singlet state spin order and level anticrossings is able to target a multitude of different nuclei. As long as $p\text{H}_2$, catalyst and substrate are present in the sample solution, the process can be induced continuously.

In ultralow fields, ODNP is similarly straightforward to implement. A simple RF-excitation coil for electron excitation has to be added to an existing MR-setup and the low field ensures sufficient penetration depth into the sample. It is important to note, that excessive sample heating by the RF-pulse has to be prevented. Still, the necessary hardware is relatively low-cost and the excitation pulse is easily integrated into existing measurement sequences. The ODNP hyperpolarization method can be applied to a wide range nuclei. If the presence of unpaired electrons in the sample is ensured, the technique can be performed continuously.

The ability to continuously re-hyperpolarize the sample is an advantage of both SABRE and ODNP over more prevalent, commercially available hyperpolarization techniques like dissolution DNP (d-DNP). In this approach, immense temperature jumps are combined with strong magnetic fields as well as dnp, so that enhancements of $E > 50000$ have been reported.[43] However, this procedure is non-reversible for a

given sample and only enables single-shot type experiments, which are limited in duration by T_1 -relaxation. In addition, the preparation of the hyperpolarized state is time-consuming.[10] In contrast, the continuously inducible hyperpolarization processes of SABRE and ODNP take just a few seconds. They are only limited by the presence and stability of the polarizing agents, which usually outlast the T_1 -relaxation processes.

Most current MR-systems work at high magnetic fields. While several approaches to high-field SABRE have been proposed and implemented,[44–47] the translation of ODNP to high fields still is hampered by the limited penetration depth of GHz-frequency pulses, which would be necessary for saturating the electron spin transition. ODNP of a continuously flowing liquid in the fringe field of an MR magnet [48] and the hyperpolarization of sub-ml sample volumes [49] mark the forefront of high-field ODNP research.

With up to 10^5 -fold enhancement reported for spectroscopic *in vitro* SABRE experiments,[50] it has the upper hand over ODNPs enhancement factors of ^1H , which are in the range of 10^2 - 10^3 for these types of measurements.[10, 22] It is important to note, that the nitroxides presented in **publication 4** do not exploit the full potential of the ODNP method in terms of maximum enhancement. The nitroxide hyperfine splitting produces 3 usable electron transitions, leading to 1/3 of the maximum enhancement theoretically achievable with single-line radicals without hyperfine splitting.[22] Even though they are difficult to synthesize and more expensive to obtain commercially, compared to nitroxides, such single-line radicals have been successfully synthesized and tested.[25, 51, 52] In any case, ODNP polarization levels are limited by the thermal electron spin polarization with $|\gamma_e| \approx 660 \cdot |\gamma_H|$ and yet no approach to surpass the dipolar limit has been reported.

Directing the focus towards the *in vivo* application of the two techniques radically shifts the balance towards ODNP. The necessity of gaseous $p\text{H}_2$ for *in situ* SABRE hyperpolarization and issues with catalyst stability and solubility rule out the continuous *in vivo* SABRE polarization transfer. Instead a single shot approach, where a hyperpolarized substrate bolus is injected, or the continuous injection of externally hyperpolarized substrate seem to be more likely. Even then, issues like water solubility of the catalyst and catalyst removal from the injectable substrate have to be tackled to make the method biocompatible. So far, multiple solutions have been explored *in vitro*. [16, 17, 53] Combined with the use of long-lived spin states,[54, 55] which address the T_1 -related time limit of single-shot experiments, a future *in vivo* application of SABRE is feasible. It may offer a cheaper, quicker and less complex alternative to current d-DNP hyperpolarizers and could add additional substrates to the range of hyperpolarized agents available for injection. Studies contributing to a deeper understanding of the underlying physical effects, like the ones presented in **publication 2** and **publication 3**, facilitate this development.

In regard to actual *in vivo* implementation, literature already provides promising examples of both approaches. While *in vivo* experiments with SABRE hyperpolarized substrate have not yet been published, several groups have successfully employed the closely related, hydrogenative PHIP method to perform *in vivo* MR-imaging with hyperpolarized ^{13}C agents.[56, 57] Regarding the success in catalyst removal reported by

lali et al. [53], a translation to non-hydrogenative SABRE seems only a matter of time. In terms of ODNP, numerous successful Overhauser-MRI experiments on small animals already have been reported. However, biocompatibility of the necessary chemicals and RF-heating of the sample still has to be considered. Free radicals usually are highly reactive compounds with low stability against reduction. While they can be stable in buffered aqueous solution, *in vivo* measurement duration currently is limited by their fast reduction or excretion in biological systems.[26, 27, 58, 59] Sterical shielding, as with the tetraethyl substituents of the E1-E4-compounds in **publication 4** offers improvements,[60, 61] but at the cost of ODNP-efficacy. Other approaches involve the incorporation of radicals into larger, macromolecular structures, either as delivery system ensuring a constant release of unreduced radicals, or simply to hinder interactions with large biomolecules, while ensuring access for small target molecules.[34, 36, 62–64] The results of **publication 4** contribute to this direction of research, serving as a reference for radical selection and elucidating the impact of different physico-chemical properties of spin probe efficacy. Two important conclusions can be directly transferred to macromolecular spin probe design. Firstly, the linker between macromolecule and small radical should allow flexible, unhindered movement of the radical, as rotational tumbling and translational diffusion impact ODNP efficacy. Secondly, if multiple radical sites are incorporated into one macromolecule, strong spin-spin interactions between them have to be avoided, in order to prevent significant line broadening.

Biodistribution poses a challenge to the *in vivo* application of both hyperpolarization methods, as the fast accumulation of polarizing agents or substrate in one area could lead to their absence in other possible regions of interest. If e.g. brain imaging is pursued, the blood-brain-barrier permeability of the agents has to be ensured. The *ex vivo* imaging results of **publication 1** highlight this point. Figure 7.4 (a) shows respectable SNR, but the radicals did not diffuse away from the injection site due to the absence of metabolic activity *ex vivo*, resulting in very localized signal enhancement. However, this should be greatly improved in the living organism, and biodistribution also offers great opportunity if utilized deliberately. The incorporation of radicals into macromolecules for ODNP as discussed above, or the design and selection of specific SABRE substrates both offer the possibility of functionalized signal enhancement. Similar to contrast agents in high-field MR, such functionalization offers great benefits. It could be utilized to improve diagnostics by mapping biological or physical properties, or by specifically highlighting diseased tissue.[26, 52, 65].

An important factor contributing to the relevance of the investigated methods and presented results is the recent commercial availability of low-field MRI scanners operating at 64mT.[66] While these systems are capable of providing diagnostic insight with thermal spin polarization, their existence demonstrates a general interest in low-field applications and could pave the way for the medical application of hyperpolarized MR-imaging methods operating at low- and ultralow fields.

8 Conclusion and outlook

8.1 Conclusion

The results of **publication 1** establish the presented ULF-MR system as an effective tool for the investigation and refinement of the two hyperpolarization techniques SABRE and ODNP. The study demonstrates the flexibility of the system by presenting multiple types of spectroscopic measurements to investigate the dependency of the polarization transfer on various parameters. The *ex vivo* Overhauser-MR images prove the feasibility of similar *in vivo* measurements in the system and were a cornerstone to obtaining the necessary ethics permit for such experiments. As proof-of-concept experiments they also exposed areas of improvement, that have to be addressed in the future, namely optimized imaging sequences or spin probe design and their distribution in the body.

Publication 2 highlights the benefit of using the SQUID based broadband detector for simultaneous multinuclear detection to investigate polarization transfer. The results scrutinized the current understanding of the SABRE polarization transfer mechanisms, and the newly gained information raised further questions about the underlying processes.

The experiments in **publication 3** provide a more detailed insight into the polarization transfer mechanisms. They once again demonstrate how easy the ULF system can be modified to incorporate new measurement schemes and how capable it is as a tool for spectroscopic analysis. The combination of 2D correlation spectroscopy measurements with simulated data yields important information on the underlying polarization transfer processes and answers some of the questions raised in **publication 2**.

The objectives of **publication 4** at first seem to be of a purely practical nature, simply searching the most effective polarizing agent. However, the systematic study of numerous nitroxide radicals also promotes a deeper understanding of the underlying effects by making out correlations between the chemico-physical features and the ODNP-related properties of the characterized radicals and presents cues for optimizing spin probe performance for future experiments.

8.2 Outlook

As **publications 2** and **3** highlight the potential of SABRE experiments in the ULF-MR system, future experiments will aim at developing and testing new methodological approaches and measurement schemes of ULF-SABRE.

Since the release of **publication 3**, work on improving SABRE hyperpolarization of ^{15}N by 30% through alternating fields during the hyperpolarization phase (alt-SABRE) has been performed in our group and the results are already published.[67]

The next objective is the successful implementation of catalyst-separated hyperpolarization via SABRE (CASH-SABRE) with the help of a specifically designed two-phase SABRE-reactor. This approach aims at solving the catalyst-solubility and catalyst-removal issues still hindering the *in vivo* application of the SABRE method.

Publications 1 and **4** open up the two areas of research regarding the ODNP-enhanced experiments in the ULF-MR system.

As **publication 1** makes clear, the successful execution of *in vivo* Overhauser-MRI experiments at ultralow fields is one of the main goals of the project. The planned *in vivo* studies aim at investigating spin probe delivery, distribution and diffusion inside the living organism. Radical stability in the biological environment will be determined and the achievable enhancement while limiting RF-power to prevent RF-heating should be optimized.

Parallel to *in vivo* imaging, the spectroscopic characterization of novel spin probes in search of optimized polarizing agents will continue, pursuing the ideas of **publication 4**. First results of nitroxides incorporated into nanosized structures have been presented at the European Molecular Imaging Meeting 2021 [68] and promising initial ODNP-measurements of radicals incorporated into tobacco mosaic virus rods [69] or human serum albumin [70] already have been performed. The results indicate possible functionalization and warrant further studies of these compounds along with the characterization of additional small and macromolecular radical spin probes provided by our international collaborators.

Acknowledgements

The work culminating in the composition of this thesis spanned over a significant section of my life and I want to take this opportunity to thank for the immense support of numerous people who accompanied me during this time.

Firstly I want to thank my advisor Klaus Scheffler and my project leader Kai Buckenmaier for giving me the opportunity to become a part of their department and project and for providing the facilities and equipment for my studies. Thank you for giving me free reigns with my scientific endeavors and for fostering a supportive and welcoming environment.

Fritz Schick deserves my sincere gratitude for taking on the role of second reviewer of my thesis on such short notice.

I also want to thank Reinhold Kleiner for being my second advisor but more importantly together with Dieter Kölle for first bringing this amazing project to my attention.

I want to express my gratitude towards all our collaborators here in Germany, in the USA, in Serbia and in Russia for providing materials, for scientific discussions and advice and simply for their important contributions to the success of our shared projects.

I am truly grateful to the Cusanuswerk e.V. for supporting the livelihood of me and my family, but especially for letting me be a part of an amazing community of scholarship students with all their fun and interesting events and conventions.

Great thanks also belongs to my colleagues here at the MPI. Philipp, who put a lot of work into improving the measurement routine, Rebekka and Rolf for their continuous help with the OMRI measurements, and Jörn, Yulia and Goran for answering all my chemistry related questions. I am grateful for the patience of the staff of both the mechanical and and electronics workshop, who I tried to annoy with endless requests for new sample containers and who always happily provided help and advice, even for one or two side-projects. I want to thank Tina, my current office mates, my former office mates in the Kinderzimmer and basically anyone else in the department and MR-Center for creating a fun, communal atmosphere in which I found it easy to immediately feel at home and for all the shenanigans that never let everyday life get boring.

I am very thankful to my family and friends, who influenced and continuously supported this path in my life and who were always there, when I needed a helping hand, a shoulder to lean on, or someone to celebrate with.

I want to close with thanking my wife Elli for her endless love, encouragement and appreciation and my son for trying to understand my efforts, for his determination to help with my "Dokerbeit" and for always putting a smile on my face.

Bibliography

- [1] M. H. Levitt, *Spin Dynamics*, John Wiley & Sons, **2008**.
- [2] R. W. Brown, Y.-C. N. Cheng, E. M. Haacke, M. R. Thompson, R. Venkatesan, *Magnetic Resonance Imaging: Physical Principles and Sequence Design*, John Wiley & Sons, **2014**.
- [3] R. Kraus, M. Espy, P. Magnelind, P. Volegov, *Ultra-Low Field Nuclear Magnetic Resonance*, Oxford University Press, **2014**.
- [4] W. Myers, D. Slichter, M. Hatridge, S. Busch, M. Möble, R. McDermott, A. Trabesinger, J. Clarke, *Journal of Magnetic Resonance* **2007**, *186*, 182.
- [5] J. Clarke, M. Hatridge, M. Möble, *Annual Review of Biomedical Engineering* **2007**, *9*, 389.
- [6] M. Möble, S.-I. Han, W. R. Myers, S.-K. Lee, N. Kelso, M. Hatridge, A. Pines, J. Clarke, *Journal of Magnetic Resonance* **2006**, *179*, 146.
- [7] V. S. Zotev, A. N. Matlashov, P. L. Volegov, I. M. Savukov, M. A. Espy, J. C. Mosher, J. J. Gomez, R. H. Kraus, *Journal of Magnetic Resonance* **2008**, *194*, 115.
- [8] R. E. Sepponen, J. T. Sipponen, A. Sivula, *Journal of Computer Assisted Tomography* **1985**, *9*, 237.
- [9] M. Sarracanie, N. Salameh, *Frontiers in Physics* **2020**, *8*, 172.
- [10] U. L. Günther in *Modern NMR Methodology*, (Eds.: H. Heise, S. Matthews), Topics in Current Chemistry, Springer, Berlin, Heidelberg, **2013**, p. 23.
- [11] J.-B. Hövener, E. Y. Chekmenev, K. C. Harris, W. H. Perman, L. W. Robertson, B. D. Ross, P. Bhattacharya, *Magnetic Resonance Materials in Physics Biology and Medicine* **2009**, *22*, 111.
- [12] B. Feng, A. M. Coffey, R. D. Colon, E. Y. Chekmenev, K. W. Waddell, *Journal of Magnetic Resonance* **2012**, *214*, 258.
- [13] D. A. Barskiy, A. N. Pravdivtsev, K. L. Ivanov, K. V. Kovtunov, I. V. Koptug, *Physical Chemistry Chemical Physics* **2016**, *18*, 89.
- [14] J.-B. Hövener, A. N. Pravdivtsev, B. Kidd, C. R. Bowers, S. Glöggler, K. V. Kovtunov, M. Plaumann, R. Katz-Brull, K. Buckenmaier, A. Jerschow, F. Reineri, T. Theis, R. V. Shchepin, S. Wagner, P. Bhattacharya, N. M. Zacharias, E. Y. Chekmenev, *Angewandte Chemie International Edition* **2018**, *57*, 11140.
- [15] T. Theis, M. L. Truong, A. M. Coffey, R. V. Shchepin, K. W. Waddell, F. Shi, B. M. Goodson, W. S. Warren, E. Y. Chekmenev, *Journal of the American Chemical Society* **2015**, *137*, 1404.

- [16] M. Fekete, C. Gibard, G. J. Dear, G. G. R. Green, A. J. J. Hooper, A. D. Roberts, F. Cisnetti, S. B. Duckett, *Dalton Transactions* **2015**, 44, 7870.
- [17] P. J. Rayner, S. B. Duckett, *Angewandte Chemie International Edition* **2018**, 57, 6742.
- [18] A. W. Overhauser, *Physical Review* **1953**, 92, 411.
- [19] I. Solomon, *Physical Review* **1955**, 99, 559.
- [20] K. H. Hausser, D. Stehlik in *Advances in Magnetic and Optical Resonance, Vol. 3*, (Ed.: J. S. Waugh), Academic Press, **1968**, p. 79.
- [21] J. M. Franck, A. Pavlova, J. A. Scott, S. Han, *Progress in Nuclear Magnetic Resonance Spectroscopy* **2013**, 74, 33.
- [22] T. Guiberteau, D. Grucker, *Journal of Magnetic Resonance Series B* **1996**, 110, 47.
- [23] T. Prisner, V. Denysenkov, D. Sezer, *Journal of Magnetic Resonance* **2016**, 264, 68.
- [24] K. Golman, I. Leunbach, J. H. Ardenkjær-Larsen, G. J. Ehnholm, L.-G. Wistrand, J. S. Petersson, A. Järvi, S. Vahasalo, *Acta Radiologica* **1998**, 39, 10.
- [25] K. Golman, J. S. Petersson, J. H. Ardenkjaer-Larsen, I. Leunbach, L. G. Wistrand, G. Ehnholm, K. Liu, *Journal of Magnetic Resonance Imaging* **2000**, 12, 929.
- [26] N. Kosem, T. Naganuma, K. Ichikawa, N. Phumala Morales, K. Yasukawa, F. Hyodo, K.-i. Yamada, H. Utsumi, *Free Radical Biology and Medicine* **2012**, 53, 328.
- [27] D. E. J. Waddington, M. Sarracanie, N. Salameh, F. Herisson, C. Ayata, M. S. Rosen, *NMR in biomedicine* **2018**, 31, e3896.
- [28] M. Sarracanie, B. D. Armstrong, J. Stockmann, M. S. Rosen, *Magnetic Resonance in Medicine* **2014**, 71, 735.
- [29] A. Enomoto, K. Ichikawa, *Journal of Magnetic Resonance* **2021**, 323, 106890.
- [30] A. Pavlova, E. R. McCarney, D. W. Peterson, F. W. Dahlquist, J. Lew, S. Han, *Physical Chemistry Chemical Physics* **2009**, 11, 6833.
- [31] R. Kausik, A. Srivastava, P. A. Korevaar, G. Stucky, J. H. Waite, S. Han, *Macromolecules* **2009**, 42, 7404.
- [32] B. D. Armstrong, J. Choi, C. López, D. A. Wesener, W. Hubbell, S. Cavagnero, S. Han, *Journal of the American Chemical Society* **2011**, 133, 5987.
- [33] R. Kausik, S. Han, *Physical Chemistry Chemical Physics* **2011**, 13, 7732.
- [34] S. R. Burks, E. A. Legenzov, G. M. Rosen, J. P. Y. Kao, *Drug Metabolism and Disposition* **2011**, 39, 1961.
- [35] X. Wang, M. Emoto, Y. Miyake, K. Itto, S. Xu, H. Fujii, H. Hirata, H. Arimoto, *Bioorganic & Medicinal Chemistry Letters* **2016**, 26, 4947.
- [36] E. Parzy, V. Bouchaud, P. Massot, P. Voisin, N. Koonjoo, D. Moncelet, J.-M. Franconi, E. Thiaudière, P. Mellet, *PLOS ONE* **2013**, 8, e57946.
- [37] G. Gottardi, P. Mesirca, C. Agostini, D. Remondini, F. Bersani, *Bioelectromagnetics* **2003**, 24, 125.

- [38] K. C. J. Zevenhoven, S. Alanko, *Journal of Physics: Conference Series* **2014**, 507, 042050.
- [39] I. Ruset, L. Tsai, R. Mair, S. Patz, M. Hrovat, M. Rosen, I. Muradian, J. Ng, G. Topulos, J. Butler, R. Walsworth, F. Hersman, *Concepts in Magnetic Resonance Part B: Magnetic Resonance Engineering* **2006**, 29B, 210.
- [40] P. Fehling, K. Buckenmaier, S. A. Dobrynin, D. A. Morozov, Y. F. Polienko, Y. V. Khoroshunova, Y. Borozdina, P. Mayer, J. Engelmann, K. Scheffler, G. Angelovski, I. A. Kirilyuk, *The Journal of Chemical Physics* **2022**, 156, 089901.
- [41] J. L. Yoder, P. E. Magnelind, M. A. Espy, M. T. Janicke, *Applied Magnetic Resonance* **2018**, 49, 707.
- [42] C. Polyon, D. J. Lurie, W. Youngdee, C. Thomas, I. Thomas, *Journal of Physics D: Applied Physics* **2007**, 40, 5527.
- [43] L. F. Pinto, I. Marín-Montesinos, V. Lloveras, J. L. Muñoz-Gómez, M. Pons, J. Veciana, J. Vidal-Gancedo, *Chemical Communications* **2017**, 53, 3757.
- [44] A. N. Pravdivtsev, A. V. Yurkovskaya, H.-M. Vieth, K. L. Ivanov, *The Journal of Physical Chemistry B* **2015**, 119, 13619.
- [45] T. Theis, M. Truong, A. M. Coffey, E. Y. Chekmenev, W. S. Warren, *Journal of Magnetic Resonance* **2014**, 248, 23.
- [46] N. Eshuis, R. L. E. G. Aspers, B. J. A. van Weerdenburg, M. C. Feiters, F. P. J. T. Rutjes, S. S. Wijmenga, M. Tessari, *Angewandte Chemie International Edition* **2015**, 54, 14527.
- [47] S. S. Roy, G. Stevanato, P. J. Rayner, S. B. Duckett, *Journal of Magnetic Resonance* **2017**, 285, 55.
- [48] M. D. Lingwood, T. A. Siaw, N. Sailasuta, B. D. Ross, P. Bhattacharya, S. Han, *Journal of Magnetic Resonance* **2010**, 205, 247.
- [49] T. Dubroca, S. Wi, J. v. Tol, L. Frydman, S. Hill, *Physical Chemistry Chemical Physics* **2019**, 21, 21200.
- [50] P. J. Rayner, M. J. Burns, A. M. Olaru, P. Norcott, M. Fekete, G. G. R. Green, L. A. R. Highton, R. E. Mewis, S. B. Duckett, *Proceedings of the National Academy of Sciences* **2017**, 114, E3188.
- [51] J. H. Ardenkjær-Larsen, I. Laursen, I. Leunbach, G. Ehnholm, L. G. Wistrand, J. S. Petersson, K. Golman, *Journal of Magnetic Resonance* **1998**, 133, 1.
- [52] M. C. Krishna, S. English, K. Yamada, J. Yoo, R. Murugesan, N. Devasahayam, J. A. Cook, K. Golman, J. H. Ardenkjaer-Larsen, S. Subramanian, J. B. Mitchell, *Proceedings of the National Academy of Sciences* **2002**, 99, 2216.
- [53] W. Iali, A. M. Olaru, G. G. R. Green, S. B. Duckett, *Chemistry – A European Journal* **2017**, 23, 10491.
- [54] M. Carravetta, M. H. Levitt, *Journal of the American Chemical Society* **2004**, 126, 6228.
- [55] S. S. Roy, P. Norcott, P. J. Rayner, G. G. R. Green, S. B. Duckett, *Angewandte Chemie International Edition* **2016**, 55, 15642.

- [56] E. Cavallari, C. Carrera, M. Sorge, G. Bonne, A. Muchir, S. Aime, F. Reineri, *Scientific Reports* **2018**, *8*, 8366.
- [57] A. B. Schmidt, S. Berner, M. Braig, M. Zimmermann, J. Hennig, D. v. Elverfeldt, J.-B. Hövener, *PLOS ONE* **2018**, *13*, e0200141.
- [58] T. Niidome, R. Gokuden, K. Watanabe, T. Mori, T. Naganuma, H. Utsumi, K. Ichikawa, Y. Katayama, *Journal of Biomaterials Science Polymer Edition* **2014**, *25*, 1425.
- [59] G. Bacic, A. Pavicevic, F. Peyrot, *Redox Biology* **2016**, *8*, 226.
- [60] J. T. Paletta, M. Pink, B. Foley, S. Rajca, A. Rajca, *Organic Letters* **2012**, *14*, 5322.
- [61] I. A. Kirilyuk, A. A. Bobko, S. V. Semenov, D. A. Komarov, I. G. Irtegova, I. A. Grigor'ev, E. Bagryanskaya, *The Journal of Organic Chemistry* **2015**, *80*, 9118.
- [62] J. H. Ortony, C.-Y. Cheng, J. M. Franck, R. Kausik, A. Pavlova, J. Hunt, S. Han, *New Journal of Physics* **2011**, *13*, 015006.
- [63] J. Liebmann, J. Bourg, C. Murali Krishna, J. Glass, J. A. Cook, J. B. Mitchell, *Life Sciences* **1994**, *54*, PL503.
- [64] B. C. Dollmann, A. L. Kleschyov, V. Sen, V. Golubev, L. M. Schreiber, H. W. Spiess, K. Münnemann, D. Hinderberger, *ChemPhysChem* **2010**, *11*, 3656.
- [65] A. A. Bobko, T. D. Eubank, J. L. Voorhees, O. V. Efimova, I. A. Kirilyuk, S. Petryakov, D. G. Trofimov, C. B. Marsh, J. L. Zweier, I. A. Grigor'ev, A. Samouilov, V. V. Khramtsov, *Magnetic Resonance in Medicine* **2012**, *67*, 1827.
- [66] M. H. Mazurek, B. A. Cahn, M. M. Yuen, A. M. Prabhat, I. R. Chavva, J. T. Shah, A. L. Crawford, E. B. Welch, J. Rothberg, L. Sacolick, M. Poole, C. Wira, C. C. Matouk, A. Ward, N. Timario, A. Leasure, R. Beekman, T. J. Peng, J. Witsch, J. P. Antonios, G. J. Falcone, K. T. Gobeske, N. Petersen, J. Schindler, L. Sansing, E. J. Gilmore, D. Y. Hwang, J. A. Kim, A. Malhotra, G. Sze, M. S. Rosen, W. T. Kimberly, K. N. Sheth, *Nature Communications* **2021**, *12*, 5119.
- [67] A. N. Pravdivtsev, N. Kempf, M. Plaumann, J. Bernarding, K. Scheffler, J.-B. Hövener, K. Buckenmaier, *ChemPhysChem* **2021**, *22*, n/a.
- [68] P. Fehling, A. Pavicevic, A. Korenic, S. Dobrynin, D. Morozov, Y. Polienko, Y. Khoroshunova, J. Engelmann, K. Buckenmaier, K. Scheffler, G. Angelovski, I. A. Kirilyuk, M. Mojovic, P. Andjus, Y. Borozdina in European Molecular Imaging Meeting 2021, European Society for Molecular Imaging, Göttingen, Germany, **2021**.
- [69] M. Dharmarwardana, A. F. Martins, Z. Chen, P. M. Palacios, C. M. Nowak, R. P. Welch, S. Li, M. A. Luzuriaga, L. Bleris, B. S. Pierce, A. D. Sherry, J. J. Gassen-smith, *Molecular Pharmaceutics* **2018**, *15*, 2973.
- [70] S. Dobrynin, S. Kutseikin, D. Morozov, O. Krumkacheva, A. Spitsyna, Y. Gatilov, V. Silnikov, G. Angelovski, M. K. Bowman, I. Kirilyuk, A. Chubarov, *Molecules* **2020**, *25*, 1709.

Appendix

An error in the software for evaluating the measured data led to the incorrect scaling of some parameters in the original version of **publication 4**. Since all values were affected equally, there is a difference in absolute values, but the qualitative discussion and interpretation remains valid. A respective erratum explaining and correcting the error already has been published and is included in this **appendix**.^[40] This thesis, especially the summary of **publication 4** in section 7.4, contains the corrected values and figures.

The following publications are included with permission (**publication 1**, **publication 4** and the erratum to publication 4), or under creative commons license <https://creativecommons.org/licenses/by/4.0/> (**publication 2** and **publication 3**).

Publication 1

Mutual benefit achieved by combining ultralow-field magnetic resonance and hyperpolarizing techniques

Kai Buckenmaier,^{1,a)} Matthias Rudolph,^{1,2} Paul Fehling,¹ Theodor Steffen,¹ Christoph Back,² Rebekka Bernard,¹ Rolf Pohmann,¹ Johannes Bernarding,³ Reinhold Kleiner,² Dieter Koelle,² Markus Plaumann,³ and Klaus Scheffler¹

¹High-Field Magnetic Resonance Center, Max Planck Institute for Biological Cybernetics, Max-Planck-Ring 11, 72076 Tübingen, Germany

²Physikalisches Institut and Center for Quantum Science (CQ) in LISA⁺, University of Tübingen, Tübingen, Germany

³Department for Biometrics and Medical Informatics, Otto-von-Guericke University, Magdeburg, Germany

(Received 8 June 2018; accepted 8 November 2018; published online 10 December 2018)

Ultralow-field (ULF) nuclear magnetic resonance spectroscopy (MRS) and magnetic resonance imaging (MRI) are promising spectroscopy and imaging methods allowing for, e.g., the simultaneous detection of multiple nuclei or imaging in the vicinity of metals. To overcome the inherently low signal-to-noise ratio that usually hampers a wider application, we present an alternative approach to prepolarized ULF MRS employing hyperpolarization techniques like signal amplification by reversible exchange (SABRE) or Overhauser dynamic nuclear polarization (ODNP). Both techniques allow continuous hyperpolarization of ¹H as well as other MR-active nuclei. For the implementation, a superconducting quantum interference device (SQUID)-based ULF MRS/MRI detection scheme was constructed. Due to the very low intrinsic noise level, SQUIDs are superior to conventional Faraday detection coils at ULFs. Additionally, the broadband characteristics of SQUIDs enable them to simultaneously detect the MR signal of different nuclei such as ¹³C, ¹⁹F, or ¹H. Since SQUIDs detect the MR signal directly, they are an ideal tool for a quantitative investigation of hyperpolarization techniques such as SABRE or ODNP. © 2018 Author(s). All article content, except where otherwise noted, is licensed under a Creative Commons Attribution (CC BY) license (<http://creativecommons.org/licenses/by/4.0/>). <https://doi.org/10.1063/1.5043369>

INTRODUCTION

High field magnetic resonance imaging (MRI) is one of the most powerful non-invasive imaging techniques used for medical diagnostics. Worldwide approximately 36 000 MR machines are in use and about 2500 systems are sold every year.¹ Due to the high cost, so far only hospitals, research facilities, large companies, or radiology specialized local surgeries are able to afford MRI systems.

Commercial MRI or magnetic resonance spectroscopy (MRS) systems use superconducting magnets generating strong, static magnetic fields of $B_0 = 1.5$ T and higher. These magnets are not only expensive in fabrication but also heavy and bulky. It is difficult to construct open systems, and due to susceptibility differences between, e.g., tissue and metals, it is not possible to acquire images in the vicinity of metallic objects without distortion artifacts.^{2,3}

One possibility to make MRI affordable for, e.g., local surgeries and to circumvent the above-mentioned disadvantages is to decrease the B_0 field strength. Therefore, low field (<0.5 T) or ultralow-field (ULF, <10 mT) MRI and MRS experiments have been performed for over 20 years.⁴ Besides the cost advantage, ULF MRI offers very interesting prospects like the implementation of hybrid systems that allow interleaved MRI and magnetoencephalography (MEG)

measurements,^{5–8} imaging in the vicinity of metals⁹ or drastically greater differences of the longitudinal relaxation time constants (T_1) of different tissue types,^{10,11} thus enhancing contrast.

For ULF MRI, the resolution limiting noise level of the system is determined by sensor noise instead of the sample noise as is the case for high field MRI.¹² Therefore, the choice of the sensor used for detecting the MR signal is extremely important. Commonly the detectors are realized by either atomic magnetometers^{13,14} or direct current (DC) superconducting quantum interference devices (SQUIDs).^{15,16} Due to a limited bandwidth from DC to ~1 kHz,¹⁷ atomic magnetometers are only practical for B_0 fields below the earth magnetic field. SQUIDs, however, can be used up to B_0 fields of several mT while showing a better noise performance than, e.g., a conventional Faraday detection coil, which is used for high field MRI.¹²

The main disadvantage of ULF MRI is the very low signal-to-noise ratio (SNR). The amplitude of the MR signal scales according to Curie's law and increases with the B_0 field strength. This is the main reason why there is a trend toward even higher magnetic fields for MRI systems. At ULF, only a very low MR signal is left. In order to overcome this problem, the sample can be prepolarized with a magnetic field of the order of 10–100 mT.¹⁸ The effectiveness of this noninvasive approach has been demonstrated impressively *in vivo* by several groups.^{5,7,19–21}

^{a)} Author to whom correspondence should be addressed: kai.buckenmaier@tuebingen.mpg.de

Another yet invasive approach to enhance the MR signal at ULF relies on hyperpolarization techniques.^{22–28} The term hyperpolarization refers to a sample polarization, which drastically exceeds the thermal polarization predicted by Curie's Law for a given temperature T and magnetic field B_0 . Various hyperpolarization techniques utilize different physical effects to achieve signal enhancement up to a few orders of magnitude. Three main issues impeded the breakthrough of these techniques: (a) a limited polarization lifetime, (b) the necessity of external polarizer devices, and (c) its single-shot characteristics.

ULF MRS/MRI has the potential to overcome these three aspects. Zotev *et al.* reported a signal enhancement of up to 100 for a continuous hyperpolarization technique based on Overhauser dynamic nuclear polarization (ODNP).²² Also parahydrogen ($p\text{H}_2$) based hyperpolarization techniques such as signal amplification by reversible exchange (SABRE) are promising candidates for ULF MRS and MRI to boost the signal by several orders of magnitude.^{24–27,29} However, due to the fact that it is very difficult to synthesize a biocompatible catalyst, which is needed for SABRE, it will be difficult to realize the magnetization transfer from $p\text{H}_2$ to ligands *in vivo*. It will be more likely that $p\text{H}_2$ based hyperpolarization techniques work in a similar way as commercially available polarizers. Such devices produce hyperpolarized substances, which subsequently can be injected into a subject.³⁰

Both techniques, SABRE and ODNP, can be performed ideally in the ULF regime $B_0 < 10$ mT. This renders them as well suited tools for ULF MRS and MRI experiments. However, both hyperpolarization techniques require different chemical substances. On the one hand, the substrate of interest and, on the other hand, a catalyst for polarization transfer are required for SABRE, and an electron polarization source [e.g., free radicals in the form of 2,2,6,6-tetramethylpiperidinyloxy (TEMPO)] is required for ODNP. This has turned out to be a huge obstacle for the adaption of these techniques for *in vivo* applications because these solutions are not biocompatible so far. However, the potential benefits have attracted the attention of chemists, which has led to the development of new substances with the goal of biocompatibility. In order to investigate the hyperpolarizability of newly developed substances and transfer catalysts at extremely low magnetic fields, the aim was to develop and construct a ULF-MRS/MRI system using a DC SQUID as a detector. Here, a system is presented

that allows the combination of prepolarization and hyperpolarization. In the “Hardware and Methods” section, a detailed description of the instrument and its components is given. In the section titled “MRS and $p\text{H}_2$ based hyperpolarization,” the performance of the system and its ability to characterize SABRE experiments are shown. In the subsequent section the “combination of ODNP hyperpolarization with ULF MRI” is demonstrated, followed by the conclusions, and an outlook on further possibilities of the instrument.

HARDWARE AND METHODS

Figure 1 shows a schematic that contains all components necessary to perform ULF MRS/MRI experiments. The entire system is computer-controlled. The control software used to program MRS/MRI sequences and to manage data acquisition was realized with LabVIEW.³¹ The software gives the user full flexibility by offering access to all relevant sequence parameters like pulse duration, pulse frequency, pulse repetition rate, and sampling rate. The employed SQUID electronics (Magnicon XXF-1), which ultimately controls the SQUID, is set up and controlled by the Magnicon software SQUID-Viewer (v. 3.3.11).^{32,33} Additionally, the SQUID electronics controls, amongst other parameters, the activation of the flux locked loop (FLL) mode externally by means of transistor-transistor-logic (TTL) signals.

An analog-to-digital converter (ADC)/digital-to-analog converter (DAC) system from National Instruments is used to control the voltage-controlled current sources (VCCSs), the mechanical relays, and the SQUID electronics according to the programmed sequence. The currents connecting to the coils are fed into a commercially available magnetically and radio frequency (RF) shielded chamber³⁴ via screwable low pass filters.

For $p\text{H}_2$ -based hyperpolarization, the $p\text{H}_2$ is produced on demand on-site by an in-house developed $p\text{H}_2$ generator and fed into the chamber by silicone and polyethylene (PE) hoses. The sample is filled into a hyperpolarization chamber made of polyether ether ketone (PEEK). This allows the $p\text{H}_2$ to continuously bubble through the solution and to create hyperpolarization. For ODNP hyperpolarization, an RF coil is located next to or around the sample and tuned to the corresponding electron Larmor frequency.

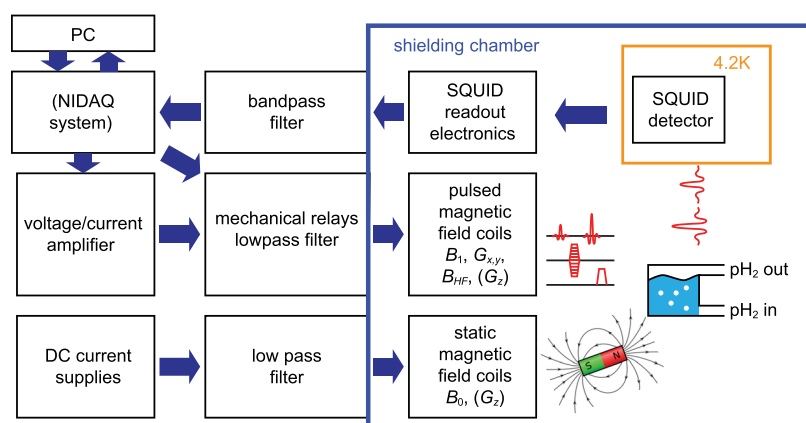


FIG. 1. Schematic overview flow chart of the ULF MRS/MRI system. The way the individual components interact with each other is indicated by the arrows.

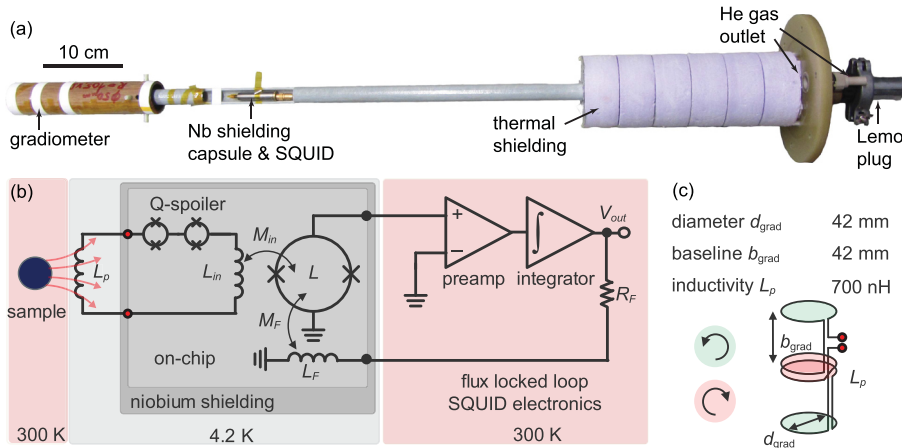


FIG. 2. Photograph (a) and schematic of the SQUID-based magnetic field sensor (b) and the pickup coil (c).

After the excitation pulses, the MRS signal arising from the sample is detected by the superconducting current sensor (SCS) and read out by the ADC system. The ADC system sends the data to the computer for further processing. Below, the individual components are explained in detail.

SQUID-based magnetic field sensor

The SQUID-based magnetic field sensor consists of two parts: the SQUID-based current sensor and the pickup coil. A photograph of the completely assembled sensor mounted on the dip-stick can be seen in Fig. 2(a).

The dip-stick is made of glass fiber reinforced polymer (GFRP) as far as possible. A thermal shielding, made of polystyrene [purple parts on the right-hand side of Fig. 2(a)], is implemented to minimize the heat input into the dewar and the evaporation rate. At the top end, besides a He gas outlet made of PEEK, a female Lemo plug socket (plug socket part number EGG.3B.324.CLL) is mounted where the Magnicon XXF-1 SQUID electronics will be inserted. In a simplified model, the SQUID electronics [Fig. 2(b)] consists of a pre-amplifier and an integrator. It feeds back the integrated signal V_{out} to the SQUID via the feedback resistor R_F and the feedback coil with inductance L_F coupled to the SQUID by the mutual inductance M_F . From the Lemo plug socket, the feed lines for the SQUIDs (shielded against RF interference by stainless steel braid) are running down into the Nb shielding capsule (Magnicon NC-1). Inside of the Nb capsule, a commercially available current sensor (Magnicon single-stage current sensor, type C6L1) is mounted (Magnicon CAR-1).

The pickup coil is mounted on the lower end of the dip-stick. It is realized by a wire wound second-order axial gradiometer [Fig. 2(c)]. The gradiometer body is made of a phenolic paper tube and has four machined grooves to guide the wire. It is wound from the enameled niobium wire with a $50 \mu\text{m}$ diameter (Goodfellow NB005100). Both the loop diameter d_{grad} and the gradiometer baseline b_{grad} are 42 mm. The effective area referred to the lowest loop of the gradiometer is found to be $A_{eff} = 5.4 \text{ mm}^2$. The system transfer function was found to be $V_{\phi,sys} = 0.44 \text{ V}/\Phi_0$. Here $\Phi_0 \approx 2.07 \times 10^{-15} \text{ V s}$ is the magnetic flux quantum.

Coil system

The coil system consists of coils that generate the stationary measuring field B_0 , the pulsed excitation field B_1 , the prepolarizing field B_p , and the three encoding gradient fields G_x , G_y , and G_z (see Fig. 3).

B_0 : Tetracoil

The coil generating the B_0 field has to meet various requirements. It has to produce a highly uniform magnetic field across the sample volume. The ratio between the overall size of the coil and the region of uniform magnetic field should be as small as possible to relieve the demands on the current source. Additionally, the sample, which will be placed in the geometric center of the coil, has to be easily accessible. A coil implementation, which fulfills all the requirements, was presented by Gottardi *et al.*³⁵ The final coil implementation uses one of the precalculated parameter sets of

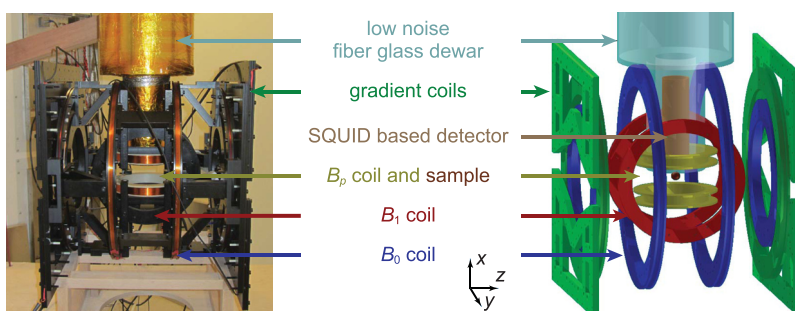


FIG. 3. Photo and schematic diagram of the coil system. For clarity, the schematic diagram shows only one of the two concave gradient coils.

Gottardi *et al.*,

$$a_1 = 0.6216 \times r_{\text{sphere}} = 161.62 \text{ mm},$$

$$b_1 = 0.7833 \times r_{\text{sphere}} = 203.66 \text{ mm},$$

$$a_2 = 0.9556 \times r_{\text{sphere}} = 248.46 \text{ mm},$$

$$b_2 = 0.2955 \times r_{\text{sphere}} = 76.83 \text{ mm},$$

$$N_1/N_2 = 80/121.$$

Here, the nomenclature of Ref. 35 is used with radius $r_{\text{sphere}} = 260$ mm. The manufactured and assembled coil can be seen in Fig. 3. The coil bodies are made of polyvinyl chloride (PVC) and are connected to a PVC-made supporting frame by glass-fiber reinforced screws. The coils have been wound using an enameled copper wire of 1 mm diameter. The complete tetracoil has an inductance $L_{B_0, \text{meas}} = 65.1$ mH, a DC resistance $R_{\text{DC}} = 12.2 \Omega$, and a current-to-field coefficient of $k_{B_0} = 0.66$ mT/A.

B_1 : Helmholtz coil

A Helmholtz coil creates the MR signal excitation pulses. This coil has a drastically smaller region of uniform magnetic field compared to a tetracoil. However, its field homogeneity is sufficient for an accurate excitation of spins. The excitation waveform usually is prepared such that it offers a certain bandwidth of 200–400 Hz around the center frequency f_0 ; therefore, small B_1 field inhomogeneities are negligible. The coil bodies are made of PVC. Each of the two coils consist of 4 windings of $\varnothing = 1.25$ mm thick enameled copper wire and has an effective radius $r_{B_1} = 186.5$ mm. The complete coil has an inductance of $L_{B_1} = 32.5 \mu\text{H}$, a DC resistance of $R_{B_1} = 0.25 \Omega$ (including ≈ 4 m twisted feed lines), and $k_{B_1} = 0.025$ mT/A. The coil is oriented such that its magnetic field is oriented perpendicularly to the B_0 field along the y -axis.

B_p : Prepolarization coil

For the polarizing coil, a Helmholtz configuration was chosen. A sample placed at the bottom of the dewar is in the geometric center of the coil. The tail of the dewar has to fit through the upper coil of the Helmholtz pair. As a result of this large Helmholtz coil implementation, the B_p field is much more homogenous than that of the previously used solenoid coil. Each of the coils has an effective diameter of $\varnothing_{B_p} = 166$ mm and holds 256 windings of an enameled copper wire of $\varnothing = 1.25$ mm. The assembled coil has an inductance $L_{B_p} = 41$ mH and a DC resistance $R_{B_p} = 4.1 \Omega$. Due to the large size, the current-to-field transfer coefficient is $k_{B_p} = 2.58$ mT/A. Since a thick wire was used, the coil can carry current up to 6 A. Due to the DC resistance and relatively large currents, a large amount of heat will be dissipated during operation. Therefore, the coil body is made of PEEK which provides a high glass-transition temperature of 143 °C. Alternatively fiber glass could have been used, which is more complicated to machine.

G_z : Maxwell coil

The gradient magnetic field $G_z = \partial B_z / \partial z$, which superimposes the B_0 magnetic field originating from the tetracoil, is created by a standard Maxwell coil arrangement consisting

of two identical coils separated by a distance $r_{G_z} \sqrt{3}$. The current in the respective coils flows in opposite directions. The gradient along the z -axis can be calculated using the formula,

$$\frac{dB_z}{dz} = 3\mu_0 INR^2 \frac{d}{(r_{G_z}^2 + d^2)^{5/2}},$$

where I is the applied current and N is the number of coil turns per coil. The coil bodies are made of PVC. Each of the two coils has a radius $r_{G_z} = 231$ mm and consists of 30 windings of $\varnothing = 0.315$ mm thick enameled copper wire which leads to $G_{z, \text{calc}} \approx 0.45$ mT/Am. The assembled coil has an inductance $L_{G_z} = 2.78$ mH and a DC resistance $R_{G_z} = 12.75 \Omega$.

G_x and G_y : Concave coils

To apply gradients in the x or y direction, various coil arrangements that approximate a linear magnetic field gradient are possible.^{16,36} The most common approach is to use a set of 4 rectangular coils per spatial dimension.^{19,37} Ruset *et al.* presented an improved version of the rectangular coils, where the coil shape was numerically optimized to yield a gradient more linear as the rectangular coil shape. The result is a coil where the wire next to the principal magnetic field axis (i.e., the z -axis) is of a slightly concave shape (see Fig. 3, the 4 outer green coil elements).³⁸ The coils are wound using 20 windings of $\varnothing = 1.25$ mm thick enameled copper wire. This leads to $L_{G_x} = 1.43$ mH, $L_{G_y} = 1.53$ mH and $R_{G_x} = 1.80 \Omega$, $R_{G_y} = 1.90 \Omega$. For both G_x and G_y , numerical simulations yield $G_{x,y, \text{sim}} \approx 0.183$ mT/Am. Table I summarizes the parameters of the coil system.

RF coil for ODNP hyperpolarization

For ODNP hyperpolarization, RF coils with a diameter of 30 mm are used. The coils can be connected to a tuning and matching circuit [see Fig. 4(a)]. With the adjustable capacitors (Voltronics Corporation, NMAJ40HV), the frequency can be tuned and the impedance matched to the input impedance [see Fig. 4(b)]. Since the tuning range was very limited (approximately 50 MHz), three different RF coils were fabricated to cover a range from 80 MHz to 250 MHz. The values for the different capacitors are listed in Fig. 4(c).

It turned out that the SQUID-based detector arrangement needs to be shielded from strong RF fields generated by these coils. Otherwise the Niobium wire of the gradiometer captures magnetic flux vortices. Our hypothesis is that after the switch-off of the RF field those vortices leave the niobium wire again on the time scale of several 10 ms–100 ms via flux creep.

TABLE I. Parameter overview table of the complete coil system.

	B_0	B_1	B_p	G_x	G_y	G_z
R_{DC} (Ω)	12.2	0.25	4.1	1.8	1.9	12.8
L (mH)	65.1	0.033	41.0	1.4	1.5	2.8
Wire \varnothing (mm)	1	1.25	1.25	1.25	1.25	0.315
Radius (mm)	161.6/248.5	186.5	83.0	231.0
Windings	80/121	4	256	20	20	30
k (mT/A)	0.66	0.025	2.58
G (mT/Am)	0.18	0.17	0.45

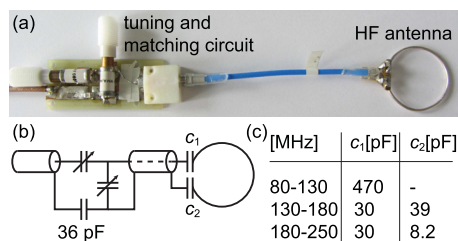


FIG. 4. Photo (a) and schematic diagram (b) of the RF coil. The table (c) shows the values for the capacitors.

This assumption is based on the fact that the observed transient was not decaying smoothly but showed jumps with an amplitude of Φ_0 . This non-acceptable delay can be prevented by shielding the complete dewar with a silver plated mylar foil. There was no increase in noise measured with the mylar foil, whereas other materials such as aluminum or copper foil increased the noise level significantly. The reason therefore is the Johnson-Nyquist noise inside electric conductors.^{39,40}

DAC/ADC system

For generating analog/digital output signals and acquiring analog input data, a National Instruments DAC/ADC system is used. For data acquisition and outputting MRS pulses, a NI PXIe-6363 and module is used.⁴¹ Due to the huge amount of control signals needed, e.g., for opening/closing the relays, a second PXI analog output module is required. A NI PXI-6738 module has been chosen. It offers 32 analog outputs that are capable of ± 10 V at 16 bit resolution and 1.00 megasamples/s.

Voltage controlled current sources

For DC magnetic fields, on the one hand, ultralow noise current sources are required to drive the coils that are either permanently turned on during the sequence (e.g., the B_0 field) or getting ramped quickly to a DC current value which has to be constant for a given time (e.g., the gradient coils). Current noise of the B_0 VCCS, for instance, directly affects the noise floor of the total setup. It is practically impossible to perfectly decouple B_0 from the pickup loop. Thus, current noise of the VCCS directly translates into B_0 noise, which then couples into the sensor and raises the noise floor. On the other hand, for the excitation pulses, VCCSs are needed that are able to drive fast changing signals through rather large coils (e.g., $L_{B_1} = 32.5 \mu\text{H}$). The current noise of these VCCSs is not critical since they are galvanically coupled to the system only during the pulses. One exception is the VCCS for the frequency encoding gradient G_z , which needs to be on during the data acquisition.

DC current sources

To drive the B_0 coil, a linear regulated bipolar current source (BCS) from HighFinesse⁴² as well as a battery driven home-made BCS is employed. The HighFinesse BCS is optimized for driving ultralow noise DC currents through highly inductive loads. It can deliver up to ± 3 A and ± 12 V. The output current drift is smaller than < 5 ppm/K.

The frequency encoding gradient G_z is driven by a heavily improved version of the current source presented in Ref. 43. It is a linear regulated bipolar current source with a sample-and-hold circuitry involving a voltage source mode. The amplifier can deliver up to 10 A and 100 V and has a current slew rate $\text{SR} = 0.1 \text{ A}/\mu\text{s}$ for an inductive load of $L_{G_z} = 2.8 \mu\text{H}$. During operation, the amplifier receives a desired set current value from the DAC and it operates as a high-power current source, i.e., its internal control loop controls the output current by measuring the voltage drop across a low-ohmic shunt resistor in series to the coil. As soon as the output current has settled to the steady state (i.e., the set current value), the amplifier changes the internal control loop to a voltage controlled sample-and-hold control loop. Therefore, the voltage drop across the coil for the steady state set current is measured by the discrete sample-and-hold circuit solution and is stored in a polypropylene type low leakage capacitor. Due to the low charge leakage of the capacitor and the high input impedance of the sample and hold circuit ($Z_{\text{in}} > 10 \text{ G}\Omega$), holding times of the stored voltage of 10 s can be achieved. The result is an ultralow noise current flowing through the coil. The current noise in the sample-and-hold mode $S_{i,SH}^{1/2}$ is given by the voltage noise of the sample-and-hold circuit $S_{v,SH}^{1/2}$ divided by the impedance of the coil and the shunt resistor: $S_{i,SH}^{1/2} = S_{v,SH}^{1/2} / (R_{\text{shunt}} + R_{\text{DC,coil}} + i\omega L_{\text{coil}})$. The holding time of this ultralow noise mode, however, is practically limited to two or 3 s with a duty cycle $< 50\%$. The reason for this limitation is the Joule heating of the coil windings and the resulting resistance change. This leads to a DC offset of the set current that increases with increasing holding time and current since the voltage across the coil is kept constant.

Broadband amplifier

The B_1 coil is driven by a modified stereo audio amplifier (60-120D DOLIFET SE from ABACUS) or alternatively by a 4-quadrant amplifier (TOE 7621-60 from Toellner).^{44,45} Since both amplifiers are driven as voltage sources, an additional ohmic load of 4 Ohm is added in series to the coil circuit to minimize the phase difference between the control signal and the actual output voltage.

A Kepco BOP 100-4 ML linear regulated bipolar current source is used to drive the B_p coil.⁴⁶ It is especially designed to drive heavy inductive loads and can deliver up to ± 4 A and ± 100 V.

The $G_{x,y}$ gradient coils are powered by Dr. Hubert A1110-16-QE precision power amplifiers.⁴⁷ It has an output capability of up to ± 28 A and ± 75 V, a bandwidth from DC to 200 kHz, and a slew rate $\text{SR} = 100 \text{ V}/\mu\text{s}$.

The RF coil for ODNP hyperpolarization is driven by a broadband RF amplifier of the type FLH-50A from Frankonia.⁴⁸ The frequency band ranges from 1 MHz to 1 GHz and has a maximum output power of 50 W. The signal for the RF amplifier is generated by a synthesizer (HAMEG HM8134-3).

Relay switches

The broadband current sources that drive the coils for pulsed magnetic fields are optimized for high output power

to precisely produce the desired waveform. This comes at the price of increased current and voltage noise densities of the amplifier output stage. Even when the output current of the broadband VCCS is set to zero, the output noise current/voltage is large enough to completely overload the SQUID. A simple yet effective way to get rid of this problem completely is to disconnect the noisy amplifiers galvanically from the coil system when they are not needed. This has been achieved by means of mechanical relays, which have the advantage over MOSFETs of a higher isolation resistance.

For the B_1 coil, relays from Gigavac (GR3BJA335) were implemented.⁴⁹ They are rated for $V_{\max} = 160$ V and $I_{\max} = 3$ A and have short closing ($100 \mu\text{s}$) and release times ($200 \mu\text{s}$). For the high current gradients $G_{x,y}$, the automotive relays TE Connectivity 2-1904058-5 are used.⁵⁰ They are rated for $V_{\max} = 400$ V and $I_{\max} = 20$ A. Due to the huge current carrying capability, high mass contacts are used which drastically increase the switching times (closing: 2.5 ms, release: 1 ms).

To decouple the RF amplifier galvanically from the coil system, only the middle conductor of a coaxial line is separated by a mechanical relay (Radiall MICRO-SPDT 8 GHz MO 12 V part# R596812100), while the ground connection still remained. The switching time for closing the contact is <4 ms and for breaking the contact <1 ms.

Low pass feed-through filters

The RF shielded cables connecting the VCCSs and the coils have to be fed into the shielding chamber without impairing the shielding effect. Tesch 02000203 feedthrough filters are used for the DC coils.⁵¹ They have a Π filter topology consisting of two capacitors $C_{\Pi} = 250$ nF and one inductor $L_{\Pi} = 1.5 \mu\text{H}$, have a cutoff frequency $f_{-3\text{dB}} = 180$ kHz, and are rated for 16 A and 250 V.

For all other coils, Tesch 02000207 filters are employed.⁵¹ They are also realized by a Π filter topology consisting of two capacitors $C_{\Pi} = 5$ nF and one inductor $L_{\Pi} = 0.4 \mu\text{H}$. They have a cutoff frequency $f_{-3\text{dB}} = 2.5$ MHz and are rated for 30 A and 600 V. The increased bandwidth of $f_{-3\text{dB}} = 2.5$ MHz is of importance. Since the gradient current profiles ideally are of the trapezoidal shape, high-frequency components have to be present to achieve the sharp transitions needed from the linearly rising/falling current to the steady state constant current.

Hyperpolarization chamber for pH_2 hyperpolarization

To bring the pH_2 in contact with the catalyst and the target molecule in a controlled manner, a small hyperpolarization chamber was designed that allows for convenient handling during experiments. Figure 5 shows a cross section and a photo of the realized hyperpolarization chamber. It is made of PEEK and has a lateral side length $l_0 = 25$ mm and a total height $h_0 = 30$ mm. The inner volume has a diameter $\varnothing_i = 10$ mm and an inner height $h_i = 24.5$ mm, giving a sample volume $V = 1.9$ ml.

A pH_2 inlet is located at the left bottom side of the container.

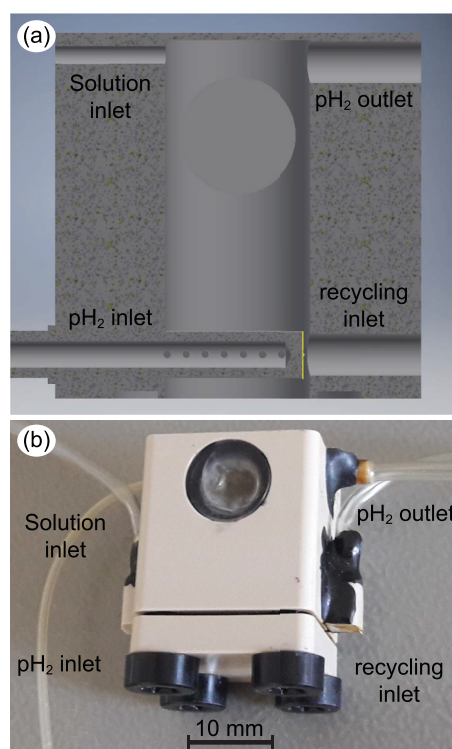


FIG. 5. Hyperpolarization chamber. (a) Cross section of the CAD drawing of the hyperpolarization chamber. (b) Photograph of the fully assembled container.

At the top side, there are two differently sized holes. The smaller one [cf. the left side of Fig. 5(a)] is the solution inlet (solution inlet diameter 1.5 mm). A polytetrafluoroethylene (PTFE) hose glued (glue used: Henkel Loctite Stycast 2850 FT) into the solution inlet is connected to a syringe, which is used to both press the solution into the container as well as a solution-storage reservoir for long term measurements where refilling of the container is necessary on a regular basis. The larger hole on the opposite side has a diameter of 3.0 mm and is used as the pH_2 outlet. A Polyurethane (PUR) hose glued into the pH_2 outlet leads to a collecting basin (not shown). The basin is an indispensable feature of the hyperpolarization chamber. Due to the slight excess pressure within the container, the solution will be pushed out of the pH_2 outlet. This fluid is collected in the collecting basin. The basin is wide enough so that the solution will stay, but the exhaust pH_2 gas can escape. At the basin, a second PUR hose is connected, which is running to the hole on the bottom right in Fig. 5(a). This allows pushed-out solution to flow back from the basin into the container. This measure increased the container refilling intervals drastically (compared to prototype container implementations without a recycling system).

pH_2 generator

To perform MRS experiments using pH_2 based hyperpolarized contrast agents, the experiment ideally should be supplied with $\sim 100\%$ enriched pH_2 to maximize the signal enhancement. A high conversion rate can be obtained when the thermal equilibrium mixture of pH_2 and orthohydrogen (oH_2) will be cooled to cryogenic temperatures in the

presence of a catalyst.⁵² For this purpose, a $p\text{H}_2$ generator has been developed that allows for convenient $p\text{H}_2$ production in a laboratory environment. Various $p\text{H}_2$ generator designs are suggested in the literature^{53–55} or are even commercially available.⁵⁶ All generator implementations employ a cryo-cooled paramagnetic catalyst that gets in contact with H_2 . The generator layout follows the design of Juarez *et al.*⁵⁴ Figure 6 shows a technical drawing and the flow scheme of the $p\text{H}_2$ generator.

It is designed as a dip-stick which can be flanged (flange type: KF25) and immersed into a liquid helium transport vessel. At the H_2 inlet, a precision dosing valve is mounted (Parcom M6A-H1L-V-SS-TC) for gas flow regulation. At the outlet of the generated $p\text{H}_2$, a block valve is mounted [cf. Fig. 6(b)] that seals the generator air-tight when not in use. The catalyst is housed in a cartridge in the stick at the bottom end of the outlet pipe. A temperature sensor and a heater resistor are located close to the catalyst cartridge. Two safety valves, one in the inlet branch and one in the outlet branch, ensure a safe operation. A block valve connected to the inlet pipe allows for convenient evacuation of the generator.

The riser pipe consists of two coaxial stainless steel pipes nested into each other ($\varnothing_{\text{inner}} = 12$ mm and a wall thickness $d_{\text{inner}} = 0.25$ mm as well as $\varnothing_{\text{outer}} = 18$ mm and $d_{\text{outer}} = 0.5$ mm). At the lower end of the inner pipe (i.e., the start of the outlet pipe), the cartridge made of gold plated copper is screw-mounted. The cartridge has a volume of $\sim V_{\text{cat}} = 3$ cm³ and houses the catalyst granulate (iron(III)oxide hydrate, mesh size 30–50 μm , Sigma-Aldrich 371254-50G). The bottom end is perforated by 4 holes ($\varnothing = 3$ mm), which allows the H_2 to enter the cartridge. The holes are covered by a metal mesh to prevent the catalyst granulate from pouring out of the cartridge. The cartridge is nested in a cup made of gold plated copper that is soldered onto the outer pipe.

Between cartridge and cup, there is a small gap, which allows H_2 gas to pass the cartridge and enter it by the bottom holes. The cooled, converted gas is streaming upwards in the inner riser pipe, thereby cooling the pipe which subsequently cools inflowing H_2 [cf. the bottom right part of Fig. 6(a)]. Thereby, the heat introduced by the inflowing H_2 is reduced and the helium consumption is minimized. A temperature diode (standard 1N4448 diode) and a heater resistor

are glued (glue used: GE Varnish VGE7031) into the bottom of the cup covering the cartridge. The 1N4448 diode shows very linear current-voltage characteristics in the temperature range of interest (25 K–100 K). The catalyst temperature is monitored and controlled by a home-made temperature controller unit.

The conversion efficiency of the generator was determined by a home-made thermal-conductivity detector (TCD) built from a reworked standard light bulb in a temperature-controlled housing. It was thermally insulated using Armaflex. A different $p\text{H}_2$ generator (not presented in this work) was used for the reference measurement of the TCD. The contact time of the gas with the catalyst in this generator was about 20 min, ensuring that the $\text{oH}_2/p\text{H}_2$ achieves equilibrium composition of 50.2% at $T = 77$ K. The voltage output of the TCD was set as the reference value for $\text{oH}_2/p\text{H}_2$ of 50.2%. Subsequently, the $p\text{H}_2$ generator described above was characterized by operating it with the same flow rate as the reference measurement at various temperatures above the condensation temperature of hydrogen of 21 K, while acquiring the TCD voltage output. A maximum $p\text{H}_2$ concentration of above 90% for the iron(III)oxide hydrate catalyst was received, while activated charcoal as a catalyst only achieved a $p\text{H}_2$ concentration of 48%. Hövener *et al.* also reported a much higher conversion efficiency after replacing activated charcoal with iron(III)oxide hydrate.⁵⁷ The $p\text{H}_2$ concentration was not maximized any further by means of larger iron(III)oxide hydrate catalyst volumes. During the TCD characterization and NMR measurements, the typical flow rate was $dV/dt = 1.5$ – 2.5 l/h, thus the $p\text{H}_2$ concentration was at least 90%.

Low noise helium dewar

To provide the temperature environment for the SQUID-based magnetic field detector to operate ($T < T_{c,\text{Nb}} = 9.26$ K), a GFRP dewar and liquid helium is employed. The dewar, Cryoton type LH-11.5-NTE,⁵⁸ holds up to 11.5 l of liquid helium and has a helium boil-off rate ≈ 1 l/day (for insulation vacuum pressures $p < 1.0 \times 10^{-5}$ mbar). It offers an ultralow noise performance of $S_B^{1/2} < 0.5$ fT/Hz^{1/2}. The residual magnetic field noise arises from noise currents present in the one-layer gold plated Mylar thermal insulation foil, which is incorporated in the dewar. The dewar is placed right next to the geometric

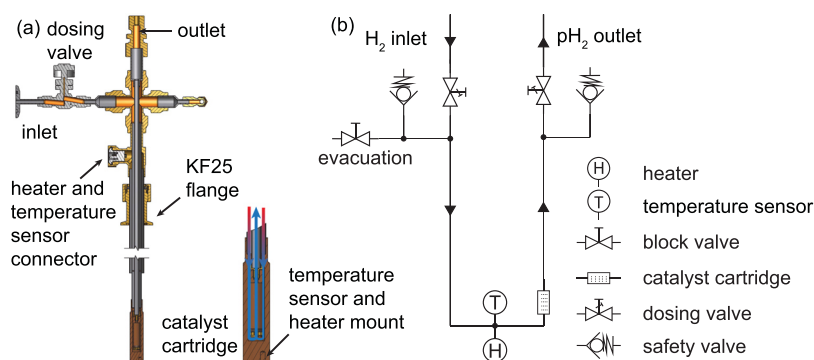


FIG. 6. Technical drawing (a) and schematic layout (b) of the $p\text{H}_2$ generator.

TABLE II. Shielding factors of the three layered shielding chamber.

f (Hz)	Shielding factor
DC	>10 000
$0.01 < f < 1$	>100
$1 < f < 10$	>1000
$10 < f < 100$	>15 000
$100 < f < 1000$	>50 000
>1000	>100 000

center of the coil system where the sample is located, offering a hot-to-cold distance of $d_{hc} = 12$ mm.

Magnetic shielding

Due to the broadband characteristics of the SQUID-based magnetic field detector, it is not enough to shield the detector only within the operation bandwidth. In fact, shielding from the DC range up to the GHz range is necessary. To shield the SQUID sensor from low-frequency magnetic fields (e.g., magnetic fields originating from the elevator ~ 10 m away), from quasi-static magnetic fields like the earth's magnetic field and from high-frequency noise, the detector arrangement (cf. blue frame in Fig. 1) is situated inside a commercially available three-layered, cubic shielding chamber with an inner side length of 2.6 m.³⁴ For shielding DC and low-frequency noise, two μ -metal layers are used. For shielding HF noise, one Al layer is used. The inner shell consists of a 3 mm thick μ -metal layer. To minimize eddy currents, which arise from fast changing magnetic fields from, e.g., the switching of the polarizing coil, this layer is made of 4 single layers, each with a thickness of 0.75 mm. The middle shell consists of 8 mm thick Al. The outer shell is made of 4 layers of 0.5 mm thick μ -metal resulting in a thickness of 2 mm. The shielding factor for different frequency ranges is listed in Table II.

Imaging methods

For acquiring images with the ULF MRI setup, we used simple spin echo (SE) and gradient echo (GRE) sequences (cf. Fig. 7).

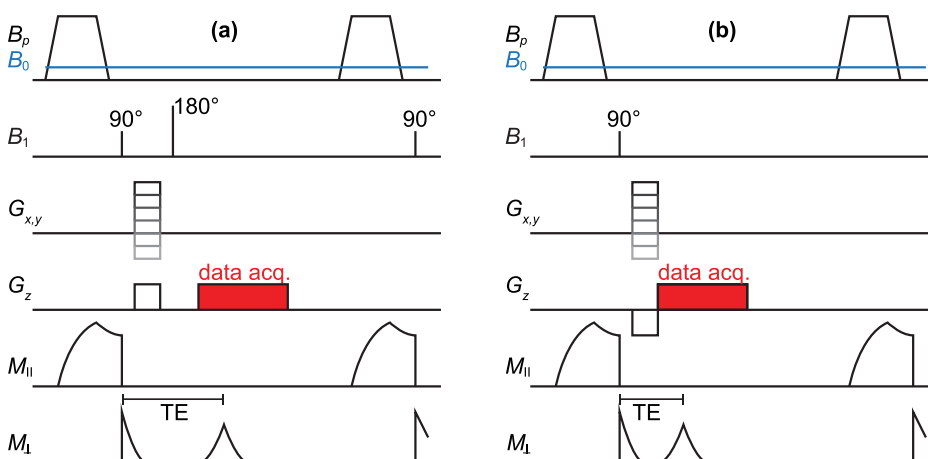


FIG. 7. Spin echo (a) and gradient echo (b) imaging sequences.

The sequences start with a prepolarizing pulse B_p . During this pulse, the sample is irradiated with the ODNP RF field and hyperpolarized. After switching off the polarizing field, a 90° pulse flips the magnetization in the transversal plane followed by a 180° pulse or a sign-flipping gradient generating the echo. An additional phase gradient is switched on directly after the 90° pulse. After the readout of the echo, the sequence starts again until all phase encoding steps are acquired. Note that the rapid switching of the frequency-encoding gradient was made possible by the home-made low-noise amplifier.

MRS AND pH_2 -BASED HYPERPOLARIZATION

In this section, the noise performance of the SQUID-based MRS system is described and its ability to quantitatively measure MR signal intensities. It is also demonstrated that the system is a well suited platform to conduct pH_2 -based hyperpolarization experiments such as SABRE.

Magnetic field noise

The magnetic field noise performance of the coil system can be seen in Fig. 8(a). The blue curve shows the pure noise floor of only the dewar and the SQUID inside the shielding chamber, which leads to a white noise level in the range of interest above 5 kHz of $S_B^{1/2} \approx 0.6$ fT/Hz^{1/2}. When placing the coil system around the dewar, the white noise level increases to $S_B^{1/2} \approx 1.1$ fT/Hz^{1/2}.

Once the home-made battery-driven B_0 -BCS source is turned on, the noise level is increased drastically in the low-frequency region of the spectrum [Fig. 8(a) green curve] with a peak at 250 Hz. The noise level in the frequency range of interest ($f > 5$ kHz) increases slightly but is still below $S_B^{1/2} \approx 1.1$ fT/Hz^{1/2}. The B_p and B_1 amplifiers show no significant additional contribution to the noise spectra in the range < 80 kHz, due to the open mechanical relays separating them galvanically from the experiment. This configuration was used for MRS experiments.

For MRI and ODNP experiments, the RF amplifier and the gradient amplifiers need to be turned on [Fig. 8(a) red curve]. The RF amplifier and the amplifiers for the phase encoding gradients showed no significant increase in noise due to the

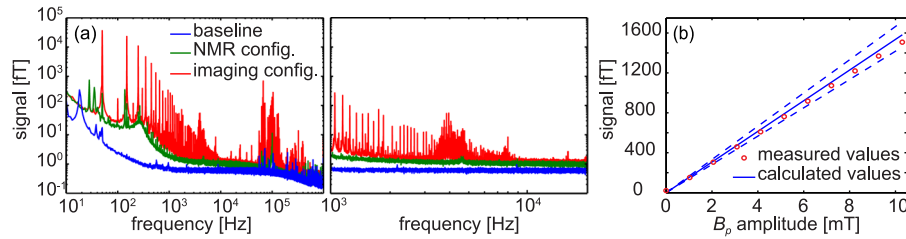


FIG. 8. (a) Noise spectra of the system. The blue curve is the noise level of the SQUID-based detector without the MRI coil setup in place. The green curve shows the spectrum with the MRI coil system in place, and all amplifiers necessary for MRS experiments are active. The red curve shows the noise spectrum of the MRI setup with active gradient amplifiers. (b) Comparison of measured (red circles) and calculated (blue line) MR signal strength in units of fT. The dashed blue lines represent the calculated MR signal strength with ± 1 mm offset of the sample.

mechanical relays, which separate them galvanically from the coil system during the SQUID readout. However, by turning on the home-made amplifier for the frequency encoding gradient, the region below 5 kHz becomes noisy. There is a broad noise peak around 4 kHz, and there are strong harmonics of the 50 Hz main power. The noise level in the bandwidth of interest around 5.5 kHz is slightly increased but still below $S_B^{1/2} \approx 1.4$ fT/Hz^{1/2}. Between 10 kHz and 11 kHz, the noise is slightly lower at $S_B^{1/2} \approx 1.2$ fT/Hz^{1/2}. The spectrum rolls off at $f_{-3dB} \approx 160$ kHz.

Quantitative analysis of the MR signal amplitude

One advantage of the SQUID-based detector is its ability to measure changes in the magnetic flux, unlike rf coils that are sensitive to dB/dt . This enables the measurement of the MR signal strength in absolute units of fT, independent of the frequency. For a given geometry of the gradiometer and for a homogenous sample, the detected field strength can be calculated via⁵⁹

$$B_{\text{det}} = \frac{1}{A_p} \int_{\text{phantom}} \beta_{\perp}(\mathbf{r}) M_{\text{sample}} dV, \quad (1)$$

where A_p is the area of the pickup loop. The magnetization M_{sample} can be calculated via Curie's law $M_{\text{sample}} = \rho_{\text{sample}} \gamma^2 \hbar^2 B_p / 4k_B T$, where ρ_{sample} is the proton spin density, γ is the gyromagnetic ratio, \hbar is the Planck constant, k_B is the Boltzmann constant, and T is the temperature of the sample. $\beta_{\perp}(\mathbf{r})$ is the component of the receive field, which is perpendicular to the precession field and can be calculated analytically as described in Ref. 60.

For the verification of this approach, we built a cylindrical water phantom with a diameter and height of 25 mm. The phantom was placed directly under the dewar. The distance between the upper part of the phantom and the lowest loop of the pickup coil was (14 ± 1) mm. Additionally a signal loss of 10% was assumed due to a non-perfect adiabatic switch-off of the polarizing coil, which is oriented perpendicularly to the B_0 coil. The 10% loss results from numerical simulations of the signal decay based on the Bloch equations. The calculated signal strength is compared with the signal strength of measured spectra of the water phantom, which is gained by integrating the area under the MRS peak [see Fig. 8(b)]. The measurements were performed with a free induction decay (FID) sequence, which consists of a 20 s prepolarizing pulse followed by a 90° pulse and the data acquisition at a field

strength of 120 μ T. After the long prepolarizing pulse, it was assumed that the magnetization of the water is in thermal equilibrium at the B_p field strength. The measurements were in good agreement with the calculated values.

pH₂-based hyperpolarization

The advantages of the SQUID-based MRS system compared to field-cycling systems used for high-field MRS spectroscopy of heteronuclei as described, e.g., in Refs. 61 and 62, include the use of a broadband detector, which can detect different nuclei at the same time. Also, the open geometry of the ULF MRI system allows the easy installation of hyperpolarization chambers with inputs and outputs for the pH₂ supply. The hyperpolarization chamber does not have to be moved, enabling imaging of larger sample volumes.

Even though it is not possible to resolve chemical shifts at ULF, it is easy to reach a linewidth of the MRS signal below 1 Hz due to the fact that field inhomogeneities scale with the magnetic field strength.¹⁸ This enables to resolve heteronuclear J coupling without additional shimming efforts although it is possible to shim the B_0 field with the implemented gradient coils. The possibility to measure, e.g., two dimensional spectra of ligands containing two different nuclei, which are hyperpolarized with pH₂ and where J coupling can be resolved, helps to find out polarization transfer processes between the different nuclei.

The SNR of a SQUID-based system is much smaller than the SNR of field-cycling high-field MRS systems, but it is increased compared to ULF MRS systems using Faraday detection coils as presented in Ref. 24. However, the SQUID-based detector needs a heavily shielded room, which makes it not as cost efficient.

As an example for the ability of a quantitative study, the magnetic field dependence of SABRE is shown in Fig. 9(a). The hyperpolarization chamber was filled with 11.9 μ L 3-fluoropyridin and 6.2 mg Crabtree catalyst⁶³ dissolved in 6 ml methanol. For the measurement, pH₂ was bubbled with a rate of 1.5 l/h through the hyperpolarization chamber. The sequence used was a simple FID sequence consisting of a prepolarization pulse with a length of 4 s and variable magnitude between 0 and 15 mT, followed by a 90° pulse and the data acquisition. During the whole experiment, the B_0 field (122 μ T) was on. Figure 9(a) shows the real part of the signal $\text{Re}(\text{SI})$. Additionally a high-resolution spectrum is shown in Fig. 9(b). The spectral resolution without additional shimming

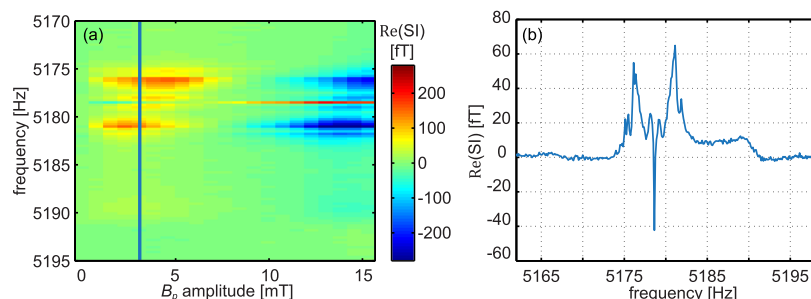


FIG. 9. B_p dependence of the polarization transfer effect of 3-fluoropyridine and Crabtree catalyst dissolved in methanol (a). In (b), a spectrum for a hyperpolarization field of 3 mT is shown [indicated by the vertical blue line in (a)].

is <0.5 Hz. The spectrum was acquired at a hyperpolarization field of $B_p = 3$ mT, indicated by the vertical blue line in Fig. 9(a). The negative peak at around 5178.5 Hz is most likely due to hyperpolarized methanol. The result is in good agreement with previous published data using the Crabtree catalyst.⁶⁴

It is easy to modify the sequence to get further useful information on the hyperpolarization process. For example, by varying the length of the prepolarizing pulse, the hyperpolarization build-up time can be gained. Due to the easy access to the hyperpolarization chamber, it is easy to investigate different sample compositions. A detailed study with this ULF MRS system is shown in Ref. 27.

COMBINATION OF ODNP HYPERPOLARIZATION WITH ULF MRI

An easy method to continuously increase the SNR without strong polarizing pulses (>20 mT) is ODNP-based hyperpolarization. Compared to pH_2 -based hyperpolarization techniques, reaching biocompatibility seems much more feasible with the free radicals, needed for ODNP. Amplification factors of >50 can easily be reached, which might enable unique experiments such as, for example, cerebral blood volume based fMRI at ULF, if realized *in vivo*.^{65–67} An amplification factor of 50 at a field strength of 10 mT would correspond to a prepolarization field of 0.5 T. Such strong prepolarization fields have not been realized in ULF MRI experiments. Eddy currents in the RF shielding of the system,¹⁶ Nyquist noise of the polarization coil, which needs to be situated in proximity to the SQUID-based detector and switching-time limits on *in vivo* experiments make large and strong polarizing coils difficult to implement.⁶⁸ The implementation of the RF coil for ODNP is an easy task in comparison. However, one must be careful with heating of the sample due to the RF field. We already reached good amplification factors by irradiating the sample with 8 W and a duty cycle of 1:1. This irradiation power is in the range of *in vivo* experiments as shown in Refs. 22, 68–70, where a 9 W irradiation with a duty cycle of 1:1 was used.

ODNP needs the presence of free electrons, which can be injected into biomaterials as free radicals. Free radicals are usually far from being biocompatible due to their reactive nature. However, they can be integrated into larger molecules, which shield the free radical from large biomolecules, still allowing small water molecules to access them. Due to a large variety of applications in electron spin resonance (ESR), MRS, and MRI, the development of such biocompatible, stable, and

efficient free radicals is a research branch of its own.⁷¹ The system presented here is an optimal tool for the quantitative investigation of these free radicals since larger sample volumes can easily be penetrated by the RF field due to the penetration depth of several cm at ultralow-fields. Additionally, the use of a SQUID allows the measurement of absolute signal intensities making the comparison of different samples easy.

Imaging results

With the sequences described above, we were able to acquire the first *ex vivo* images of a dead rat. 5 ml of commercially available carboxy proxyl (CP) free radicals dissolved in water with a concentration of 2.5 mM/l was injected into the belly of the rat. The RF coil was placed right next to the injection point. For orientation, we also attached two markers on the other side of the RF coil [cf. Fig. 10(a)].

In Fig. 10(b), a hyperpolarized GRE image is shown. The image was acquired at $545 \mu\text{T}$ with a 4.45 mT polarizing pulse of 450 ms duration. The microwave power was 7 W at 180 MHz. The magnitude of the frequency encoding gradient was 0.175 mT/m and 0.9 mT/m for the largest phase encoding gradient 0.9 mT/m. The acquisition time for each phase encoding step was 131 ms. The repetition time (TR) was 900 ms, and the total duration for the 37×37 phase encoding steps was 60 min. These parameters result in an isotropic nominal resolution of about 1 mm.

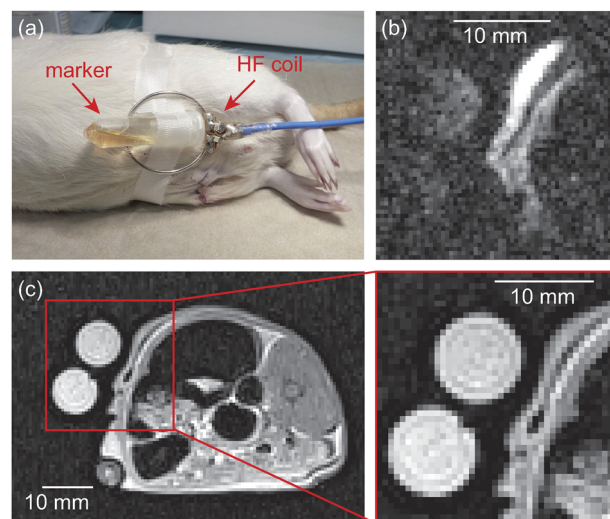


FIG. 10. Photo of the position of the RF coil and marker on the rat (a), ODNP enhanced ULF (b), and high field (c) *ex vivo* MR image of a dead rat.

For comparison, we also acquired an image with a commercial 3 T MRI scanner (Siemens PRISMA) [cf. Fig. 10(c)]. A standard 2D TSE sequence was used. The resolution was similar to the ULF image, and the overall acquisition time was 2 min 35 s.

The comparison of the two images shows a very good agreement of the anatomical structure. However, the image acquired at ULF shows only signals where free radicals are located. The experiment demonstrates that with free radicals in mM concentration it is possible to acquire anatomical images with high resolution. Inside of the rat's body, the radicals stayed stable for more than 1 h. We expect that the lifetime of the CP radicals will decrease drastically in living tissue. Therefore, the development of biocompatible and stable free radicals is necessary to perform *in vivo* experiments with ODNP-enhanced ULF MRI.

CONCLUSIONS

We presented an ULF MRS and MRI system with an open geometry and an easily accessible sample volume for the combination with hyperpolarization techniques, such as SABRE and ODNP. The system offers the possibility to perform gradient and spin echo sequences, owing to a home-built low-noise gradient amplifier for the frequency encoding gradient coil. For the detection of the MR signal, we used a SQUID coupled to a second order gradiometer. The broadband characteristics of the SQUID allow simultaneous detection of different nuclei and thus potentially investigations of internuclear polarization transfer mechanisms, e.g., ^{19}F and ^1H , which was demonstrated in Ref. 27. Also, a very low noise level of the SQUID below $\sim 1.4 \text{ fT/Hz}^{1/2}$ and the ability to measure the MR signal strength in absolute units of fT turns the instrument into a platform for quantitative characterization of hyperpolarization techniques and allows the comparison of different hyperpolarization agents and polarization conditions as well as internuclear transfer processes.

The feasibility of performing *in vivo* experiments with the combination of ULF MRI with ODNP hyperpolarization techniques was also demonstrated. First, *ex vivo* results with commercially available contrast images were shown, using GRE sequences.

OUTLOOK

The initial goal of building this system was to create a flexible platform for the investigation of the mechanisms related to the pH_2 hyperpolarization technique SABRE. The main mechanism for the magnetization transfer at low fields is coherent spin mixing.^{72,73} Coherent spin mixing leads to the picture of energy level anticrossing (LAC).⁷⁴ Up to now, the theory is only verified qualitatively.⁵⁵ With the new SQUID-based ULF MRS unit, we hope to get a much better understanding of the theory behind SABRE and to quantitatively verify the LAC theory. A detailed understanding of this theory can help to develop more efficient solvent, catalyst, and ligand systems needed for SABRE.

Furthermore, the current system allows for an easy implementation of SABRE-SHEATH (Signal Amplification by

Reversible Exchange in SHield Enables Alignment Transfer to Heteronuclei) experiments, due to the very good shielding factor of the magnetically shielded room.^{75–77}

During the construction, it turned out that the implementation of a unit for ODNP can easily be realized. This technique is a promising candidate for continuous *in vivo* hyperpolarization. After our success with *ex vivo* imaging using continuous ODNP hyperpolarization, the logical next step is to perform continuous *in vivo* imaging techniques. However, the bottleneck of this technique is the lack of biocompatible, efficient, and stable free radicals. Therefore, the ULF MRI system is used as a platform for the investigation of the ODNP performance of novel free radicals.

ACKNOWLEDGMENTS

M.P./J.B. thank the Deutsche Forschungsgemeinschaft (Grant No. DFG BE 1824/12-1) for the financial support. K.B./T.S. thank Koos Zevenhoven for providing schematics of their gradient amplifier.

- ¹P. A. Rinck, *Magnetic Resonance in Medicine*, 12th ed. (ABW Wissenschaftsverlagsgesellschaft, 2018).
- ²W. Lu, K. B. Pauly, G. E. Gold, J. M. Pauly, and B. A. Hargreaves, *Magn. Reson. Med.* **62**, 66 (2009).
- ³K. M. Koch, J. E. Lorbiecki, R. S. Hinks, and K. F. King, *Magn. Reson. Med.* **61**, 381 (2009).
- ⁴R. E. Sepponen, *Acta Radiol.* **37**, 446 (1996).
- ⁵V. S. Zotev, A. N. Matlashov, P. L. Volegov, I. M. Savukov, M. A. Espy, J. C. Mosher, J. J. Gomez, and R. H. Kraus, *J. Magn. Reson.* **194**, 115 (2008).
- ⁶P. E. Magnelind, J. J. Gomez, A. N. Matlashov, T. Owens, J. H. Sandin, P. L. Volegov, and M. A. Espy, *IEEE Trans. Appl. Supercond.* **21**, 456 (2011).
- ⁷P. T. Vesanen, J. O. Nieminen, K. C. J. Zevenhoven, J. Dabek, L. T. Parkkonen, A. V. Zhdanov, J. Luomahaara, J. Hassel, J. Penttilä, J. Simola, A. I. Ahonen, J. P. Mäkelä, and R. J. Ilmoniemi, *Magn. Reson. Med.* **69**, 1795 (2013).
- ⁸R. Körber, J. H. Storm, H. Seton, J. P. Makela, R. Paetau, L. Parkkonen, C. Pfeiffer, B. Riaz, J. F. Schneiderman, H. Dong, S. M. Hwang, L. You, B. Inglis, J. Clarke, M. A. Espy, R. J. Ilmoniemi, P. E. Magnelind, A. N. Matlashov, J. O. Nieminen, P. L. Volegov, K. C. J. Zevenhoven, N. Höfner, M. Burghoff, K. Enpuku, S. Y. Yang, J. J. Chieh, J. Knuutila, P. Laine, and J. Nenonen, *Supercond. Sci. Technol.* **29**, 113001 (2016).
- ⁹M. Mölle, S. I. Han, W. R. Myers, S. K. Lee, N. Kelso, M. Hatridge, A. Pines, and J. Clarke, *J. Magn. Reson.* **179**, 146 (2006).
- ¹⁰K. L. Seung, M. Mölle, W. Myers, N. Kelso, A. H. Trabesinger, A. Pines, and J. Clarke, *Magn. Reson. Med.* **53**, 9 (2005).
- ¹¹S. Busch, T. Wong, M. Moessle, M. Hatridge, J. Simko, A. Pines, and J. Clarke, in *Proceedings of the 16th Scientific Meeting International Society of Magnetic Resonance in Medicine 2008* [*Magn. Reson. Med.* **67**, 1138 (2012)].
- ¹²W. Myers, D. Slichter, M. Hatridge, S. Busch, M. Mölle, R. McDermott, A. Trabesinger, and J. Clarke, *J. Magn. Reson.* **186**, 182 (2007).
- ¹³I. M. Savukov, V. S. Zotev, P. L. Volegov, M. A. Espy, A. N. Matlashov, J. J. Gomez, and R. H. Kraus, *J. Magn. Reson.* **199**, 188 (2009).
- ¹⁴M. P. Ledbetter, T. Theis, J. W. Blanchard, H. Ring, P. Ganssle, S. Appelt, B. Blümich, A. Pines, and D. Budker, *Phys. Rev. Lett.* **107**, 107601 (2011).
- ¹⁵J. Clarke and A. I. Braginski, *The SQUID Handbook* (Wiley-VCH Verlag GmbH & Co. KGaA, 2005).
- ¹⁶P. V. Robert Kraus, M. Espy, and P. Magnelind, *Ultra-Low Field Nuclear Magnetic Resonance: A New MRI Regime*, 1st ed. (Oxford University Press, 2014).
- ¹⁷See www.quspin.com for Quspin.
- ¹⁸J. Clarke, M. Hatridge, and M. Mölle, *Annu. Rev. Biomed. Eng.* **9**, 389 (2007).
- ¹⁹V. S. Zotev, A. N. Matlashov, P. L. Volegov, A. V. Urbaitis, M. A. Espy, and R. H. Kraus, *Supercond. Sci. Technol.* **20**, S367 (2007).

- ²⁰V. S. Zotev, P. L. Volegov, A. N. Matlashov, M. A. Espy, J. C. Mosher, and R. H. Kraus, *J. Magn. Reson.* **192**, 197 (2008).
- ²¹B. Inglis, K. Buckenmaier, P. Sangiorgio, A. F. Pedersen, M. A. Nichols, and J. Clarke, *Proc. Natl. Acad. Sci. U. S. A.* **110**, 19194 (2013).
- ²²V. S. Zotev, T. Owens, A. N. Matlashov, I. M. Savukov, J. J. Gomez, and M. A. Espy, *J. Magn. Reson.* **207**, 78 (2010).
- ²³S. Karpuk, F. Allmendinger, M. Burghoff, C. Gemmel, M. Güldner, W. Heil, W. Kilian, S. Knappe-Grüneberg, C. Mrozik, W. Müller, E. W. Otten, M. Repetto, Z. Salhi, U. Schmidt, A. Schnabel, F. Seifert, Y. Sobolev, L. Trahms, and K. Tullney, *Phys. Part. Nucl.* **44**, 904 (2013).
- ²⁴R. Borowiak, N. Schwaderlapp, F. Hueth, T. Lickert, E. Fischer, S. Bär, J. Hennig, D. Von Elverfeldt, and J. B. Hövener, *Magn. Reson. Mater. Phys., Biol. Med.* **26**, 491 (2013).
- ²⁵J. B. Hövener, N. Schwaderlapp, T. Lickert, S. B. Duckett, R. E. Mewis, L. A. R. Highton, S. M. Kenny, G. G. R. Green, D. Leibfritz, J. G. Korvink, J. Hennig, and D. Von Elverfeldt, *Nat. Commun.* **4**, 2946 (2013).
- ²⁶M. C. Butler, G. Kervern, T. Theis, M. P. Ledbetter, P. J. Ganssle, J. W. Blanchard, D. Budker, and A. Pines, *J. Chem. Phys.* **138**, 234201 (2013).
- ²⁷K. Buckenmaier, M. Rudolph, C. Back, T. Miszta, U. Bommerich, P. Fehling, D. Koelle, R. Kleiner, H. A. Mayer, K. Scheffler, J. Bernarding, and M. Plaumann, *Sci. Rep.* **7**, 13431 (2017).
- ²⁸D. E. J. Waddington, M. Sarracanie, N. Salameh, F. Herisson, C. Ayata, and M. S. Rosen, *NMR Biomed.* **31**, e3896 (2018).
- ²⁹R. W. Adams, J. A. Aguilar, K. D. Atkinson, M. J. Cowley, P. I. P. Elliott, S. B. Duckett, G. G. R. Green, I. G. Khazal, J. Lopez-Serrano, and D. C. Williamson, *Science* **323**, 1708 (2009).
- ³⁰J. Hövener, A. N. Pravdivtsev, B. Kidd, C. R. Bowers, S. Glöggler, K. V. Kovtunov, M. Plaumann, R. Katz-Brull, K. Buckenmaier, A. Jerschow, F. Reiner, T. Theis, R. V. Shchepin, S. Wagner, N. M. M. Zacharias, P. Bhattacharya, and E. Y. Chekmenev, *Angew. Chem., Int. Ed.* **57**, 11140 (2018).
- ³¹C. Elliott, V. Vijayakumar, W. Zink, and R. Hansen, *J. Lab. Autom.* **12**, 17 (2007).
- ³²See www.magnicon.de for Magnicon GmbH, Magnicon Single-Stage Current Sensors (2013).
- ³³See www.magnicon.de for Magnicon GmbH, High Perform, Dc SQUID Electron, XXF-1 Man. v3.3.11 (2013).
- ³⁴See www.vacuumschmelze.com for VACUUMSCHMELZE GmbH & Co.KG.
- ³⁵G. Gottardi, P. Mesirca, C. Agostini, D. Remondin, and F. Bersani, *Bioelectromagnetics* **24**, 125 (2003).
- ³⁶J. Jin, *Electromagnetic Analysis and Design in Magnetic Resonance Imaging* (CRC Press, 1998).
- ³⁷Q. Herreros, H. Dyvorne, P. Campiglio, G. Jasmin-Lebras, A. Demonti, M. Pannetier-Lecoec, and C. Fermon, *Rev. Sci. Instrum.* **84**, 095116 (2013).
- ³⁸I. C. Ruset, L. L. Tsai, R. W. Mair, S. Patz, M. I. Hrovat, M. S. Rosen, I. Muradian, J. Ng, G. P. Topulos, J. P. Butler, R. L. Walsworth, and F. W. Hersman, *Concepts Magn. Reson., Part B* **29**, 210 (2006).
- ³⁹H. J. Sandin, P. L. Volegov, M. A. Espy, A. N. Matlashov, I. M. Savukov, and L. J. Schultz, *IEEE Trans. Appl. Supercond.* **21**, 489 (2011).
- ⁴⁰J. S. Robert Mayrhofer and R. Körber, *IEEE Trans. Appl. Supercond.* **27**, 770043 (2017).
- ⁴¹See www.ni.com for National Instruments Germany GmbH, Germany.
- ⁴²See www.highfinesse.com for HighFinesse, BCS Series.
- ⁴³K. C. J. Zevenhoven and S. Alanko, *J. Phys.: Conf. Ser.* **507**, 042050 (2014).
- ⁴⁴See www.abacus-electronics.de for Abacus-Electronics.
- ⁴⁵See www.toellner.de/en for Toellner.
- ⁴⁶See www.ni.com for Kepco, Germany.
- ⁴⁷See <http://www.drhubert.de> for Dr. Hubert GmbH.
- ⁴⁸See www.frankonia-solutions.com for Frankonia Germany EMC Solutions GmbH.
- ⁴⁹See www.gigavac.com for Gigavac.
- ⁵⁰See www.te.com for TE-Connectivity.
- ⁵¹See www.tesch.de for Tesch-EMC.
- ⁵²I. F. Silvera, *Rev. Mod. Phys.* **52**, 393 (1980).
- ⁵³B. A. Tom, S. Bhasker, Y. Miyamoto, T. Momose, and B. J. McCall, *Rev. Sci. Instrum.* **80**, 016108 (2009).
- ⁵⁴A. M. Juarez, D. Cubric, and G. C. King, *Meas. Sci. Technol.* **13**, N52 (2002).
- ⁵⁵J. B. Hövener, S. Knecht, N. Schwaderlapp, J. Hennig, and D. Von Elverfeldt, *ChemPhysChem* **15**, 2451 (2014).
- ⁵⁶See www.bruker.com/products/mr/nmr/accessories/hyperpolarization/para-hydrogen-generator/overview.html for Bruker Corporation.
- ⁵⁷J. B. Hövener, S. Bär, J. Leupold, K. Jenne, D. Leibfritz, J. Hennig, S. B. Duckett, and D. Von Elverfeldt, *NMR Biomed.* **26**, 124 (2013).
- ⁵⁸See www.cryoton.org for Cryoton.
- ⁵⁹K. C. J. Zevenhoven, H. Dong, R. J. Ilmonemi, and J. Clarke, *Appl. Phys. Lett.* **106**, 034101 (2015).
- ⁶⁰J. Simpson, J. Lane, C. Immer, and R. Youngquist, NASA Technical Reports Server 20010038494, 2001, available at <https://ntrs.nasa.gov/search.jsp?R=20010038494>.
- ⁶¹S. Grosse, F. Gubaydullin, H. Scheelken, H.-M. Vieth, and A. V. Yurkovskaya, *Appl. Magn. Reson.* **17**, 211 (1999).
- ⁶²A. S. Kiryutin, K. L. Ivanov, A. V. Yurkovskaya, R. Kaptein, and H. M. Vieth, *Z. Phys. Chem.* **226**, 1343 (2012).
- ⁶³K. D. Atkinson, M. J. Cowley, P. I. P. Elliott, S. B. Duckett, G. G. R. Green, J. López-Serrano, and A. C. Whitwood, *J. Am. Chem. Soc.* **131**, 13362 (2009).
- ⁶⁴A. N. Pravdivtsev, K. L. Ivanov, A. V. Yurkovskaya, P. A. Petrov, H. H. Limbach, R. Kaptein, and H. M. Vieth, *J. Magn. Reson.* **261**, 73 (2015).
- ⁶⁵R. L. Grubb, M. E. Raichle, J. O. Eichling, and M. M. Ter-Pogossian, *Stroke* **5**, 630 (1974).
- ⁶⁶H. Lu, X. Golay, J. J. Pekar, and P. C. M. Van Zijl, *Magn. Reson. Med.* **50**, 263 (2003).
- ⁶⁷J. J. Chen and G. B. Pike, *NMR Biomed.* **22**, 1054 (2009).
- ⁶⁸H. Eto, F. Hyodo, N. Kosem, R. Kobayashi, K. Yasukawa, M. Nakao, M. Kuniwa, and H. Utsumi, *Free Radicals Biol. Med.* **89**, 1097 (2015).
- ⁶⁹H. Utsumi and F. Hyodo, *Methods Enzymol.* **564**, 553 (2015).
- ⁷⁰S. Ito and F. Hyodo, *Sci. Rep.* **6**, 21407 (2016).
- ⁷¹E. M. Haacke, R. W. Brown, M. R. Thompson, and R. Venkatesan, *Haacke—Magnetic Resonance Imaging—Physical Principles and Sequence Design* (John Wiley and Sons, Inc., 1999).
- ⁷²R. A. Green, R. W. Adams, S. B. Duckett, R. E. Mewis, D. C. Williamson, and G. G. R. Green, *Prog. Nucl. Magn. Reson. Spectrosc.* **67**, 1 (2012).
- ⁷³K. L. Ivanov, A. N. Pravdivtsev, A. V. Yurkovskaya, H. M. Vieth, and R. Kaptein, *Prog. Nucl. Magn. Reson. Spectrosc.* **81**, 1 (2014).
- ⁷⁴A. N. Pravdivtsev, A. V. Yurkovskaya, H. M. Vieth, K. L. Ivanov, and R. Kaptein, *ChemPhysChem* **14**, 3327 (2013).
- ⁷⁵T. Theis, M. L. Truong, A. M. Coffey, R. V. Shchepin, K. W. Waddell, F. Shi, B. M. Goodson, W. S. Warren, and E. Y. Chekmenev, *J. Am. Chem. Soc.* **137**, 1404 (2015).
- ⁷⁶M. L. Truong, T. Theis, A. M. Coffey, R. V. Shchepin, K. W. Waddell, F. Shi, B. M. Goodson, W. S. Warren, and E. Y. Chekmenev, *J. Phys. Chem. C* **119**, 8786 (2015).
- ⁷⁷R. V. Shchepin, D. A. Barskiy, A. M. Coffey, T. Theis, F. Shi, W. S. Warren, B. M. Goodson, and E. Y. Chekmenev, *ACS Sens.* **1**, 640 (2016).

Publication 2

SCIENTIFIC REPORTS

OPEN

SQUID-based detection of ultra-low-field multinuclear NMR of substances hyperpolarized using signal amplification by reversible exchange

K. Buckenmaier¹, M. Rudolph^{1,2}, C. Back², T. Misztal³, U. Bommerich⁴, P. Fehling¹, D. Koelle², R. Kleiner², H. A. Mayer³, K. Scheffler¹, J. Bernarding⁴ & M. Plaumann⁴

Ultra-low-field (ULF) nuclear magnetic resonance (NMR) is a promising spectroscopy method allowing for, e.g., the simultaneous detection of multiple nuclei. To overcome the low signal-to-noise ratio that usually hampers a wider application, we present here an alternative approach to ULF NMR, which makes use of the hyperpolarizing technique signal amplification by reversible exchange (SABRE). In contrast to standard parahydrogen hyperpolarization, SABRE can continuously hyperpolarize ¹H as well as other MR-active nuclei. For simultaneous measurements of ¹H and ¹⁹F under SABRE conditions a superconducting quantum interference device (SQUID)-based NMR detection unit was adapted. We successfully hyperpolarized fluorinated pyridine derivatives with an up to 2000-fold signal enhancement in ¹⁹F. The detected signals may be explained by two alternative reaction mechanisms. SABRE combined with simultaneous SQUID-based broadband multinuclear detection may enable the quantitative analysis of multinuclear processes.

Signal Amplification By Reversible Exchange (SABRE) is a relatively new technique to produce continuous hyperpolarization to boost nuclear magnetic resonance (NMR) signals and is even applied for magnetic resonance imaging (MRI)^{1,2}. SABRE is based on a symmetry-breaking mechanism that converts the parahydrogen (para-H₂) spin order into a non-Boltzmann polarization^{1,3,4}. High-field NMR measurements show signal enhancements of up to a factor of 10⁵ for ¹H. The underlying mechanism is based on the interaction of para-H₂ with a substrate of interest via an Ir-based catalyst system¹.

Gong *et al.* first reported the use of SABRE at low-field in 2010⁵. Further low-field (10–500 mT) examinations for the standard para-H₂ induced polarization (PHIP) approach, where hydrogen atoms were added to a double or triple bond^{6,7}, were done by Hamans *et al.*⁸ and Theis *et al.*^{9,10}. In general, the advantage of SABRE against standard-PHIP is the possibility that the enhanced substrates can be continuously re-hyperpolarized by supplying a steady flow of parahydrogen^{11,12}. It is important to note that most heteronuclei require special pulse sequences, or one has to lower the field strength to perform an efficient polarization transfer. Thus, for high-field MR, dedicated solutions have been developed such as SABRE-SHEATH¹³ or mechanically challenging shuttle mechanisms¹⁴. Most of the experiments have focused on the detection of hyperpolarized molecules in high magnetic fields, on increasing the number of hyperpolarized substrates^{15,16}, or on measuring extracts of biofluids where spin densities down to sub- μ M concentrations could have been detected¹⁷. The mechanism relies on transforming the spin order of the para-H₂ singlet state into nuclear spin polarization of Ir hydride protons when an exchange reaction is performed in a low magnetic field^{1,18,19}. The required field strength (2–10 mT) of the polarization transfer reaction to further spin- $\frac{1}{2}$ nuclei of the substrate such as pyridine is strongly dependent on the coupling

¹High-Field Magnetic Resonance Center, Max Planck Institute for Biological Cybernetics, Spemannstr. 41, 72076, Tübingen, Germany. ²Physikalisches Institut und Center for Quantum Science (CQ) in LISA+, University of Tübingen, Tübingen, Germany. ³Institute of Inorganic Chemistry, University of Tübingen, Tübingen, Germany. ⁴Department for Biometrics and Medical Informatics, Otto-von-Guericke University, Magdeburg, Germany. Correspondence and requests for materials should be addressed to K.B. (email: kai.buckenmaier@tuebingen.mpg.de)

constants^{1,20,21}. So far the theoretical background of SABRE is based on level anti-crossings between magnetic field independent J-coupling energy levels and the magnetic field dependent chemical shift^{11,22,23}.

Low-field and ultra-low-field (ULF, <10 mT) NMR provide an optimal and in comparison to high-field NMR less costly tool for investigating the polarization transfer mechanism. Even MR imaging can be realized at ultra-low fields^{24–32}. More important, certain experiments that require complex and expensive technical efforts at high fields can be easily realized at ultra-low fields, such as the simultaneous detection of several nuclei³³, the separation of detection field and polarizing field, or the variation of the polarizing field. However, a wider use of ULF NMR is still hampered by the inherent low signal-to-noise ratio (SNR), as the thermal equilibrium magnetization is increasing with the polarizing field, which is typically in the range of several mT as compared to high-field NMR with up to 23.5 T. Additionally, ULF NMR signals are in the range of some kHz (about 2 kHz at the earth's magnetic field), which renders the signal in detection coils too low.

A combined strategy provides a solution to increase the SNR dramatically: first, detection is realized by a superconducting interference device (SQUID) that is very sensitive and can detect magnetic field down to some fT; second, the signal is enhanced by using the hyperpolarization technique SABRE.

ULF NMR provides the advantage that the polarizing field $B_p > B_0$, where B_0 is the detection field of the NMR signal, can be easily and reproducibly adapted to the individual field strengths required for the optimum polarization transfer of specific substances³⁴. The B_p field is usually realized by electromagnetic coils which allow field changes within milliseconds. Also imaging in the vicinity of metals is possible without distortion artefacts³⁵. The sensitivity of different magnetic field detectors used for ULF MRI^{36,37}, such as for example atomic magnetometers, is comparable to the already widely used SQUIDs. A SQUID-based system has not only a higher signal to noise ratio (SNR) compared to a system using a Faraday coil at ULF³⁸, but also can detect the NMR signal of multiple nuclei simultaneously. SQUIDs are broadband detectors, which are able to detect the magnetic flux directly, rather than the change of the magnetic field, making them sensitive from DC up to the GHz range³⁹.

Another advantage is that the NMR signal can be detected via a second order superconducting gradiometer, which acts as a surface coil³⁹. The open geometry and the small field strengths needed for detecting the NMR signal makes a SQUID based system combinable with imaging techniques such as magnetoencephalography (MEG)^{40,41}, where SQUIDs can be used to detect the MEG and NMR signals.

The design of our home-built ULF MRI system is derived from previously described detection architectures^{33,41,42}. It consists of a tetracoil⁴³ with radius 260 mm for generating the B_0 field along the z axis, a B_1 coil in a Helmholtz configuration with radius 145 mm oriented perpendicular to B_0 in the y direction, a prepolarizing B_p Helmholtz coil with radius of 90 mm oriented along the x axis, and a gradient coil in a Maxwell configuration with radius 306 mm for shimming along the z axis. All coils are driven by commercially available current amplifiers (Hubert A110-16-QE, Kepco BOP 100-4 ML, Highfinesse BCS 3/12). The DC current sources are heavily filtered with pi-filters. The amplifiers for the B_1 and B_p coil were galvanically separated from the whole setup during the readout of the signal via mechanical relays. The heart of the system, the SQUID-based magnetic field detector, is sitting inside a liquid-helium filled low-noise fiber glass Dewar [see Fig. 1(a) and (b)]^{44,45}. The SQUID itself sits inside a Niobium shield preventing background noise to couple directly into the SQUID [see Fig. 1(c)]. A pickup coil in a second-order gradiometer configuration, with a loop diameter of 40 mm and a baseline of 40 mm, is used to couple the NMR signal to the SQUID via an input coil. The gradiometer is sensitive to the sample, which locates 12 mm (the hot-to-cold distance of the Dewar) below the lowest loop, and it rejects signals from distant noise sources, because such sources usually exhibit only a small gradient. In series with the gradiometer and input coil, a current-limiting array of SQUIDs (Q-spoiler) with a critical current I_c acts as a superconducting short, as long as the induced current in the gradiometer is less than I_c . Above I_c the junctions become dissipative, limiting the maximum current induced in the gradiometer and protecting the SQUID. Large currents are, for example, induced by the pulsed magnetic fields needed in ULF MRI.

Since SQUIDs are sensitive to signals from DC up to the GHz range, the whole system is placed inside a cylindrical mu-metal shield with a diameter of 780 mm for magnetic shielding and inside a cubic steel-shielding chamber with an edge length of 2.8 m for shielding RF noise.

To allow for continuous hyperpolarization, a cylindrical/spherical PEEK vessel with 2 ml volume serving as reaction chamber was adapted. The para- H_2 was continuously delivered at the bottom of the vessel and bubbled continuously through the sample. At the top part, a small hole permitted the para- H_2 outflow. Since the evaporation rate of the substrate dramatically increases with the flow rate of the para- H_2 and capillary action in combination with overpressure due to the para- H_2 removes liquid from the vessel, a reservoir behind the hole in the top part was installed together with a backflow tube. The backflow tube feeds the liquid from the reservoir back to the bottom of the reaction chamber. A typical measurement session required about 2 to 3 hours. At a para- H_2 flow rate of approx. 1.5 l/h, roughly 3–4 ml of the substrate evaporated. By filling the reservoir with additional 5 ml we were able to measure during the whole session without refilling. The temperature of the sample stayed constantly at room temperature during the whole measurement. The para- H_2 was produced on-site during the experiment with a home-made para- H_2 generator operating at about 21 K–30 K. The design of the generator is based on ref. ⁴⁶. The concentration of para- H_2 (in comparison to orthohydrogen) was determined before the experiments by using a home-made temperature-stabilized thermal-conductivity cell based on a heated tungsten filament^{47–50}. With this method a quantitative analysis of the para- H_2 concentration is difficult, however qualitatively we could see that the concentration was much higher than the equilibrium concentration at liquid nitrogen temperature (77 K).

A simple free-induction-decay (FID) pulse sequence served for acquiring the NMR signal and is shown in Fig. 1(d). A prepolarizing pulse with variable amplitude B_p and variable length t_{B_p} was used to increase the B_0 field strength. After the adiabatic switch-off of the B_p field the sample magnetization is aligned with B_0 and a $90^\circ B_1$ pulse followed. A double resonant pulse, for example, a B_1 pulse exhibiting in its Fourier transform two peaks at the Larmor frequencies of nucleus X and Y, can be used to excite the magnetization of multiple nuclei simultaneously. In this study we used single resonant pulses with one exception in the SI (see spectrum in Figure S1). Subsequently, the FID was read out.

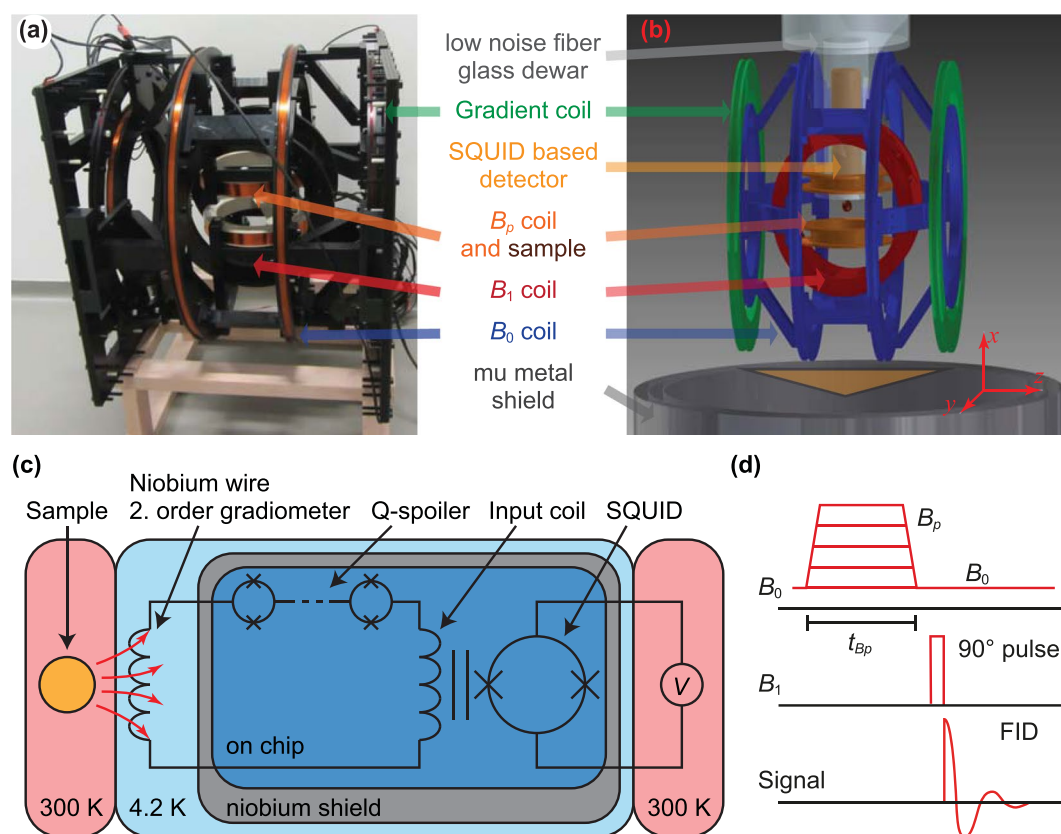


Figure 1. Photo (a), scheme of the ULF MRI system (b), scheme of the SQUID based magnetic field detector (c) and the pulse sequence used for the ULF NMR measurements (d).

As model compounds 3,5-bis(trifluoromethyl)pyridine, ethyl-5-fluoronicotinic acid and 3-fluoropyridine were chosen to compare the hyperpolarizability of ^1H and ^{19}F quantitatively under ULF conditions. All measurements were performed in presence of an Ir catalyst $[\text{Ir}(\text{COD})(\text{IMes})(\text{Cl})]^{51}$. Substrates as well as the catalyst were dissolved in methanol and injected at room temperature into the reaction chamber before starting the first measurement. The exact mixture of the three substances was 7 mg of $[\text{Ir}(\text{COD})(\text{IMes})(\text{Cl})]$ and 0.23 mmol of the fluorinated pyridine derivative, dissolved in 10 ml methanol. The samples were not degassed.

The detection field B_0 was $\sim 150 \mu\text{T}$ (about three times stronger than the earth's magnetic field). Accordingly, the Larmor frequencies of the hyperpolarized nuclei were $\sim 6140 \text{ Hz}$ for ^1H and $\sim 5770 \text{ Hz}$ for ^{19}F (see peak positions in SI Figure S1). The field strength of $\sim 150 \mu\text{T}$ was chosen, because the noise spectrum around 6 kHz did not show any additional noise due to external noise sources. Test experiments on solutions of the compounds and catalyst in methanol but without para- H_2 show small MR signals of the methanol, which increases linearly with B_p . Since this signal is much smaller than the hyperpolarized signal of the substrate, no deuterated methanol was used.

To determine the influence of the polarizing field B_p on the achievable signal enhancements experiments were performed using the sequence shown in Fig. 1d. The B_p field strength was varied between 0.144 mT (the B_0 field) and 10.3 mT. The acquired signal was Fourier transformed, and the absolute value of the signal was integrated over the range of the multiple peak structure ($\approx 20 \text{ Hz}$ around the excitation frequency). The results show (Fig. 2) that the signal enhancement is not only influenced by the polarizing field, but also by the substance to be hyperpolarized and the corresponding nuclei. Interestingly, the ^{19}F signals of the monofluorinated compounds exhibit only a weak dependence on the polarizing field when compared to the according ^1H signals. The field strengths that yield maximum signal enhancement for the ^{19}F and the ^1H signal of the substances were also different. The B_p field for the maximum ^{19}F signal enhancement is lower for the two monofluorinated pyridine derivatives lower than for ^1H . 3,5-Bis(trifluoromethyl)pyridine seems to exhibit a different behavior. Here, the B_p field dependency of the ^{19}F is even less pronounced than for all the other substrates. The small increase of the area-under-peak for stronger B_p field strengths is due to an increase in noise, which becomes dominant here, because of the small SNR.

A more detailed investigation can be made by plotting the spectra (real part of the MR signal) as a function of the B_p field. Due to J-coupling, multiple peaks can be observed. For 3-fluoropyridine and 3,5-bis(trifluoromethyl)pyridine the signal amplitudes of all resonances are correlated. The same could be observed for the ^1H signal of ethyl-5-fluoronicotinic acid. An exception is observed for the ^{19}F signal of ethyl-5-fluoronicotinic acid (see Fig. 3): the peak intensity below 5771 Hz and between 5773 Hz and 5776 Hz seems to be correlated. However, the peak at 5772 Hz (between dashed lines) and at 5778 Hz (between dotted lines) is changing its phase for increasing B_p . The sequence parameters are listed in Table 1, measurement number 1 to 6.

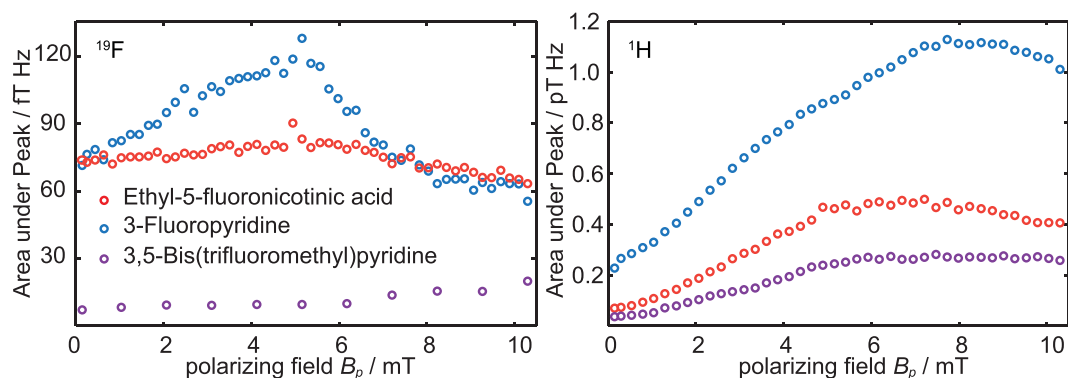


Figure 2. Integrated peak signals vs. B_p amplitude for the ^{19}F (left) and ^1H (right) signals of all three substances.

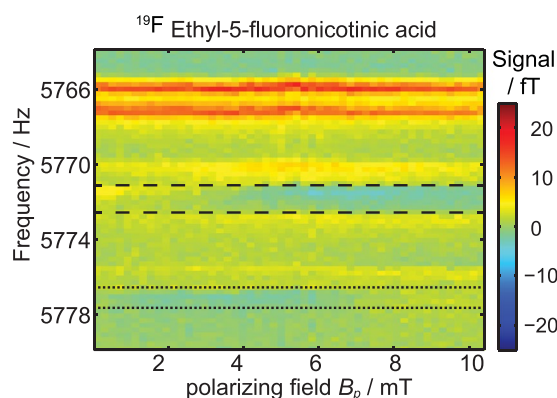


Figure 3. ^{19}F spectra of ethyl-5-fluoronicotinic acid as a function of B_p . The signal intensity is given in fT. For $B_p < 1$ mT all visible NMR peaks are positive. With increasing B_p the peaks between, respectively, the dashed and the dotted lines become negative.

The measurements support previous results that the polarization transfer from ^1H to further spin-1/2 nuclei is field-dependent even at ultra-low fields^{52,53}. In the next set of experiments we investigated the signal enhancement of ^1H and ^{19}F and the magnetization transfer between both nuclei when applying the SABRE technique. It was observed that a strong magnetization transfer reaction to ^1H and ^{19}F nuclei takes place in the range of 0–10 mT. However, while the transfer to ^1H nuclei of pyridine derivatives was strongly field-dependent, the field dependence for ^{19}F hyperpolarization is much less pronounced (see Fig. 2). To the best of our knowledge, this is the first time that such behavior could be detected.

As a next characterization step, the signal enhancement as a function of the hyperpolarization time t_{BP} was determined in order to gain the maximum SNR for multiple averages. The experimental setup was identical to the previous measurements; however, instead of sweeping B_p , now t_{BP} was varied between 100 ms and 10.1 s. The polarizing field B_p was fixed to the value where the maximum enhancement was observed (Fig. 4). The corresponding experimental parameters are listed in Table 1, rows 7 to 12.

An exponential saturation function

$$M(t_{BP}) = M_{HP} \left(1 - \exp\left(-\frac{t_{BP} - t_0}{T_{HP}}\right) \right) \quad (1)$$

was fitted to the data (see green lines in Fig. 4). Here, $M(t_{BP})$ is the magnetization of the sample, which is proportional to the area under the peak. M_{HP} is the saturation magnetization for infinite polarizing time, t_0 is a time offset and T_{HP} is the buildup time of the magnetization. The buildup time T_{HP} depends also on the longitudinal relaxation time T_1 , which is dependent on the B_p field strength, as well as on the buildup time constant for the hyperpolarization of the substrate. T_{HP} is dominated by the shorter of both processes. The fitted values for T_{HP} of the ^{19}F and ^1H signals of the three substrates are listed in Table 2.

The results show that T_{HP} can be different for the observed nuclei. Whereas for 3-fluoropyridine, T_{HP} for ^{19}F and ^1H is within the confidence interval and has in comparison to the other two substrates a very long T_{HP} , the other two substances show a different behavior. T_{HP} for ^1H of ethyl-5-fluoronicotinic acid is about 1 s shorter than for ^{19}F , also within the confidence interval. The influence of the substituent ($-\text{COOCH}_2\text{CH}_3$) in ethyl-5-fluoronicotinic acid is even stronger and the T_{HP} time for ^{19}F of 3,5-bis(trifluoromethyl)pyridine was too short and could not be fitted (see Fig. 4). As can be seen in Fig. 2 (purple dots) the hyperpolarization process

#	Substance	Avg.	TR[s]	B_p time[s]	B_p field[mT]	B_1 Freq.[Hz]	Nucleus
1	Ethyl-5-fluoronicotinic acid	5	6.5	2	0.144–10.3	5775	^{19}F
2	3-Fluoropyridine	5	6.5	2	0.144–10.3	5775	^{19}F
3	3,5-Bis(trifluoromethyl)pyridine	50	3.5	2	0.144–10.3	5775	^{19}F
4	Ethyl-5-fluoronicotinic acid	5	8.5	4	0.144–10.3	6140	^1H
5	3-Fluoropyridine	5	8.5	4	0.144–10.3	6140	^1H
6	3,5-Bis(trifluoromethyl)pyridine	5	8.5	4	0.144–10.3	6140	^1H
7	Ethyl-5-fluoronicotinic acid	10	1.6–10.6	0–10	3.1	5775	^{19}F
8	3-Fluoropyridine	10	1.6–10.6	0–10	5.2	5775	^{19}F
9	3,5-Bis(trifluoromethyl)pyridine	25	1.5–10.5	1.5–10.5	0.14	5775	^{19}F
10	Ethyl-5-fluoronicotinic acid	10	1.6–10.6	0–10	6.2	6140	^1H
11	3-Fluoropyridine	10	1.6–10.6	0–10	7.7	6140	^1H
12	3,5-Bis(trifluoromethyl)pyridine	10	1.6–10.6	0–10	7.7	6140	^1H
13	Ethyl-5-fluoronicotinic acid	50	9.5	9.5	0.144	5775	^{19}F
14	3-Fluoropyridine	50	9.5	4	5.2	5775	^{19}F
15	3,5-Bis(trifluoromethyl)pyridine	200	5.25	5.25	0.144	5775	^{19}F
16	Ethyl-5-fluoronicotinic acid	50	9.5	4	6.2	6140	^1H
17	3-Fluoropyridine	50	9.5	4	7.7	6140	^1H
18	3,5-Bis(trifluoromethyl)pyridine	100	10.1	5	7.7	6140	^1H

Table 1. Overview of the sequence parameters used for all presented ultra-low-field measurements.

Sample	Nucleus	T_{HP} / s
Ethyl-5-fluoronicotinic acid	^{19}F	2.4 ± 0.5
3-Fluoropyridine	^{19}F	9.4 ± 3.9
3,5-Bis(trifluoromethyl)pyridine	^{19}F	—
Ethyl-5-fluoronicotinic acid	^1H	3.4 ± 0.5
3-Fluoropyridine	^1H	9.7 ± 2.4
3,5-Bis(trifluoromethyl)pyridine	^1H	3.9 ± 1.0

Table 2. ^1H and ^{19}F ultra-low-field build up times for ethyl-5-fluoronicotinic acid, 3-fluoropyridine and 3,5-bis(trifluoromethyl)pyridine.

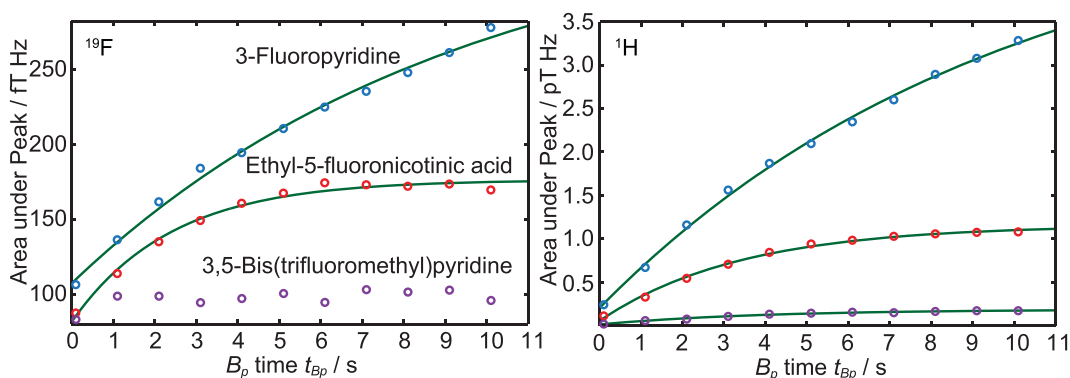


Figure 4. Integrated peak signals vs. pulse length t_{Bp} for the ^{19}F (left) and ^1H (right) MR signals of 3-fluoropyridine, ethyl-5-fluoronicotinic acid and 3,5-bis(trifluoromethyl)pyridine.

for ^{19}F is independent from the field strength. For the sequence shown in Fig. 1d the hyperpolarization process starts during the data acquisition time of the previous shot directly after the 90° pulse resulting in a minimum hyperpolarization time of the data acquisition time. For short T_{HP} the signal is already saturated. Therefore, a fit using Equation (1) will not lead to reasonable results. For the other substances, even though the hyperpolarization processes start also at the same position, they are not saturated for short t_{Bp} . Therefore, by varying t_{Bp} , Equation (1) leads to reasonable results.

In order to get more information on the hyperpolarization process, hyperpolarized high-resolution ULF spectra were additionally acquired using the simple FID sequence. The sequence parameters were set to the B_p amplitude for maximal enhancement, and t_{Bp} was roughly estimated to get the highest SNR for multiple averages. The

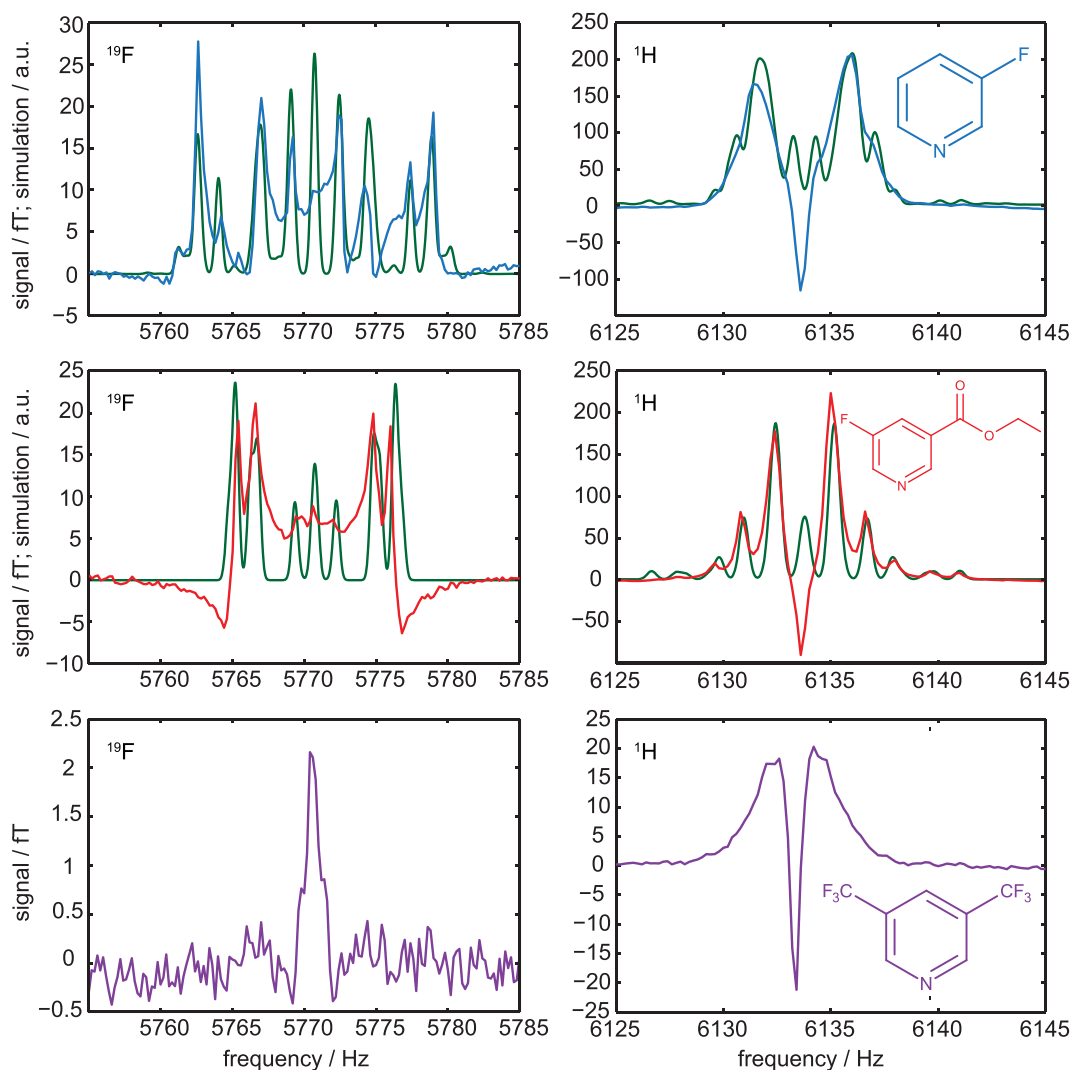


Figure 5. Ultra-low-field ^{19}F and ^1H MR spectra of hyperpolarized 3-fluoropyridine (upper row), ethyl-5-fluoronicotinic acid (middle row), and 3,5-bis(trifluoromethyl)pyridine (lower row). Substances and catalysts were dissolved in methanol and measured at 144 μT . Signals around 5770 Hz can be assigned to the ^{19}F nuclei showing the ^1H - ^{19}F coupling. Signals around 6134 Hz can be assigned to the ^1H signal. The blue, red and violet lines represent the measured spectra whereas the green lines represent simulated spectra based on high-field determined coupling constants.

sequence parameters are listed in Table 1 (rows 13 to 18). A detailed analysis of the ^1H and ^{19}F frequency regions in the ULF spectra show J-coupling resolved multiple resonances for the first two hyperpolarized substrates. For 3,5-bis(trifluoromethyl)pyridine only two singlets were observable (see Fig. 5).

To differentiate the hyperpolarization effects from the standard spectra, which were obtained at thermal equilibrium, simulations of NMR spectra without hyperpolarized signals were performed both at high and ultra-low fields using Bruker Topspin software (high-field) as well as VeSPA (low-field)⁵⁴. The coupling constants were determined using thermal ^1H and ^{19}F spectra acquired at high-field (7 T) of all three non-hyperpolarized substrates dissolved in methanol- d_4 (see supplementary material). Interestingly, the thermal simulations fit well even to the quite complex ULF hyperpolarized spectra (Fig. 5, green lines) except for a central resonance with large amplitude in the ^1H spectrum. This line shows most likely hyperpolarized methanol. The ^{19}F signal in the spectrum displays the ^1H - ^{19}F couplings, while ^1H - ^1H as well as ^1H - ^{19}F couplings dominate the ^1H spectrum. For 3,5-bis(trifluoromethyl)pyridine no J-couplings were detected. It may therefore be hypothesized that the effect of hyperpolarization significantly increases the signal at ULF but alters relatively little the overall spectral characteristics, except for the ratio of the amplitudes of several spectral lines. An analysis of the methanol resonance line in the ^1H data supports the conclusion that the central line in the ^1H spectral range is due to hyperpolarized methanol. This signal is also visible in the ^1H ULF spectrum of 3,5-bis(trifluoromethyl)pyridine. However, as no J-couplings were detectable at high-field simulations, no simulations were performed for this substance. The broad ^1H signal around the narrow central peak may be due to ^1H resonances with shortened T_2 -time.

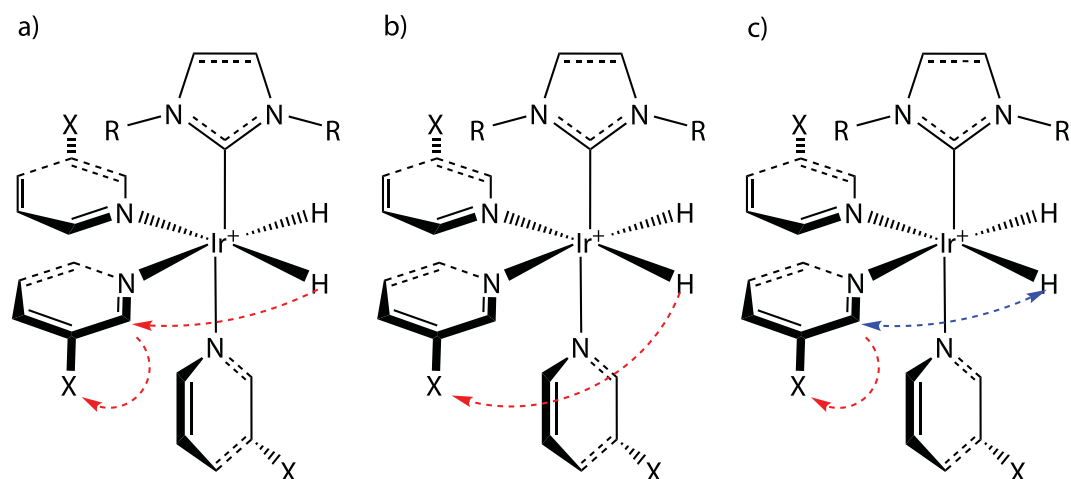


Figure 6. Possible polarization transfer mechanisms to spin-1/2 heteronuclei of pyridine derivatives. **(a)** Indirect polarization transfer: the polarization of hydrogen is transferred to hydrogen of the pyridine derivative and subsequently to the corresponding heteronucleus X, e.g. ^{19}F . **(b)** Direct polarization transfer: the polarization is transferred directly to the corresponding heteronucleus X of the exchangeable ligand. **(c)** Polarization transfer after H/H exchange reaction. Hydrogens of a pyridine ligand in ortho-position can exchange during SABRE reaction⁵⁶ which would also enable a direct polarization transfer from polarized hydrogen atoms (to the corresponding heteronucleus of the exchangeable ligand X (here ^{19}F)).

These encouraging results show that SABRE in combination with SQUID-based ULF NMR is well suited to increase the low SNR significantly and allow to measure otherwise non-detectable multinuclear spectra.

Aside from allowing measuring samples with low spin densities or nuclei with low sensitivity, the use of SABRE as a hyperpolarization technique enables a steady state generation of hyperpolarization. Compared to standard PHIP, SABRE allows repeating the experiment multiple times thus additionally increasing the SNR.

Our measurements also demonstrate that the theory behind SABRE is not yet completely understood^{11,22,23,52}. J-coupling as the main mechanism for the polarization transfer cannot explain the differences of the B_p field dependencies between the ^{19}F and ^1H signals of all three substrates. One would expect that the polarization is first transferred to a proton of the substrate and subsequently transferred to ^{19}F (see Fig. 6a). But then the B_p dependencies of the ^{19}F and ^1H signal should be correlated, which is not the case. It seems that other coupling mechanisms such as dipole-dipole coupling cannot be neglected, since the polarization transfer takes place in the vicinity of the catalyst. Therefore, the secular part of the intramolecular dipole-dipole coupling does not average to zero, as it is the case in isotropic liquids⁵⁵. Thus, a direct polarization transfer reaction from ^1H to ^{19}F might become possible (see Fig. 6b).

A further explanation of the observed results is based on a proton-proton exchange reaction (see Fig. 6c). It was reported that the ortho-standing hydrogen nuclei can exchange via the Ir-catalyst with Ir-coordinated hydrogen (here from parahydrogen)⁵⁶. This supports the conclusion that at least one hydrogen atom from parahydrogen was transferred to the fluorinated pyridine derivative and followed by an intramolecular polarization transfer to the vicinal bounded fluorine. A complete simulation of the hyperpolarized spectra may therefore have to include additional processes.

The presented results demonstrate that a SQUID-based NMR system is a promising setup for the investigation of hyperpolarization techniques that work optimally in the μT and mT range and below, such as SABRE or dynamic nuclear polarization. As described by Appelt *et al.*, low-field MR detection can be used for the determination of relaxation times, diffusion and J-coupling constants⁵⁷. Our results also support the hypothesis of alternative reaction pathways in SABRE that are based on an H/H exchange^{56,58}. Furthermore, SQUID-based systems can be used for magnetic resonance imaging and the simultaneous detection of different MR-active nuclei. Combining continuous hyperpolarization methods with SQUIDs increases the sensitivity to a point where spatially-resolved MR methods or even MR imaging of heteronuclei of background-free molecular probes at ultra-low-field conditions will be feasible.

The datasets generated and/or analyzed during the current study are available from the corresponding author on reasonable request.

References

- Adams, R. W. *et al.* Reversible interactions with para-hydrogen enhance NMR sensitivity by polarization transfer. *Science* **323**, 1708–1711 (2009).
- Rovedo, P. *et al.* Molecular MRI in the earth's magnetic field using continuous hyperpolarization of a biomolecule in water. *The journal of physical chemistry. B* **20**, 5670–5677 (2016).
- Ivanov, K. L., Pravdivtsev, A. N., Yurkovskaya, A. V., Vieth, H.-M. & Kaptein, R. The role of level anti-crossings in nuclear spin hyperpolarization. *Progress in Nuclear Magnetic Resonance Spectroscopy* **81**, 1–36 (2014).
- Kiryutin, A. S., Ivanov, K. L., Yurkovskaya, A. V., Kaptein, R. & Vieth, H.-M. Transfer of parahydrogen induced polarization in scalar coupled systems at variable magnetic field. *Zeitschrift für Physikalische Chemie* **226**, 1343–1362 (2012).

5. Gong, Q., Gordji-Nejad, A., Blumich, B. & Appelt, S. Trace analysis by low-field NMR: breaking the sensitivity limit. *Analytical Chemistry* **82**, 7078–7082 (2010).
6. Eisenschmid, T. C. *et al.* Para hydrogen induced polarization in hydrogenation reactions. *J. Am. Chem. Soc.* **109**, 8089–8091 (1987).
7. Natterer, J. & Bargon, J. Parahydrogen induced polarization. *Progress in Nuclear Magnetic Resonance Spectroscopy* **31**, 293–315 (1997).
8. Hamans, B. C., Andreychenko, A., Heerschap, A., Wijmenga, S. & Tessari, M. NMR at earth's magnetic field using para-hydrogen induced polarization. *Journal of Magnetic Resonance* **212**, 224–228 (2011).
9. Theis, T. *et al.* Zero-field NMR enhanced by parahydrogen in reversible exchange. *J. Am. Chem. Soc.* **134**, 3987–3990 (2012).
10. Theis, T. *et al.* Parahydrogen-enhanced zero-field nuclear magnetic resonance. *Nature Physics* **7**, 571–575 (2011).
11. Hövener, J.-B., Knecht, S., Schwaderlapp, N., Hennig, J. & Elverfeldt, D. von. Continuous re-hyperpolarization of nuclear spins using parahydrogen: Theory and experiment. *ChemPhysChem* **15**, 2451–2457 (2014).
12. Pravdivtsev, A. N., Yurkovskaya, A. V., Vieth, H.-M. & Ivanov, K. L. RF-SABRE: A way to continuous spin hyperpolarization at high magnetic fields. *The journal of physical chemistry B* **119**, 13619–13629 (2015).
13. Truong, M. L. *et al.* ¹⁵N hyperpolarization by reversible exchange using SABRE-SHEATH. *The journal of physical chemistry C* **119**, 8786–8797 (2015).
14. Kiryutin, A. S. *et al.* A fast field-cycling device for high-resolution NMR: Design and application to spin relaxation and hyperpolarization experiments. *Journal of magnetic resonance (San Diego, Calif.: 1997)* **263**, 79–91 (2016).
15. Glöggler, S. *et al.* Para-hydrogen induced polarization of amino acids, peptides and deuterium-hydrogen gas // Para-hydrogen induced polarization of amino acids, peptides and deuterium-hydrogen gas. *Phys. Chem. Chem. Phys.* **13**, 13759–13764 (2011).
16. Zeng, H. *et al.* Optimization of SABRE for polarization of the tuberculosis drugs pyrazinamide and isoniazid. *Journal of Magnetic Resonance* **237**, 73–78 (2013).
17. Reile, I. *et al.* NMR detection in biofluid extracts at sub- μ M concentrations via para-H₂ induced hyperpolarization. *The Analyst* **141**, 4001–4005 (2016).
18. Atkinson, K. D. *et al.* Spontaneous transfer of para hydrogen derived spin order to pyridine at low magnetic field. *J. Am. Chem. Soc.* **131**, 13362–13368 (2009).
19. Green, R. A. *et al.* The theory and practice of hyperpolarization in magnetic resonance using parahydrogen. *Progress in Nuclear Magnetic Resonance Spectroscopy* **67**, 1–48 (2012).
20. Dücker, E. B., Kuhn, L. T., Münnemann, K. & Griesinger, C. Similarity of SABRE field dependence in chemically different substrates. *Journal of Magnetic Resonance* **214**, 159–165 (2012).
21. Plaumann, M. *et al.* Hyperpolarization of fluorinated pyridine carboxylic acids. *MAGMA: (ESMRMB)* (2016).
22. Buljubasich, L., Franzoni, M. B., Spiess, H. W. & Münnemann, K. Level anti-crossings in parahydrogen induced polarization experiments with Cs-symmetric molecules. *Journal of magnetic resonance (San Diego, Calif.: 1997)* **219**, 33–40 (2012).
23. Pravdivtsev, A. N., Yurkovskaya, A. V., Vieth, H.-M., Ivanov, K. L. & Kaptein, R. Level anti-crossings are a key factor for understanding para-hydrogen-induced hyperpolarization in SABRE experiments. *ChemPhysChem* **14**, 3327–3331 (2013).
24. Seton, H. C., Hutchison, J. M. S. & Bussell, D. M. A 4.2 K receiver coil and SQUID amplifier used to improve the SNR of low-field magnetic resonance images of the human arm. *Meas. Sci. Technol.* **8**, 198–207 (1997).
25. Seton, H. C., Hutchison, J. M. S. & Bussell, D. M. Gradiometer pick-up coil design for a low field SQUID-MRI system. *MAGMA* **8**, 116–120 (1999).
26. Seton, H. C., Bussell, D. M., Hutchison, J. & Lurie, D. J. Use of a DC SQUID receiver preamplifier in a low field MRI system. *IEEE Trans. Appl. Supercond.* **5**, 3218–3221 (1995).
27. McDermott, R. *et al.* Liquid-state NMR and scalar couplings in microtesla magnetic fields. *Science (New York, N.Y.)* **295**, 2247–2249 (2002).
28. Bernarding, J. *et al.* J-coupling nuclear magnetic resonance spectroscopy of liquids in nT fields. *Journal of the American Chemical Society* **128**, 714–715 (2006).
29. Hilschenz, I. *et al.* Magnetic resonance imaging at frequencies below 1 kHz. *Magnetic Resonance Imaging* **31**, 171–177 (2013).
30. Coffey, A. M., Truong, M. L. & Chekmenev, E. Y. Low-field MRI can be more sensitive than high-field MRI. *Journal of Magnetic Resonance* **237**, 169–174 (2013).
31. Inglis, B. *et al.* MRI of the human brain at 130 microtesla. *Proceedings of the National Academy of Sciences of the United States of America* **110**, 19194–19201 (2013).
32. Körber, R. *et al.* SQUIDS in biomagnetism. A roadmap towards improved healthcare. *Supercond. Sci. Technol.* **29**, 113001 (2016).
33. Zotev, V. S. *et al.* Microtesla MRI with dynamic nuclear polarization. *Journal of magnetic resonance (San Diego, Calif.: 1997)* **207**, 78–88 (2010).
34. Borowiak, R. *et al.* A battery-driven, low-field NMR unit for thermally and hyperpolarized samples. *Magma (New York, N.Y.)* **26**, 491–499 (2013).
35. Mößle, M. *et al.* SQUID-detected microtesla MRI in the presence of metal. *Journal of magnetic resonance (San Diego, Calif.: 1997)* **179**, 146–151 (2006).
36. Ganssle, P. J. *et al.* Ultra-low-field NMR relaxation and diffusion measurements using an optical magnetometer. *Angewandte Chemie (International ed. in English)* **53**, 9766–9770 (2014).
37. Tayler, M. C. D., Sjolander, T. F., Pines, A. & Budker, D. Nuclear magnetic resonance at millitesla fields using a zero-field spectrometer. *Journal of magnetic resonance (San Diego, Calif.: 1997)* **270**, 35–39 (2016).
38. Myers, W. *et al.* Calculated signal-to-noise ratio of MRI detected with SQUIDS and Faraday detectors in fields from 10 microT to 1.5 T. *Journal of magnetic resonance (San Diego, Calif.: 1997)* **186**, 182–192 (2007).
39. Clarke, J. & Braginski, A. I. *Applications of SQUIDS and SQUID systems* (Wiley-VCH, Weinheim, 2006).
40. Zotev, V. S. *et al.* Microtesla MRI of the human brain combined with MEG. *Journal of magnetic resonance (San Diego, Calif.: 1997)* **194**, 115–120 (2008).
41. Vesanen, P. T. *et al.* Hybrid ultra-low-field MRI and magnetoencephalography system based on a commercial whole-head neuromagnetometer. *Magnetic Resonance in Medicine* **69**, 1795–1804 (2013).
42. Clarke, J., Hatridge, M. & Mossle, M. SQUID-detected magnetic resonance imaging in microtesla fields. *Annual review of biomedical engineering* **9**, 389–413 (2007).
43. Gottardi, G., Mesirca, P., Agostini, C., Remondini, D. & Bersani, F. A four coil exposure system (tetracoil) producing a highly uniform magnetic field. *Bioelectromagnetics* **24**, 125–133 (2003).
44. Maslennikov, Y. CRYOTON Co. Ltd. <http://cryoton.org> (2017).
45. Seton, H. C., Hutchison, J. M. & Bussell, D. M. Liquid helium cryostat for SQUID-based MRI receivers. *Cryogenics* **45**, 348–355 (2005).
46. Tellez-Juárez, M. C. *et al.* Hydrogen storage in activated carbons produced from coals of different ranks: Effect of oxygen content. *International Journal of Hydrogen Energy* **39**, 4996–5002 (2014).
47. Weitzel, D. H. & White, L. E. Continuous analysis of ortho-parahydrogen mixtures. *Review of Scientific Instruments* **26**, 290–292 (1955).
48. Weitzel, D. H. & Park, O. E. Iron catalyst for production of liquid parahydrogen. *Review of Scientific Instruments* **27**, 57 (1956).
49. Weitzel, D. H., van Valin, C. C. & Draper, J. W. Design data for ortho-parahydrogen converters. In: *Timmerhaus K.D. (eds) Advances in Cryogenic Engineering. Advances in Cryogenic Engineering, vol 3. Springer, Boston, MA* (1960).

50. Weitzel, D. H. & White, L. E. Continuous analysis of ortho-parahydrogen mixtures. In: *Timmerhaus K.D. (eds) Advances in Cryogenic Engineering. Advances in Cryogenic Engineering, vol 1. Springer, Boston, MA (1960).*
51. Cowley, M. J. *et al.* Iridium N-heterocyclic carbene complexes as efficient catalysts for magnetization transfer from para-hydrogen. *J. Am. Chem. Soc.* **133**, 6134–6137 (2011).
52. Pravdivtsev, A. N., Yurkovskaya, A. V., Zimmermann, H., Vieth, H.-M. & Ivanov, K. L. Transfer of SABRE-derived hyperpolarization to spin-1/2 heteronuclei. *RSC Adv* **5**, 63615–63623 (2015).
53. Plaumann, M. *et al.* Parahydrogen-induced polarization transfer to ^{19}F in perfluorocarbons for ^{19}F NMR spectroscopy and MRI. *Chemistry - A European Journal* **19**, 6334–6339 (2013).
54. *VeSPA – Versatile Simulation, Pulses, and Analysis* <http://scion.duhs.duke.edu/vespa> (2017).
55. Levitt, M. H. *Spin dynamics. Basics of nuclear magnetic resonance*. 2nd ed. (John Wiley & Sons, Chichester, England, Hoboken, NJ, 2008).
56. Barskiy, D. A. *et al.* The feasibility of formation and kinetics of NMR signal amplification by reversible exchange (SABRE) at high magnetic field (9.4 T). *Journal of the American Chemical Society* **136**, 3322–3325 (2014).
57. Appelt, S., Häsing, F. W., Kühn, H., Sieling, U. & Blümich, B. Analysis of molecular structures by homo- and hetero-nuclear J-coupled NMR in ultra-low field. *Chemical Physics Letters* **440**, 308–312 (2007).
58. Permin, A. B. & Eisenberg, R. One-hydrogen polarization in hydroformylation promoted by platinum–tin and iridium carbonyl complexes. A new type of parahydrogen-induced effect. *J. Am. Chem. Soc.* **124**, 12406–12407 (2002).

Acknowledgements

This work was supported by the Deutsche Forschungsgemeinschaft (BE 1824/12-1). We thank Joern Engelmann for fruitful discussions.

Author Contributions

K.B., M.R., T.M., D.K., R.K., H.M., K.S., J.B. and M.P. designed research; K.B., M.R., C.B. and M.P. performed research; K.B., M.R., U.B., P.A., J.B. and M.P. analyzed data; K.B. and M.P. wrote the whole manuscript; and all authors reviewed the manuscript.

Additional Information

Supplementary information accompanies this paper at <https://doi.org/10.1038/s41598-017-13757-7>.

Competing Interests: The authors declare that they have no competing interests.

Publisher's note: Springer Nature remains neutral with regard to jurisdictional claims in published maps and institutional affiliations.



Open Access This article is licensed under a Creative Commons Attribution 4.0 International License, which permits use, sharing, adaptation, distribution and reproduction in any medium or format, as long as you give appropriate credit to the original author(s) and the source, provide a link to the Creative Commons license, and indicate if changes were made. The images or other third party material in this article are included in the article's Creative Commons license, unless indicated otherwise in a credit line to the material. If material is not included in the article's Creative Commons license and your intended use is not permitted by statutory regulation or exceeds the permitted use, you will need to obtain permission directly from the copyright holder. To view a copy of this license, visit <http://creativecommons.org/licenses/by/4.0/>.

© The Author(s) 2017

Publication 3

Multiple Quantum Coherences Hyperpolarized at Ultra-Low Fields

Kai Buckenmaier,^{*[a]} Klaus Scheffler,^[a, b] Markus Plaumann,^[c] Paul Fehling,^[a] Johannes Bernarding,^[c] Matthias Rudolph,^[a, d] Christoph Back,^[d] Dieter Koelle,^[d] Reinhold Kleiner,^[d] Jan-Bernd Hövener,^[e] and Andrey N. Pravdivtsev^{*[e]}

The development of hyperpolarization technologies enabled several yet exotic NMR applications at low and ultra-low fields (ULF), where without hyperpolarization even the detection of a signal from analytes is a challenge. Herein, we present a method for the simultaneous excitation and observation of homo- and heteronuclear multiple quantum coherences (from zero up to the third-order), which give an additional degree of freedom for ULF NMR experiments, where the chemical shift

variation is negligible. The approach is based on heteronuclear correlated spectroscopy (COSY); its combination with a phase-cycling scheme allows the selective observation of multiple quantum coherences of different orders. The nonequilibrium spin state and multiple spin orders are generated by signal amplification by reversible exchange (SABRE) and detected at ULF with a superconducting quantum interference device (SQUID)-based NMR system.

1. Introduction

The hyperpolarization of nuclear spins and the associated breakthroughs in physics, chemistry, biology and medicine continue to inspire the work of many scientists around the world. During the past decades, various hyperpolarization techniques have been developed^[1–14] to boost the magnetic resonance (MR) signal in order to bring new applications to industry^[15–17] and life-sciences.^[18–25] One of these methods is signal amplification by reversible exchange (SABRE),^[26–36] where parahydrogen (pH_2) is used to polarize dissolved molecules by

their mutual exchange with a transient complex. SABRE is unique in providing continuous hyperpolarization in the liquid state with high-throughput^[26,37] and is relatively cost-efficient.

SABRE at high magnetic field for high-resolution NMR encounters difficulties due to magnetic field inhomogeneity caused by pH_2 bubbling,^[38] this is not a problem for ultra-low field (ULF) NMR and even allows continuous SABRE,^[39] radio-wave amplification by stimulated emission of radiation (RASER)^[13] and QUASI-Resonance SABRE (QUASR).^[40]

Much effort is being undertaken to bring SABRE to “life sciences”, but despite considerable efforts, a clean, highly polarized, highly concentrated biologically relevant contrast agent was not produced yet.^[41–46]

When it comes to biomedical applications, usually, it is the goal to populate one dedicated spin state and, as a result, boost the MRI signal of the targeted nuclei. Here, we report the opposite effect: we discovered that in SABRE experiments at low magnetic fields various multiple spin orders are hyperpolarized. It was revealed by simultaneous observation of hyperpolarized homo- (1H) and heteronuclear (1H - ^{19}F) zero-order and multiple quantum coherences (QCs), up to the third order. This confirms that redistribution of pH_2 spin alignment in SABRE results not only in the substrate's magnetization but also in the population of multiple spin orders, including homo- and heteronuclear zz-orders and singlet spin states.^[27,35,36,47–49] This observation illustrates that the transfer of pH_2 spin order to a substrate at the low magnetic field can be greatly improved by using more targeted polarization transfer techniques discussed elsewhere.^[40,50]

The redistribution of pH_2 spin alignment and hyperpolarized multiple quantum coherences were revealed using a superconducting quantum interference device (SQUID)-based ULF MR spectrometer, designed as a field-cycling system, which operates in the magnetic field range of 10 μT to 20 mT. In this range of fields SQUID-based magnetic field sensors^[51] and

[a] Dr. K. Buckenmaier, Prof. Dr. K. Scheffler, P. Fehling, Dr. M. Rudolph
High-Field Magnetic Resonance Center
Max Planck Institute for Biological Cybernetics
Max-Planck-Ring 11, 72076, Tübingen, Germany
E-mail: kai.buckenmaier@tuebingen.mpg.de

[b] Prof. Dr. K. Scheffler
Department for Biomedical Magnetic Resonance
University of Tübingen
Hoppe-Seyler-Str. 3, 72076, Tübingen, Germany

[c] Dr. M. Plaumann, Prof. Dr. J. Bernarding
Institute for Biometrics and Medical Informatics
Otto-von-Guericke University
Building 02, Leipziger Str. 44, 39120, Magdeburg, Germany

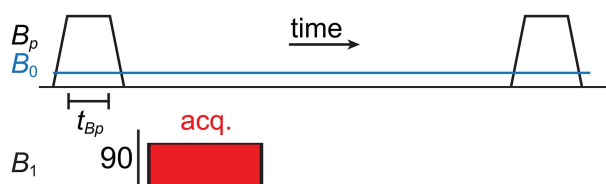
[d] Dr. M. Rudolph, Dr. C. Back, Prof. Dr. D. Koelle, Prof. Dr. R. Kleiner
Physikalisches Institut and
Center for Quantum Science (CQ) in LISA⁺
University of Tübingen
Auf der Morgenstelle 14, 72076, Tübingen, Germany

[e] Prof. Dr. J.-B. Hövener, Dr. A. N. Pravdivtsev
Section Biomedical Imaging
Molecular Imaging North Competence Center (MOIN CC)
Department of Radiology and Neuroradiology
University Medical Center Kiel, Kiel University
Am Botanischen Garten 14, 24114, Kiel, Germany
E-mail: andrey.pravdivtsev@rad.uni-kiel.de

Supporting information for this article is available on the WWW under <https://doi.org/10.1002/cphc.201900757>

© 2019 The Authors. Published by Wiley-VCH Verlag GmbH & Co. KGaA.
This is an open access article under the terms of the Creative Commons Attribution License, which permits use, distribution and reproduction in any medium, provided the original work is properly cited.

(a) ULF SABRE



(b) ULF SABRE spectra

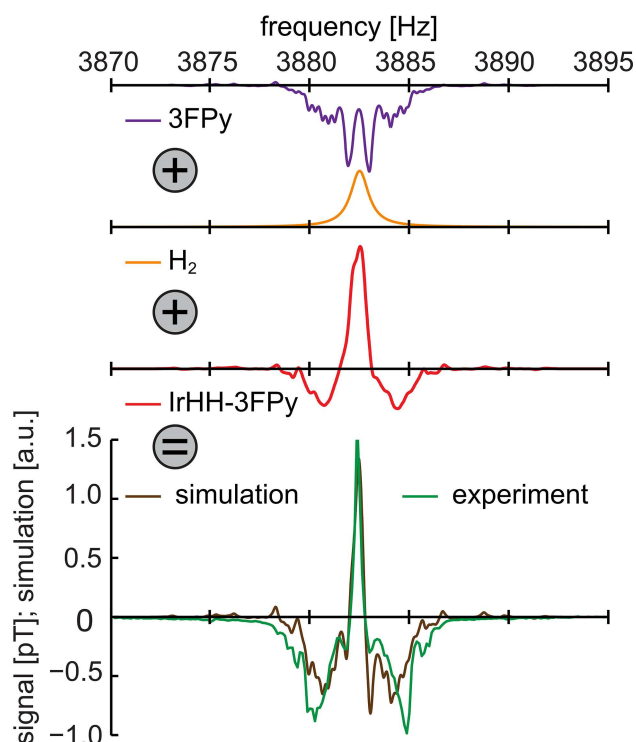


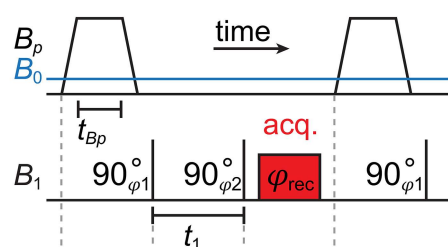
Figure 1. ULF SABRE scheme (a) and corresponding simulated and experimental spectra (b). After hyperpolarization at $B_p = 5.2$ mT and a 90° excitation pulse at $B_0 = 91$ μ T, the SABRE signal is acquired. Simulated 1 H-spectra of hyperpolarized 3FPy substrate (purple), H_2 (orange) and IrHH-3FPy complex (red). The weighted sum of these spectra (brown) was fitted to the experimental data (green). This data indicates that all three constituents of SABRE (H_2 , Ir-complex and substrate) were hyperpolarized and observed.

optical magnetometers^[52] become superior to conventional Faraday coils.^[53]

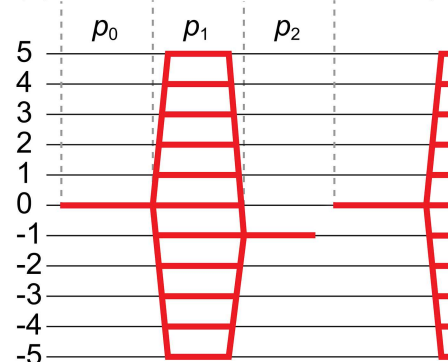
The combination of this fast field-cycling SQUID-based MR system and the continuous generation of SABRE allows to observe hyperpolarized substrate, H_2 and SABRE complexes (IrHH-substrate) at ULF (Figure 1). Before, similar measurements were achieved only at much higher magnetic fields.^[54,55] The superposition of several hyperpolarized species or states in the 1 H ULF SABRE spectrum is evident (Figure 1b) and in the absence of chemical shift resolution the sign of polarization can serve as a contrast; at 91 μ T the chemical shift difference of 1 ppm corresponds to only 4 mHz frequency variation.

In the main text, the findings and their evaluation will be demonstrated on 3-fluoropyridine (3FPy), used as a substrate

(a) ULF COSY



(b) Coherence Transfer Pathway



Scheme 1. ULF COSY experiment (a) and the corresponding evolution of the quantum coherences, p_n (b). The coherence selection pathway starts from different zero quantum coherences and multiplet spin orders with $p_0 = 0$, a first 90° pulse converts these spin order into quantum coherences p_1 for a period of time, t_1 , (\rightarrow frequency 1 domain) and after the second 90° pulse NMR signal observation starts (\rightarrow frequency 2 domain), therefore only $p_2 = -1$ is retained (acq.-block stands for signal acquisition).

with the ubiquitous SABRE catalyst [IrMesCODCI].^[56] Fluorinated variants of common SABRE substrates (3FPy and ethyl 5-fluoronicotinate – see the Supporting Information) were used here to demonstrate the presence of homo- and heteronuclear quantum coherences.

2. Results and Discussion

2.1. ULF COSY Scheme

To elucidate the hyperpolarized spin states, we modified a conventional correlation spectroscopy (COSY) pulse sequence (Scheme 1a) for ULF NMR^[57,58] – ULF COSY, by adding a hyperpolarization phase for each t_1 variation step and simultaneous excitation of 1 H and 19 F spins. Note that we also tried to implement the method with a variable excitation flip angle,^[59–61] however, in the given conditions it was shown to be unpractical (cf. Supporting Information, Section 4).

The ULF COSY sequence starts with a prepolarization phase at the magnetic field strength B_p for the period of t_{Bp} by means of SABRE. When the magnetic field was reduced to the observation field, B_0 , two 90° 1 H- 19 F excitation pulses with the phases φ_1 and φ_2 and a variable interpulse interval, t_1 , were

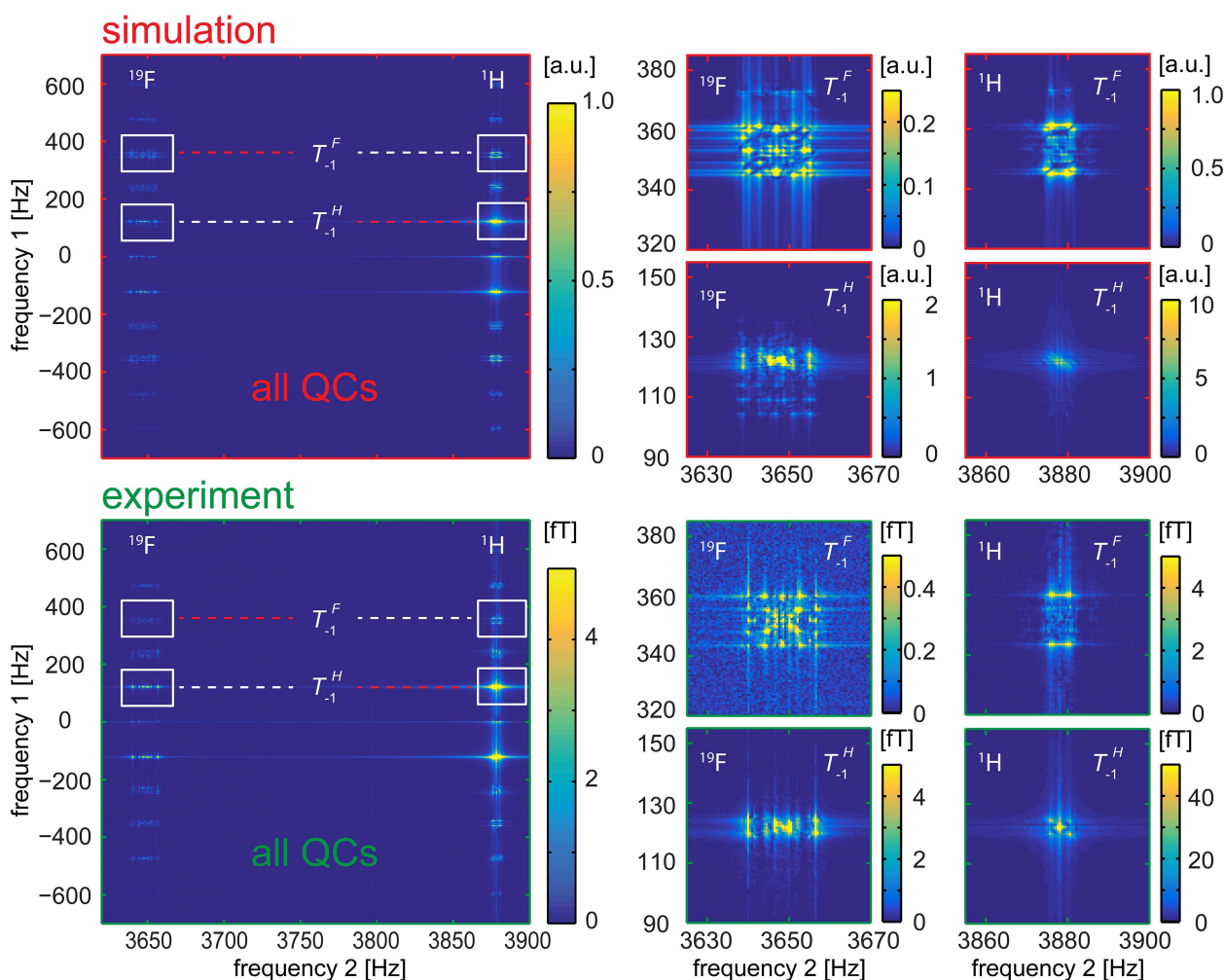


Figure 2. Hyperpolarized quantum coherences measured with the ULF COSY experiment ($B_p = 5.2$ mT and $B_0 = 91$ μ T): simulated (top) and experimental (bottom) amplitude spectra of 3FPy. T_y^x is a symbol for QCs, where y is the order of the QC and x indicates the types of nuclei involved (Table S5). On the right, the zoomed out T_{-1}^H and T_{-1}^F QCs measured at ^1H and ^{19}F resonances are shown (indicated by the white rectangles). Red and white dashed lines mark the diagonal and off-diagonal peaks, respectively. Up to third-order coherences were observed. Simulations reproduced experimental details.

applied. After the second 90° pulse, the signal was acquired with a receiver phase φ_{rec} . A 2D Fourier transformation along the direct readout (\rightarrow frequency 2) and the indirect " t_1 direction" (\rightarrow frequency 1) result in a 2D spectrum (Figure 2).

2.2. ULF COSY Spectrum

A relatively narrow spectral width (SW) of 4 kHz instead of the required 40 kHz in the indirect dimension was chosen to obtain a highly resolved 2D ULF COSY spectrum at a reasonable time (< 8 h), however, as a result the signals of the quantum coherences folded into the bandwidth between -2 kHz and $+2$ kHz (Figure 2 and Table S5 in the Supporting Information). Such frequencies can be easily obtained using the product operator formalism (SI, Section 7).^[62]

Four uncoupled undistinguishable ^1H spins and one ^{19}F spin in maximum have 26 different sorts of quantum coherences with different frequencies due to the Zeeman interaction

(Table S5); a total number of coherences of 5 spin- $1/2$ system is $2^4(2^5-1)=496$. Although J-coupling constants make the system more complex, at ULFs of 91 μ T, the Zeeman interaction is still the leading term which defines the frequencies of quantum coherences and J-coupling only adds multiplicity to the peaks (Figure 2).

These coherences can be encoded by ULF COSY during the time period t_1 and observed as separate peaks in a 2D spectrum. By chance, at the given magnetic field, $B_0 \approx 91$ μ T, and SW = 4 kHz, some QCs have the same (aliased) frequencies and only 15 peaks were clearly separable in the simulations. Experimentally only 11 peaks were obtained (Figure 2a and Figure S5 in the Supporting Information). These peaks belong to QCs from zero up to the third order.

This demonstrates that not only one and two-spin orders like \hat{I}_{kz} and $\hat{I}_{kz}\hat{I}_{mz}$ are polarized by means of SABRE but also 3-spin orders like $\hat{I}_{kz}\hat{I}_{mz}\hat{I}_{nz}$ are populated [see SI, Eq. (S3)]. The signal intensity of predicted higher-order QCs (fourth and fifth) was below the noise level of the setup.

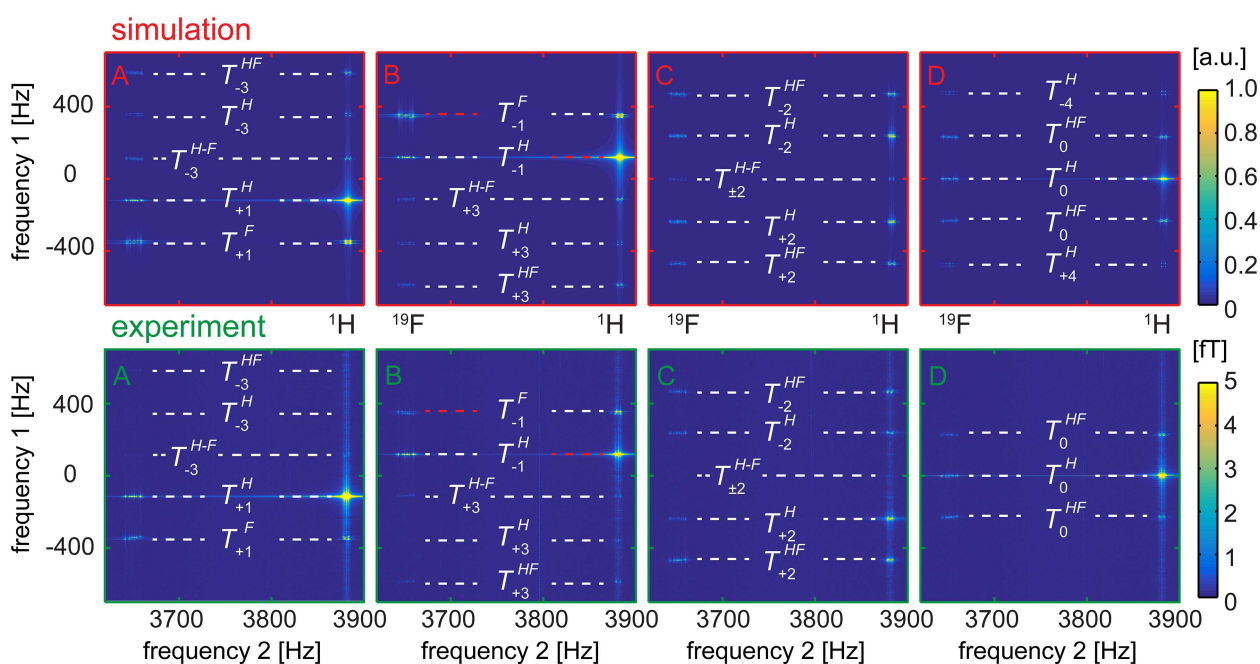


Figure 3. Separation of QCs in the coherence selective ULF COSY experiment ($B_p = 5.2$ mT and $B_0 = 91$ μ T): simulated (top) and experimental (bottom) amplitude spectra of 3FPy obtained with four different phase alternating methods (here A–D corresponds to phase cycling schemes mentioned in the text and given in the SI, Table S4). T_y^x is a symbol of QCs, where y is the order of the QC and x indicates the types of nuclei involved (SI, Table S5). The red and white dashed lines mark the diagonal and off-diagonal peaks, respectively. ULF COSY spectra without phase cycling are shown in Figure 2.

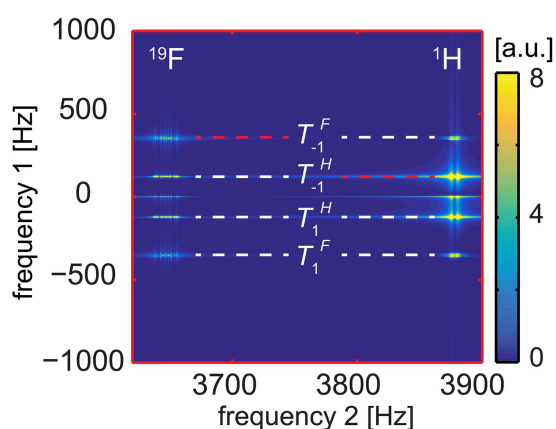


Figure 4. Simulated ULF COSY amplitude spectrum of 3FPy after polarization of longitudinal states alone (thermal Zeeman polarization of order $p = 0$ and rank $l = 1$). Note that in the case of SABRE higher-order quantum coherences appear (Figures 2 and 3). The COSY spectrum with an initial longitudinal magnetization shows only first order (and zero H–H orders) quantum coherences. Also, note that the shapes of the peaks are different.

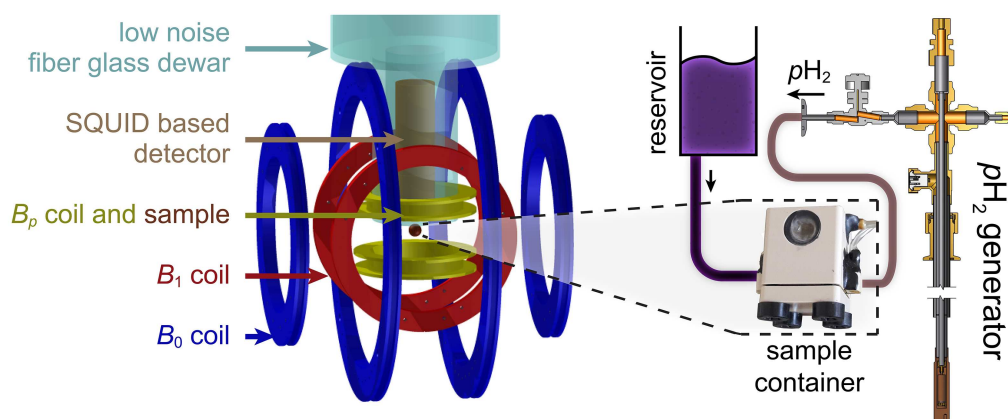
Note, that only two peaks are “diagonal” COSY peaks, which are the result of the “-1” quantum coherence evolution during the t_1 time interval and acquisition block (indicated by red dashed lines on Figures 2–4). All other peaks are “off-diagonal” peaks.

2.3. Coherence Selective ULF COSY

The COSY experiment with phase cycling solves the problem of overlapping aliased signals. For the selective observation of multiple quantum coherences the experiment was repeated four times with the following phases of two excitation pulses (Scheme 1): $\varphi_1 = x, y, -x, -y$, $\varphi_2 = 4(x)$. Then, four different φ_{rec} cycles were used to select different orders, p_1 , of quantum coherences during the t_1 interval: (A) $\varphi_{rec} = x, -y, -x, y$ selects $p_1 = 1 + 4n$; (B) $\varphi_{rec} = x, y, -x, -y$ selects $p_1 = -1 + 4n$; (C) $\varphi_{rec} = x, -x, x, -x$ selects $p_1 = 2 + 4n$; (D) $\varphi_{rec} = 4(x)$ selects $p_1 = 4n$ with n being an integer number (Figure 3 and Table S4). There are 11 multiple quantum coherences for a 5 spin-1/2 system: $0, \pm 1, \pm 2, \pm 3, \pm 4$ and ± 5 . And all of them can be excited with the first 90° pulse [(SI, Eq (S3))] if appropriate multiple spin orders are initially populated (SI, Section 5).

2.4. Thermally Polarized ULF COSY Spectrum

To demonstrate that higher-order quantum coherences in ULF COSY spectra are the result of the population of higher-order spin states and not a coherent evolution of magnetization during the COSY sequence we performed additional simulations. A COSY spectrum of a system with only longitudinal initial polarization, i.e. thermal Zeeman polarization of order $p = 0$ and rank $l = 1$, showed quantum coherences up to the first order only (Figure 4); SABRE polarized systems exhibit higher QCs (Figures 2 and 3).



Scheme 2. Scheme of the ULF SQUID based MR setup for the hyperpolarization of multiple quantum coherences by SABRE. Freshly produced $p\text{H}_2$ was supplied to the sample container inside a magnetic shield, where the field was varied between the polarizing field B_p and the measurement field B_0 . For details, see Ref. [65].

3. Conclusions

To summarize, we demonstrated the hyperpolarization of homo- and heteronuclear, multiple spin states in a SABRE experiment using SQUID-based ULF NMR by observation of multiple QCs. COSY at ULF enables the simultaneous measurement at different resonance frequencies (i), selection of different QCs by phase cycling (ii) and does not require a very precise flip angle calibration or experimental performance to extract small polarization of high spin-order from the one big signal (like in 1D experiments) that comprises all spin orders (iii).

Although QCs from zero up to the fifth-order could theoretically be measured for 3FPy, experimentally we obtained and assigned only QCs in the range from -3 to $+3$ within a single experiment or selectively using a phase cycling scheme. As the simulations showed, the signal intensities of higher-order QCs are dropping rapidly and are below the noise level.

We believe that this contribution is an important experimental confirmation of a known and underestimated evidence that at the low magnetic field the polarization distributes among all strongly-coupled spins even if the direct source-target nuclear spin coupling is small. Moreover, the demonstration that multiple quantum coherences are hyperpolarized with SABRE is important information for continuous improvement of the SABRE performance, but it may be even more important for some exotic methods such as ultra-low field magnetometers^[63] and RASER.^[13] MR at ULF is a quickly developing MR topic^[64] and this work puts a bridge to 2D ULF spectroscopy, whose role at high-resolution NMR cannot be overestimated.

Experimental Section

Hardware

In essence the SQUID-NMR spectrometer consists of a coil generating the static magnetic field, B_0 , a Helmholtz coil to excite

the spins by pulses, B_1 , a polarizing coil to generate the (elevated) field for SABRE, B_p , and a SQUID-based detector, which is positioned inside a low noise fiberglass Dewar (Scheme 2). The polarizing coil enables fast switching (≈ 10 ms) between B_p and B_0 and is placed inside a three-layered μ -metal shield. For the experiments, B_p is set to the optimal strength for the SABRE hyperpolarization of ^{19}F of the ligands, 5.2 mT,^[35] and reduced to $B_0 = 91 \mu\text{T}$ for observation of the free induction decay (FID) (see Scheme 1a and Figure S1). 1D and 2D NMR spectra are obtained by 1D and 2D Fourier transformation of the corresponding FIDs. The setup is described in detail in Ref. [65].

Sample Preparation

Experiments were carried out using two different samples. **Sample 1** contained 29.6 μl 3-fluoropyridine (3FPy) and 10.5 mg of the $[\text{IrMesCODCl}]^{[56]}$ self-synthesized according to Ref. [66] (IMes = 1,3-bis (2,4,6-trimethylphenyl) imidazole-2-ylidene, COD = cyclooctadiene). Both substances were dissolved in 15 ml methanol. **Sample 2** was prepared using 48.7 μl ethyl 5-fluoronicotinate (EFNA) and the same amount of the $[\text{IrMesCODCl}]$ (10.5 mg) and methanol (15 ml). Results obtained with **Sample 1** are reported in the main text, while those of **Sample 2** are in SI. All samples were filled into a 2 ml sample container that was held at room temperature at the isocenter of the SQUID-based MR system under atmospheric pressure. This container was connected to a reservoir filled with the rest of the sample (Scheme 1). $p\text{H}_2$ was bubbled continuously through the sample container at a rate of $\approx 42 \text{ scm}^3/\text{min}$. The experiment was carried out for about 8 hours until ≈ 13 ml of the solution was evaporated as monitored by MR (Figure S9). The initial concentrations of the Ir-catalyst and of the fluorinated ligand were 1 mM and 23 mM, respectively.

Computational Methods

To analyze the experimental results, density matrix simulations were performed using the code of the Magnetic resonance Open source Initiative (MOIN)^{[67][27]} in the following steps:

1. Setting up a spin system of the non-polarized substrate: four ^1H , one ^{19}F for 3FPy or three ^1H , one ^{19}F for EFNA;
2. Additions of two singlet-state hydride protons ($p\text{H}_2$) to the system forming the polarized Ir-complex: IrHH-3FPy or IrHH-

EFNA, where IrHH represents the hydride protons of transient Ir-complex;

3. Removal of coherences of the density matrix written in the Eigen basis of the systems Hamiltonian at B_p (polarization transfer in Ir-complex);
4. Removal of the two hydride protons from the system (dissociation of the substrate);
5. Application of the pulse sequence to the free substrate (3FPy or EFNA), dissolved H_2 and IrHH-3FPy or IrHH-EFNA complex. The Liouville von Neuman equation was used to evolve the spin system.

J-coupling constants for 3FPy and EFNA are listed in Tables S1 and S2.

To investigate the effect of pulse sequences on the Ir-complex, step 4 (dissociation) was omitted. J-coupling constants were taken from literature or were estimated,^[35] excitation pulses were treated as ideal rotations with zero duration (hard pulses), and spin relaxation was neglected. More details and an analytical description of the sequence performance is given in the supplementary materials (SI, Sections 2–4). The code for obtaining the simulated COSY spectra is provided via Ref. [66].

Supporting Information

NMR parameters of 3FPy and EFNA, additional materials to ULF SABRE experiments, measurement of signal stability during the long lasting experiments, evaluation of QCs frequencies and used phase cycling schemes (.PDF)

Acknowledgements

A.P. and J.-B.H. acknowledge support by the Emmy Noether Program of the DFG (HO 4604/2-2), DFG-RFBR grant (HO 4604/3-1, N° 19-53-12013), the Cluster of Excellence "Inflammation at Interfaces" (EXC306). Kiel University and the Medical Faculty are acknowledged for supporting the Molecular Imaging North Competence Center (MOIN CC) as a core facility for imaging in vivo. MOIN CC was founded by a grant of the European Regional Development Fund (ERDF) and the Zukunftsprogramm Wirtschaft of Schleswig-Holstein (Project no. 122-09-053). M.P. and J.B. acknowledge support by DFG grant (BE 1824/12-1). K.B. thanks Jonas Bause for fruitful discussions.

Conflict of Interest

The authors declare no conflict of interest.

Keywords: hyperpolarization · multiple quantum coherence · parahydrogen · SABRE · SQUID

- [1] C. R. Bowers, D. P. Weitekamp, *J. Am. Chem. Soc.* **1987**, *109*, 5541–5542.
- [2] S. Glöggler, J. Colell, S. Appelt, *J. Magn. Reson.* **2013**, *235*, 130–142.
- [3] F. Reineri, T. Boi, S. Aime, *Nat. Commun.* **2015**, *6*, ncomms6858.

- [4] J. H. Ardenkjær-Larsen, B. Fridlund, A. Gram, G. Hansson, L. Hansson, M. H. Lerche, R. Servin, M. Thaning, K. Golman, *PNAS* **2003**, *100*, 10158–10163.
- [5] X. Ji, A. Bornet, B. Vuichoud, J. Milani, D. Gajan, A. J. Rossini, L. Emsley, G. Bodenhausen, S. Jannin, *Nat. Commun.* **2017**, *8*, 13975.
- [6] X. J. Chen, H. E. Möller, M. S. Chawla, G. P. Cofer, B. Driehuys, L. W. Hedlund, G. A. Johnson, *Magn. Reson. Med.* **1999**, *42*, 721–728.
- [7] M. L. Hirsch, N. Kalechofsky, A. Belzer, M. Rosay, J. G. Kempf, *J. Am. Chem. Soc.* **2015**, *137*, 8428–8434.
- [8] K. V. Kovtunov, E. Pokochueva, O. Salnikov, S. Cousin, D. Kurzbach, B. Vuichoud, S. Jannin, E. Chekmenev, B. Goodson, D. Barskiy, *Chem. Asian J.* **2018**, *13*, 1857–1871.
- [9] A. B. Schmidt, S. Berner, W. Schimpf, C. Müller, T. Lickert, N. Schwaderlapp, S. Knecht, J. G. Skinner, A. Dost, P. Rovedo, *Nat. Commun.* **2017**, *8*, ncomms14535.
- [10] V. V. Zhivonitko, V.-V. Telkki, K. Chernichenko, T. Repo, M. Leskelä, V. Sumerin, I. V. Koptuyug, *J. Am. Chem. Soc.* **2014**, *136*, 598–601.
- [11] J. McCormick, S. Korchak, S. Mamone, Y. N. Ertas, Z. Liu, L. Verlinsky, S. Wagner, S. Glöggler, L.-S. Bouchard, *Angew. Chem. Int. Ed.* **2018**, *57*, 10692–10696.
- [12] J. Wang, F. Kreis, A. J. Wright, R. L. Hesketh, M. H. Levitt, K. M. Brindle, *Magn. Reson. Med.* **2018**, *79*, 741–747.
- [13] M. Siefert, S. Lehmkuhl, A. Liebisch, B. Blümich, S. Appelt, *Nat. Phys.* **2017**, *13*, 568–572.
- [14] J.-B. Hövener, A. N. Pravdivtsev, B. Kidd, C. R. Bowers, S. Glöggler, K. V. Kovtunov, M. Plaumann, R. Katz-Brull, K. Buckenmaier, A. Jerschow, *Angew. Chem. Int. Ed.* **2018**, *57*, 11140–11162.
- [15] K. V. Kovtunov, M. L. Truong, D. A. Barskiy, O. G. Salnikov, V. I. Bukhtiyarov, A. M. Coffey, K. W. Waddell, I. V. Koptuyug, E. Y. Chekmenev, *J. Phys. Chem. C* **2014**, *118*, 28234–28243.
- [16] V. V. Zhivonitko, V.-V. Telkki, I. V. Koptuyug, *Angew. Chem. Int. Ed.* **2012**, *51*, 8054–8058.
- [17] V.-V. Telkki, V. V. Zhivonitko, S. Ahola, K. V. Kovtunov, J. Jokisaari, I. V. Koptuyug, *Angew. Chem. Int. Ed.* **2010**, *49*, 8363–8366.
- [18] M. J. Albers, R. Bok, A. P. Chen, C. H. Cunningham, M. L. Zierhut, V. Y. Zhang, S. J. Kohler, J. Tropp, R. E. Hurd, Y.-F. Yen, *Cancer Res.* **2008**, *68*, 8607–8615.
- [19] E. Cavallari, C. Carrera, S. Aime, F. Reineri, *ChemPhysChem* **2019**, *20*, 318–325.
- [20] C. H. Cunningham, J. Y. C. Lau, A. P. Chen, B. J. Geraghty, W. J. Perks, I. Roifman, G. A. Wright, K. A. Connelly, *Circ. Res.* **2016**, *119*, 1177–1182.
- [21] S. J. Nelson, J. Kurhanewicz, D. B. Vigneron, P. E. Z. Larson, A. L. Harzstark, M. Ferrone, M. van Criekinge, J. W. Chang, R. Bok, I. Park, *Sci. Transl. Med.* **2013**, *5*, 198ra108–198ra108.
- [22] R. Aggarwal, D. B. Vigneron, J. Kurhanewicz, *Eur. Urol.* **2017**, *72*, 1028–1029.
- [23] A. B. Schmidt, S. Berner, M. Braig, M. Zimmermann, J. Hennig, D. von Elverfeldt, J.-B. Hövener, *PLoS One* **2018**, *13*, e0200141.
- [24] K. V. Kovtunov, B. E. Kidd, O. G. Salnikov, L. B. Bales, M. E. Gemeinhardt, J. Gesiorski, R. V. Shchepin, E. Y. Chekmenev, B. M. Goodson, I. V. Koptuyug, *J. Phys. Chem. C* **2017**, *121*, 25994–25999.
- [25] J. G. Skinner, L. Menichetti, A. Flori, A. Dost, A. B. Schmidt, M. Plaumann, F. A. Gallagher, J.-B. Hövener, *Mol. Imaging Biol.* **2018**, *20*, 902–918.
- [26] R. W. Adams, J. A. Aguilar, K. D. Atkinson, M. J. Cowley, P. I. P. Elliott, S. B. Duckett, G. G. R. Green, I. G. Khazal, J. López-Serrano, D. C. Williamson, *Science* **2009**, *323*, 1708–1711.
- [27] A. N. Pravdivtsev, A. V. Yurkovskaya, H.-M. Vieth, K. L. Ivanov, R. Kaptein, *ChemPhysChem* **2013**, *14*, 3327–3331.
- [28] N. Eshuis, N. Hermkens, B. J. A. van Weerdenburg, M. C. Feiters, F. P. J. T. Rutjes, S. S. Wijmenga, M. Tessari, *J. Am. Chem. Soc.* **2014**, *136*, 2695–2698.
- [29] K. M. Appleby, R. E. Mewis, A. M. Olaru, G. G. R. Green, I. J. S. Fairlamb, S. B. Duckett, *Chem. Sci.* **2015**, *6*, 3981–3993.
- [30] A. N. Pravdivtsev, A. V. Yurkovskaya, H.-M. Vieth, K. L. Ivanov, *J. Phys. Chem. B* **2015**, *119*, 13619–13629.
- [31] N. Eshuis, B. J. A. van Weerdenburg, M. C. Feiters, F. P. J. T. Rutjes, S. S. Wijmenga, M. Tessari, *Angew. Chem. Int. Ed.* **2015**, *54*, 1481–1484.
- [32] T. Theis, M. L. Truong, A. M. Coffey, R. V. Shchepin, K. W. Waddell, F. Shi, B. M. Goodson, W. S. Warren, E. Y. Chekmenev, *J. Am. Chem. Soc.* **2015**, *137*, 1404–1407.
- [33] R. V. Shchepin, D. A. Barskiy, A. M. Coffey, T. Theis, F. Shi, W. S. Warren, B. M. Goodson, E. Y. Chekmenev, *ACS Sens.* **2016**, *1*, 640–644.
- [34] T. Theis, G. X. Ortiz, A. W. J. Logan, K. E. Claytor, Y. Feng, W. P. Huhn, V. Blum, S. J. Malcolmson, E. Y. Chekmenev, Q. Wang, *Sci. Adv.* **2016**, *2*, e1501438.

- [35] K. Buckenmaier, M. Rudolph, C. Back, T. Misztal, U. Bommerich, P. Fehling, D. Koelle, R. Kleiner, H. A. Mayer, K. Scheffler, *Sci. Rep.* **2017**, *7*, 13431.
- [36] J. Bae, Z. Zhou, T. Theis, W. S. Warren, Q. Wang, *Sci. Adv.* **2018**, *4*, eaar2978.
- [37] J.-B. Hövener, N. Schwaderlapp, T. Lickert, S. B. Duckett, R. E. Mewis, L. A. R. Highton, S. M. Kenny, G. G. R. Green, D. Leibfritz, J. G. Korvink, *Nat. Commun.* **2013**, *4*, ncomms3946.
- [38] A. Svyatova, I. V. Skovpin, N. V. Chukanov, K. V. Kovtunov, E. Y. Chekmenev, A. N. Pravdivtsev, J.-B. Hövener, I. V. Koptuyug, *Chem. Eur. J.* **2019**, *25*, 8465–8470.
- [39] J.-B. Hövener, S. Knecht, N. Schwaderlapp, J. Hennig, D. von Elverfeldt, *ChemPhysChem* **2014**, *15*, 2451–2457.
- [40] T. Theis, N. M. Ariyasingha, R. V. Shchepin, J. R. Lindale, W. S. Warren, E. Y. Chekmenev, *J. Phys. Chem. Lett.* **2018**, 6136–6142.
- [41] K. V. Kovtunov, L. M. Kovtunova, M. E. Gemeinhardt, A. V. Bukhtiyarov, J. Gesiorski, V. I. Bukhtiyarov, E. Y. Chekmenev, I. V. Koptuyug, B. M. Goodson, *Angew. Chem. Int. Ed.* **2017**, *56*, 10433–10437.
- [42] B. E. Kidd, J. L. Gesiorski, M. E. Gemeinhardt, R. V. Shchepin, K. V. Kovtunov, I. V. Koptuyug, E. Y. Chekmenev, B. M. Goodson, *J. Phys. Chem. C* **2018**, *122*, 16848–16852.
- [43] D. A. Barskiy, L. A. Ke, X. Li, V. Stevenson, N. Widarman, H. Zhang, A. Truxal, A. Pines, *J. Phys. Chem. Lett.* **2018**, *9*, 2721–2724.
- [44] J. F. P. Colell, M. Emondts, A. W. J. Logan, K. Shen, J. Bae, R. V. Shchepin, G. X. Ortiz, P. Spannring, Q. Wang, S. J. Malcolmson, *J. Am. Chem. Soc.* **2017**, *139*, 7761–7767.
- [45] H. Zeng, J. Xu, M. T. McMahon, J. A. B. Lohman, P. C. M. van Zijl, *J. Magn. Reson.* **2014**, *246*, 119–121.
- [46] W. Iali, A. M. Olaru, G. G. R. Green, S. B. Duckett, *Chem. Eur. J.* **2017**, *23*, 10491–10495.
- [47] A. N. Pravdivtsev, A. V. Yurkovskaya, H. Zimmermann, H.-M. Vieth, K. L. Ivanov, *RSC Adv.* **2015**, *5*, 63615–63623.
- [48] K. Shen, A. W. J. Logan, J. F. P. Colell, J. Bae, G. X. Ortiz, T. Theis, W. S. Warren, S. J. Malcolmson, Q. Wang, *Angew. Chem. Int. Ed.* **2017**, *56*, 12112–12116.
- [49] R. E. Mewis, K. D. Atkinson, M. J. Cowley, S. B. Duckett, G. G. R. Green, R. A. Green, L. A. R. Highton, D. Kilgour, L. S. Lloyd, J. A. B. Lohman, *Magn. Reson. Chem.* **2014**, *52*, 358–369.
- [50] J. R. Lindale, S. L. Eriksson, C. P. N. Tanner, Z. Zhou, J. F. P. Colell, G. Zhang, J. Bae, E. Y. Chekmenev, T. Theis, W. S. Warren, *Nat. Commun.* **2019**, *10*, 395.
- [51] J. Clarke, M. Hatridge, M. Mößle, *Annu. Rev. Biomed. Eng.* **2007**, *9*, 389–413.
- [52] T. Theis, M. P. Ledbetter, G. Kervern, J. W. Blanchard, P. J. Ganssle, M. C. Butler, H. D. Shin, D. Budker, A. Pines, *J. Am. Chem. Soc.* **2012**, *134*, 3987–3990.
- [53] W. Myers, D. Slichter, M. Hatridge, S. Busch, M. Mößle, R. McDermott, A. Trabesinger, J. Clarke, *J. Magn. Reson.* **2007**, *186*, 182–192.
- [54] A. N. Pravdivtsev, K. L. Ivanov, A. V. Yurkovskaya, P. A. Petrov, H.-H. Limbach, R. Kaptein, H.-M. Vieth, *J. Magn. Reson.* **2015**, *261*, 73–82.
- [55] D. A. Barskiy, K. V. Kovtunov, I. V. Koptuyug, P. He, K. A. Groome, Q. A. Best, F. Shi, B. M. Goodson, R. V. Shchepin, M. L. Truong, *ChemPhysChem* **2014**, *15*, 4100–4107.
- [56] L. D. Vazquez-Serrano, B. T. Owens, J. M. Buriak, *Inorg. Chim. Acta* **2006**, *359*, 2786–2797.
- [57] W. P. Aue, E. Bartholdi, R. R. Ernst, *J. Chem. Phys.* **1976**, *64*, 2229–2246.
- [58] J. Keeler, *Understanding NMR Spectroscopy*, University of Cambridge, **2002**.
- [59] K. L. Ivanov, K. Miesel, H.-M. Vieth, A. V. Yurkovskaya, R. Z. Sagdeev, *Z. Phys. Chem.* **2003**, *217*, 1641–1659.
- [60] E. A. Nasibulov, A. N. Pravdivtsev, A. V. Yurkovskaya, N. N. Lukzen, H.-M. Vieth, K. L. Ivanov, *Z. Phys. Chem.* **2013**, *227*, 929–953.
- [61] A. N. Pravdivtsev, A. V. Yurkovskaya, P. A. Petrov, H.-M. Vieth, *Phys. Chem. Chem. Phys.* **2017**, *19*, 25961–25969.
- [62] O. W. Sørensen, G. W. Eich, M. H. Levitt, G. Bodenhausen, R. R. Ernst, *Prog. Nucl. Magn. Reson. Spectrosc.* **1984**, *16*, 163–192.
- [63] T. Theis, P. Ganssle, G. Kervern, S. Knappe, J. Kitching, M. P. Ledbetter, D. Budker, A. Pines, *Nat. Phys.* **2011**, *7*, 571–575.
- [64] R. Körber, J.-H. Storm, H. Seton, J. P. Mäkelä, R. Paetau, L. Parkkonen, C. Pfeiffer, B. Riaz, J. F. Schneiderman, H. Dong, *Supercond. Sci. Technol.* **2016**, *29*, 113001.
- [65] K. Buckenmaier, M. Rudolph, P. Fehling, T. Steffen, C. Back, R. Bernard, R. Pohmann, J. Bernarding, R. Kleiner, D. Koelle, *Rev. Sci. Instrum.* **2018**, *89*, 125103.
- [66] M. J. Cowley, R. W. Adams, K. D. Atkinson, M. C. R. Cockett, S. B. Duckett, G. G. R. Green, J. A. B. Lohman, R. Kerssebaum, D. Kilgour, R. E. Mewis, *J. Am. Chem. Soc.* **2011**, *133*, 6134–6137.
- [67] A. N. Pravdivtsev, J.-B. Hövener, *MOIN Spin Library*, (www.moincc.de/method-development/mr/moin-spin-library) UKSH, University Kiel, **2018**.

Manuscript received: September 16, 2019
 Revised manuscript received: September 17, 2019
 Accepted manuscript online: September 19, 2019
 Version of record online: October 17, 2019

Publication 4

The effects of nitroxide structure upon ^1H Overhauser dynamic nuclear polarization efficacy at ultralow-field

Cite as: J. Chem. Phys. 155, 144203 (2021); doi: 10.1063/5.0064342

Submitted: 22 July 2021 • Accepted: 17 September 2021 •

Published Online: 12 October 2021



View Online



Export Citation



CrossMark

Paul Fehling,¹ Kai Buckenmaier,^{1,a)} Sergey A. Dobrynin,² Denis A. Morozov,² Yuliya F. Polienko,² Yulia V. Khoroshunova,^{2,3} Yulia Borozdina,¹ Philipp Mayer,¹ Jörn Engelmann,¹ Klaus Scheffler,^{1,4} Goran Angelovski,^{1,5} and Igor A. Kirilyuk²

AFFILIATIONS

¹Max Planck Institute for Biological Cybernetics, 72076 Tübingen, Germany

²N.N. Vorozhtsov Institute of Organic Chemistry SB RAS, 630090 Novosibirsk, Russia

³Novosibirsk State University, 630090 Novosibirsk, Russia

⁴Department for Biomedical Magnetic Resonance, University of Tübingen, 72074 Tübingen, Germany

⁵Laboratory of Molecular and Cellular Neuroimaging, International Center for Primate Brain Research (ICPBR), Center for Excellence in Brain Science and Intelligence Technology (CEBSIT), Chinese Academy of Sciences (CAS), Shanghai 200031, People's Republic of China

^{a)}Author to whom correspondence should be addressed: kai.buckenmaier@tuebingen.mpg.de

ABSTRACT

The efficacy in ^1H Overhauser dynamic nuclear polarization in liquids at ultralow magnetic field (ULF, $B_0 = 92 \pm 0.8 \mu\text{T}$) and polarization field ($B_p = 1\text{--}10 \text{ mT}$) was studied for a broad variety of 26 different spin probes. Among others, piperidine, pyrrolidine, and pyrroline radicals specifically synthesized for this study, along with some well-established commercially available nitroxides, were investigated. Isotope-substituted variants, some sterically shielded reduction-resistant nitroxides, and some biradicals were included in the measurements. The maximal achievable enhancement, E_{max} , and the radio frequency power, $P_{1/2}$, needed for reaching $E_{\text{max}}/2$ were measured. Physico-chemical features such as molecular weight, spectral linewidth, heterocyclic structure, different types of substituents, deuteration, and ^{15}N -labeling as well as the difference between monoradicals and biradicals were investigated. For the unmodified nitroxide radicals, the E_{max} values correlate with the molecular weight. The $P_{1/2}$ values correlate with the spectral linewidth and are additionally influenced by the type of substituents neighboring the nitroxide group. The nitroxide biradicals with high intramolecular spin-spin coupling show low performance. Nitroxides enriched with ^{15}N and/or ^2H afford significantly higher $|E_{\text{max}}|$ and require lower power to do so, compared to their unmodified counterparts containing at natural abundance predominantly ^{14}N and ^1H . The results allow for a correlation of chemical features with physical hyperpolarization-related properties and indicate that small nitroxides with narrow spectral lines have clear advantages for the use in Overhauser dynamic nuclear polarization experiments. Perdeuteration and ^{15}N -labeling can be used to additionally boost the spin probe performance.

© 2021 Author(s). All article content, except where otherwise noted, is licensed under a Creative Commons Attribution (CC BY) license (<http://creativecommons.org/licenses/by/4.0/>). <https://doi.org/10.1063/5.0064342>

INTRODUCTION

^1H Overhauser dynamic nuclear polarization (ODNP) is a hyperpolarization method that transfers the higher electron spin polarization to target proton spins.¹ In contrast to other common dynamic nuclear polarization (DNP) mechanisms (solid effect, cross

effect, and thermal mixing), the classical Overhauser effect allows for the hyperpolarization of liquids.² In recent years, there has been a renaissance in terms of ODNP.² While it was also shown that ODNP works at high magnetic field strengths ($>1 \text{ T}$),^{3,4} the main reason for the growing interest in this method was the construction of novel low-field ($<0.5 \text{ T}$) and ultralow-field (ULF, $<10 \text{ mT}$) MRI

scanners.^{5–7} In this field range, the radio frequency (RF) needed for transferring spin order from electrons to protons via ODNP¹ lies in the 100 MHz range. Thus, a sufficient penetration depth for larger samples is enabled, making *in vivo* hyperpolarization experiments with small animals possible. The continuous *in vivo* hyperpolarization is one of the main advantages of ODNP over other techniques such as parahydrogen-based hyperpolarization, where the hyperpolarization process takes place outside of the subject.⁸ It led to the development of *in vivo* Overhauser MRI (OMRI). Several groups already performed OMRI experiments on animals using trityl radicals^{9,10} or nitroxides such as carboxy-PROXYL (PCA)¹¹ and TEMPO¹² in mM concentrations.

Several trityl radicals show no hyperfine splitting of the electron energy levels, and the toxicity of some hydrophilic derivatives, e.g., Oxo63, is sufficiently low.¹³ However, they are difficult to synthesize or to obtain commercially. Nitroxides, e.g., TEMPO or PCA, are easily available, but the magnitude of the maximal enhancement is lower than that of trityl free radicals because of hyperfine splitting.¹⁴ For more than half a century, nitroxides have been exploited as spin probes and spin labels in biophysics and biomedical research. Specific spin probes have been designed for imaging of extracellular pH,¹⁵ thiols,¹⁶ and enzymatic activities.¹⁷ The unique redox properties of nitroxides make them a useful tool for the investigation of oxidative stress.^{11,18} Unlike large trityls, small-sized nitroxides show a high ability to permeate cells, tissues, and even the blood–brain-barrier, thus enabling brain imaging.^{19–22}

Those kinds of small-size free radical molecules or spin probes are being investigated in respect to their ODNP properties since Hauser and Stehlik discovered the ODNP effect in liquids.²³ Not only the enhancement of the proton magnetic resonance (MR) signal was reported but also other nuclei, such as ²H, ¹³C, or ¹⁹F, could be hyperpolarized.²⁴ For OMRI, so far only ¹H *in vivo* hyperpolarization was implemented.

The main drawbacks of nitroxides as free radical probes for *in vivo* applications are their fast chemical reduction to diamagnetic compounds by biogenic reductants and/or their rapid excretion.^{25,26} There are several general pathways to address the problem. Small spin probes can be incorporated into different macromolecular or supramolecular structures, which can prevent rapid reduction and clearance. Unfolded proteins, polyelectrolytes, polymers, surface lipid vesicles, and folded globular proteins have been already investigated.^{27–32} The attached nitroxide produces ODNP enhancement within 10 Å distance.^{28,29} Depending on the macromolecule, the magnitude of the enhancement can be reduced by a limited access of the solvent to the radical and by an increase in rotational correlation time. Thus, polymeric structures that reduce solvent accessibility and radical mobility can only be efficient as delivery systems (targeted or not), releasing small spin probes spontaneously or in response to certain biochemical processes, e.g., receptor interaction. Some examples of free nitroxide release from spin-labeled biopolymers have been published.^{33,34} Experiments with spin probes attached to different heparins or tobacco mosaic viruses have been performed. Solvent accessibility and radical mobility seem sufficient in these experiments, and they provide promising candidates for *in vivo* studies.^{35,36} While toxicity varies strongly for different spin probes,^{13,36–38} the inclusion of spin probes into macromolecules could additionally render this problem negligible. As an alternative, sterically shielded nitroxides, such as tetraethyl-substituted

nitroxides, with a higher resistance to bioreduction can be used.^{39,40} To retard excretion, the nitroxides can be designed to permeate or even accumulate in tissues, living cells, or cellular compartments.^{22,41}

While multiple radicals have been investigated in previous studies,^{24,42–49} a lot of promising nitroxide spin probes have never been examined in regard to their ODNP suitability.

The main goal of this work is to investigate nitroxide radicals with different chemical properties in order to compare their ODNP related characteristics. This may give insight into the underlying physical mechanisms in order to provide a foundation for future spin probe design.

All of the presented substances are stable in aqueous buffered solution. While biocompatibility, toxicity, and stability are equally important for biological and medical applications, we do not regard these features here since it is possible to manipulate these biological properties by inclusion of the spin probes in macromolecular structures. Instead, the focus of the study lies on their physical suitability for ODNP and how changes in the chemical structure affect ODNP related properties.

FINDING THE OPTIMAL FREE RADICAL

When assessing different free radicals in respect to their suitability for ODNP applications, the most crucial physical property is their ability to transfer electron spin polarization to the target nuclear spins, thus hyperpolarizing the sample.

The enhancement factor $E = \langle I \rangle / I_0$, comparing the hyperpolarized signal $\langle I \rangle$ to the non-hyperpolarized signal I_0 , is one of the most important parameters. The achievable enhancement depends among others on the magnetic polarization field B_p , power of the RF-pulse P , hyperpolarization buildup time T_{HP} , and radical concentration.¹⁴ These dependencies are specific for each type of free radical.

In practice, in particular for *in vivo* applications, additional limitations to RF-power P , T_{HP} , and spin probe concentration apply. The optimal free radical exhibits a high magnitude of enhancement $|E(P)|$ at low RF-power P and a short T_{HP} . The two most fitting parameters for an easily comprehensible comparison of spin probe performance and suitability are E_{\max} and $P_{1/2}$. While E_{\max} states the maximal enhancement achievable with a certain spin probe, $P_{1/2}$ as the RF-power needed to reach half of E_{\max} expresses how easily the maximal enhancement is reached.

THEORETICAL CONSIDERATIONS

The efficiency of the local polarization transfer is characterized by the coupling factor ξ , which is independent of spin probe concentration and RF-power P . It is specific for each type of free radical spin probe and is defined as⁵⁰

$$\xi = \frac{1 - E(P)}{s(P) \times f \times \left| \frac{\omega_e}{\omega_H} \right|}, \quad (1)$$

with the electron and proton Larmor frequencies ω_e and ω_H . The leakage factor

$$f = 1 - \frac{T_{1,Bp}}{T_{1,0,Bp}} \quad (2)$$

describes how the dipolar relaxation mechanisms at B_p affect the relaxation time $T_{1,Bp}$ of the sample, compared to $T_{1,0,Bp}$ in a sample without free radical spin probes.

The electron spin resonance (ESR) saturation factor $s(P)$ describes how well the electron spin transition is saturated for the specific sample,

$$s(P) = \frac{P \times s_{\max}}{P_{1/2} + P} \quad (3)$$

The maximal saturation s_{\max} depends on the spin probe concentration and has a maximum value of $\frac{1}{3} \leq s_{\max} \leq 1$ for ^{14}N or $\frac{1}{2} \leq s_{\max} \leq 1$ for ^{15}N nitroxides.⁵⁰⁻⁵² $P_{1/2}$ defines the RF-power P needed to reach half of the maximal saturation s_{\max} , and it is inversely proportional to the longitudinal and transversal electron spin relaxation time.^{53,54} At the limit of $P \rightarrow \infty$, Eq. (1) determines the maximal enhancement E_{\max} for a given sample as

$$\lim_{P \rightarrow \infty} E(P) \equiv E_{\max} = 1 - \xi \times f \times \left| \frac{\omega_e}{\omega_H} \right| \times s_{\max}. \quad (4)$$

Inserting Eq. (3) into Eq. (1) and substituting s_{\max} via Eq. (4) yield an expression for the power dependent enhancement factor,

$$E(P) = \frac{(E_{\max} - 1) \times P}{P_{1/2} + P} + 1. \quad (5)$$

For OMRI applications, spin probes with a combination of high $|E_{\max}|$ and low $P_{1/2}$ are desirable.

Saturation and linewidth

The saturation of the ESR transition is crucial for the effective transfer of spin polarization. A RF-field is used to increase the population of higher energy states of the coupled spin system. For nitroxides, we find additional hyperfine splitting, originating from the interaction of the electron spin with the nitrogen nuclear spin.^{14,44,55} In a continuous wave (cw)-Overhauser experiment with nitroxide radicals, there are one resonant and one or two non-resonant electron transitions, depending on the nitrogen isotope. Intermolecular or intramolecular interactions of the electron spin with other electron or nuclear spins can lead to a mixing of the resonant and non-resonant energy levels and/or broadening of the spectral lines. Therefore, these interactions also have an influence on s_{\max} .^{50,52} This mixing and broadening can increase s_{\max} at the cost of a higher $P_{1/2}$.

Heisenberg exchange

Heisenberg spin exchange occurs when two nitroxide radical molecules with opposing spins collide and exchange spin polarization. This will lead to a mixing of the respective hyperfine states. Molecular collision rates increase with radical concentration. Heisenberg exchange leads to a broadening of ESR lines. According to Armstrong and Han, the effect is significant above 0.5 mM and the broadening effect is dominant above 3 mM radical concentrations.^{52,55}

Unresolved hyperfine splitting

In a nitroxide radical molecule, hyperfine splitting of the electron energy levels occurs not only due to interactions with the

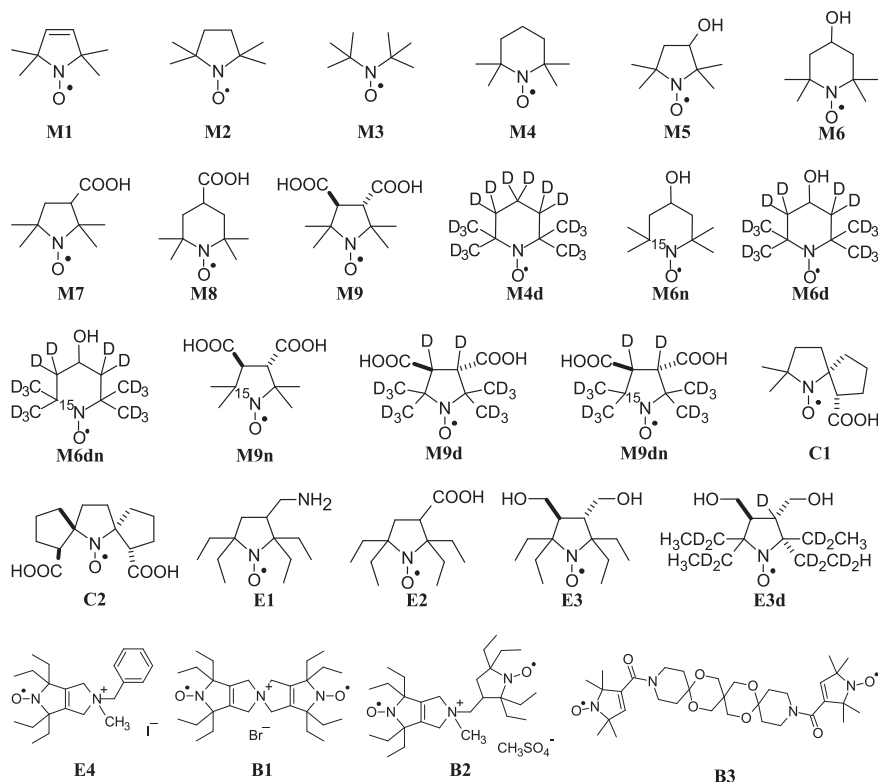


FIG. 1. Chemical structure of the radicals used in this study. The [supplementary material](#) provides more information on each specific compound and their synthesis.

nitrogen spin. Coupling to other spins within the molecule (generally proton spins) adds additional hyperfine lines. If the energy difference of the additional hyperfine structure is smaller than the ESR linewidth, it is unresolved in the spectrum and can lead to inhomogeneous broadening of the linewidth.^{56,57}

Tumbling and translational diffusion

The tumbling rate of the molecules in solution affects the spin-spin interactions. In a rapidly tumbling regime, molecular motion averages anisotropic interactions and only isotropic contributions are relevant, thereby affecting the ESR linewidth. If spin probes are immobilized (e.g., by inclusion into a macromolecule), the reduced tumbling rate leads to a line broadening in the ESR spectrum. Tumbling and translational diffusion also affect the interaction rate of free radicals with target protons, which has an effect on E_{\max} .^{47,50,58}

RESULTS AND DISCUSSION

Figure 1 shows the chemical structure of the measured spin probes. Besides commercially available tetramethyl-substituted nitroxides (M4, M6–M8), which are well established in many ODNP related publications^{12,43,46,47} and provide a point of

reference for other compounds, we also tested some bioreduction resistant, tetraethyl-substituted nitroxides (E1–E4). Other compounds such as M1–M5 look promising due to their small size (e.g., tumbling rate and permeability). Substitution of one or both geminal methyls of M2 with cyclic structures (C1, C2) provides a comparison to all other compounds with non-cyclic alkyl substituents. 3,4-Dicarboxy-proxyl (M9) is a product of intracellular hydrolysis of corresponding acetoxymethyl esters, which are well-known brain-targeted probes.⁵⁹ Deuterated and ¹⁵N-labeled versions of some of these compounds (M4, M6, M9, E3) also provide promising results. Finally, some biradicals (B1–B3) are added to the list of investigated spin probes.

Table I lists the investigated spin probes and their measured ODNP properties. The spin probes were dissolved in PBS (Phosphate Buffered Saline), and the pH was adjusted to 7.3. For TEMPO (M4), a 2 mM concentration leads to the highest $|E_{\max}|$ at a moderate power level P .¹² In this range, the radical concentration is large enough for an efficient polarization transfer, without exhibiting a dominant Heisenberg exchange rate, which would increase $P_{1/2}$. For good comparability, the same radical concentration of 2 mM was used for all compounds, leading to a 1 mM molecular concentration for biradicals and 2 mM for monoradicals.

The transition with the lowest frequency, which is equivalent to the peak with the lowest B_p in the ODNP spectrum (where

TABLE I. Spin probe properties and characterization results. For their chemical structures, refer to Fig. 1.

	$B_{p,RF}$ (mT)	f	$P_{1/2}$ (W)	E_{\max}	$\xi \cdot S_{\max}$	$FWHM$ (μ T)	MW (g/mol)
M1	2.27	0.81 ±0.01	5.9 ±0.2	-102.6 ±9.8	0.194 ±0.018	54.0 ±0.6	140.2
M2	2.27	0.73 ±0.01	4.7 ±0.2	-107.9 ±4.9	0.225 ±0.010	44.7 ±0.5	142.2
M3	2.14	0.78 ±0.01	3.8 ±0.2	-108.4 ±6.8	0.214 ±0.014	39.9 ±0.6	144.2
M4	2.12	0.73 ±0.01	6.1 ±0.3	-101.9 ±3.5	0.213 ±0.008	55.1 ±0.6	156.3
M5	2.30	0.82 ±0.01	4.8 ±0.2	-89.5 ±7.4	0.168 ±0.014	47.0 ±0.5	158.2
M6	2.15	0.74 ±0.01	7.1 ±0.3	-91.1 ±4.7	0.187 ±0.010	61.9 ±0.9	172.2
M7	2.28	0.74 ±0.01	5.3 ±0.2	-88.1 ±3.8	0.182 ±0.008	50.6 ±0.6	185.2
M8	2.14	0.75 ±0.01	6.1 ±0.3	-78.3 ±4.8	0.160 ±0.010	60.1 ±1.0	200.3
M9	2.30	0.71 ±0.02	4.3 ±0.2	-68.5 ±2.9	0.148 ±0.007	48.6 ±1.1	228.2
M4d	2.13	0.74 ±0.02	4.6 ±0.2	-118.2 ±5.4	0.245 ±0.013	43.6 ±0.5	174.4
M6n	2.64	0.74 ±0.02	5.5 ±0.2	-109.1 ±8.1	0.226 ±0.017	58.5 ±0.8	173.2
M6d	2.15	0.74 ±0.02	4.2 ±0.2	-105.2 ±2.7	0.219 ±0.007	40.6 ±0.4	188.3
M6dn	2.64	0.70 ±0.02	3.7 ±0.2	-126.2 ±5.6	0.275 ±0.014	38.6 ±0.4	189.3
M9n	2.75	0.75 ±0.01	3.1 ±0.2	-89.4 ±4.6	0.183 ±0.009	47.5 ±2.3	229.2
M9d	2.29	0.74 ±0.01	2.8 ±0.1	-79.2 ±5.9	0.164 ±0.012	36.7 ±5.9	242.3
M9dn	2.74	0.65 ±0.01	1.1 ±0.1	-79.6 ±1.5	0.188 ±0.004	37.3 ±0.9	243.3
E1	2.40	0.71 ±0.02	9.2 ±0.6	-63.8 ±2.4	0.138 ±0.006	117.2 ±11.0	228.4
E2	2.37	0.77 ±0.01	7.8 ±0.5	-62.6 ±2.3	0.126 ±0.005	104.3 ±4.8	241.3
E3	2.42	0.76 ±0.02	10.4 ±0.9	-54.4 ±3.0	0.110 ±0.007	130.1 ±10.1	258.4
E3d	2.42	0.83 ±0.01	8.9 ±0.5	-64.1 ±3.4	0.119 ±0.006	75.7 ±1.4	269.4
E4	2.36	0.74 ±0.01	6.2 ±0.3	-74.9 ±3.1	0.155 ±0.007	62.1 ±2.8	342.5
C1	2.30	0.70 ±0.01	4.8 ±0.3	-70.8 ±6.2	0.155 ±0.014	74.1 ±4.7	212.3
C2	2.39	0.81 ±0.01	7.8 ±0.5	-54.0 ±5.4	0.104 ±0.010	94.0 ±2.4	280.3
B1	3.66	0.69 ±0.11	60.5 ±29.8	-24.4 ±10.0	0.056 ±0.024	>700 ... ^a	458.7
B2	3.22	0.76 ±0.07	96.7 ±80.7	-29.8 ±22.1	0.061 ±0.044	>500 ... ^a	462.7
B3	2.29	0.70 ±0.03	16.5 ±0.90	-56.0 ±2.6	0.124 ±0.008	76.5 ±1.8	630.8

^aDue to strong inhomogeneous line broadening, the fit model did not converge for these compounds. Only a lower bound for $FWHM$ could be estimated, and no standard error could be derived from the fit.

the ESR-frequency is held constant), was used for all characterizations. According to Guiberteau and Grucker,¹⁴ this line exhibits the highest $|E_{\max}|$.

The measured parameters characterizing the ODNP efficiency of the spin probes are E_{\max} and $P_{1/2}$ [see Eq. (5)]. Additional measurements of the longitudinal relaxation times $T_{1,Bp}$ and $T_{1,0,Bp}$ enable to separate the contribution of the leakage factor f on E_{\max} and the product of the coupling constant ξ and the maximal saturation factor s_{\max} . The influence on $T_{1,Bp}$ at 2 mM concentration was similar for all measured spin probes, leading to leakage factors f between 0.65 and 0.82.

By inserting f into Eq. (4), the product $\xi \cdot s_{\max}$ can be calculated. In order to determine ξ , the spin probe concentration can be varied and fitted to theoretical models.^{50,51} Pulsed electron–electron double resonance (ELDOR) experiments can be performed,⁶⁰ or one can approximate $s_{\max} \approx 1$ for very high spin probe concentrations or tethered nitroxides.⁵² We only determined the product of $\xi \cdot s_{\max}$, partially due to physical constraints such as the maximal RF-power and the limited amount of free radical compounds available to us, but mostly because we are more interested in a qualitative comparison of the compounds at the mentioned concentration.

Perdeuterated ¹⁵N-labeled nitroxides showed the best results, exhibiting high $|E_{\max}|$ at moderate RF-power; compound **M9dn**, a perdeuterated and ¹⁵N-labeled version of 3,4-dicarboxy proxyl (**M9**), showed the lowest $P_{1/2}$, while **M6dn**, a deuterated and ¹⁵N-labeled version of 4-hydroxy-TEMPO (**M6**), showed the highest $|E_{\max}|$ ($E_{\max} = -126.2$) of the measured compounds. Of the unmodified nitroxides, di-tert-butyl (**M3**) showed the lowest $P_{1/2}$ and **M2** exhibited the highest $|E_{\max}|$. Generally, smaller (lower molecular weight) molecules seemed to perform better, most likely because of a faster tumbling rate and translational diffusion.

Since they offer the possibility of increasing radical concentration without changing the molecular concentration, we also investigated several biradicals. The biradicals with high enough spin–spin coupling of the electrons showed significant line broadening in the ODNP spectrum. More RF-power is needed to saturate the ESR transitions, and $P_{1/2}$ is increased significantly [see Fig. 2(a)].

Comparing the maximal enhancement of the different compounds, it becomes clear why TEMPO (**M4**) and PCA (**M7**) are commonly used materials for ODNP experiments. While TEMPO, often used for *in vitro* experiments, exhibits a relatively high $|E_{\max}|$ of 101.9, PCA has a lower $|E_{\max}|$, but with a lower $P_{1/2}$ of 5.3 W, and is thus better suited for low power applications such as *in vivo* experiments.

In the following, we discuss in detail the various factors that influence the most important physical properties of nitroxides as spin probes in ODNP applications.

Molecular weight (*MW*)

Figure 2(b) shows a trend for the monoradicals (dark blue and red data points), correlating E_{\max} and the *MW*, where molecules with higher *MW* have lower $|E_{\max}|$ values. For this evaluation, the *MW* of the ionic form is used for all compounds that exist protonated or unprotonated in the buffered solution at pH = 7.3 to improve comparability. Special cases such as biradicals, isotope-enriched derivatives, or an unsaturated bicyclic compound can deviate from the trend.

The correlation of E_{\max} with the molecular weight is consistent with the theoretical considerations of the local dynamics of the radicals in solution.^{50,58} Translational diffusion of the molecules is influenced by the *MW*. Lower weight leads to faster diffusion, increasing ξ and $|E_{\max}|$.⁴⁷

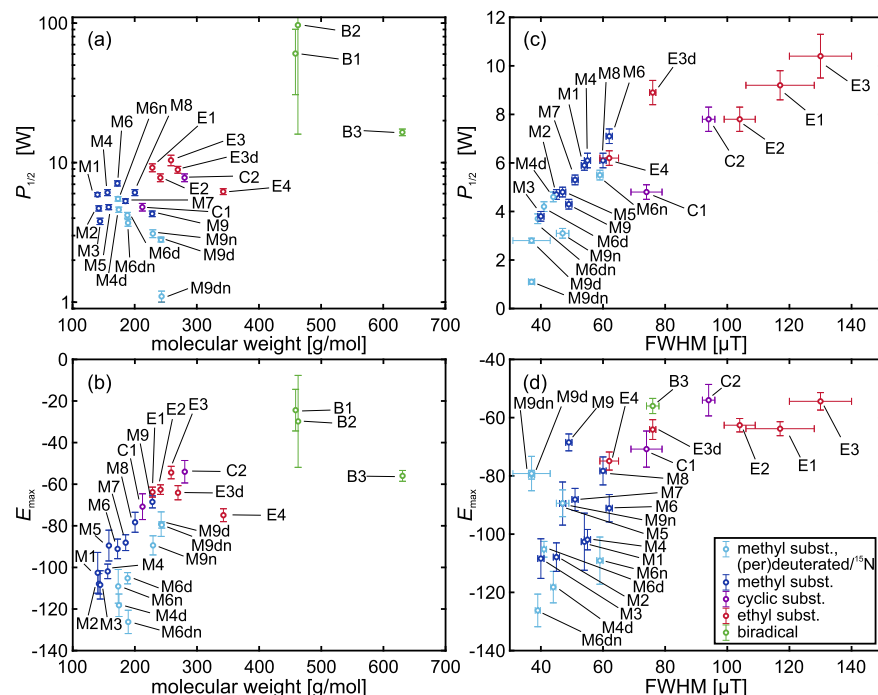


FIG. 2. Efficiency of the different groups of spin probes: (a) $P_{1/2}$ vs molecular weight (*MW*), (b) E_{\max} vs *MW*, (c) $P_{1/2}$ vs *FWHM*, and (d) E_{\max} vs *FWHM*, measured at the first peak of the ODNP spectrum. For assignment and structures of the compounds, refer to Fig. 1.

In contrast, Fig. 2(a) indicates no clear correlation between the MW and $P_{1/2}$. Whether this correlation is not existing or just superimposed by other effects cannot be determined from the data obtained.

Linewidth ($FWHM$) of the ODNP spectrum

The $P_{1/2}$ values of the monoradicals (with the exception of **C1**, which will be discussed below) show a clear correlation with the linewidth ($FWHM$) of the ODNP spectrum [see Fig. 2(c)]. In accordance with the theoretical considerations above, a broadened linewidth $FWHM$ lowers s_{\max} and increases $P_{1/2}$, independent of the underlying cause. The biradicals are not included in Fig. 2(c) and are discussed separately below.

The effects defining the ESR linewidth are influencing the ODNP linewidth in a similar manner.^{14,61} The lower boundary of the measured $FWHM$ is additionally limited by the finite homogeneity of the polarizing field. **M9d** and **M9dn** may provide examples of this limit in Fig. 2(c).

Previously, it was shown that the linewidth and the number of electron spin resonance lines of the nitroxides are influencing E_{\max} .⁶² Figure 2(d) indicates that $FWHM$ is dependent on multiple influences. As described in the theoretical section “Tumbling and translational diffusion”, the tumbling rate of the molecule affects E_{\max} as well as the linewidth. Other effects, such as inhomogeneous broadening due to intramolecular spin coupling, seem to affect $FWHM$ much more than E_{\max} . Compounds **E1**, **E2**, **E3**, and **E3d** provide good examples for this effect, showing a small variance of E_{\max} , but a broad range of $FWHM$.

Neighboring substituents to the nitroxide group

Pyrrolidines with two geminal ethyl groups at positions 2 or 5 of the heterocycle are known to show high hyperfine coupling (~ 0.2 mT) with the methylene hydrogens of these groups in their X-band ESR spectra. In low-field ESR or ODNP, this coupling is not resolved and a strong line broadening is observed in the literature and in our measurements.^{63,64} Due to the repulsion of geminal ethyl groups with a substituent in the neighboring position (positions 3 or 4) of the ring, less averaging occurs, leading to more pronounced broadening. Comparing **E1–E3**, this broadening seems to be influenced by the type and number of substituents at positions 3 and 4. However, this influence needs further investigation.

The influence of the geminal substituents becomes especially apparent when comparing similar compounds, where only the geminal methyls and ethyls are exchanged. This is shown in the ODNP spectra of Fig. 3. Here, the $FWHM$ of **E2** ($FWHM_{\text{left peak}} = 104 \pm 5 \mu\text{T}$) is more than twice when compared to the methyl group counterpart **M7** ($FWHM_{\text{left peak}} = 51 \pm 1 \mu\text{T}$).

For monoradicals, the data in Figs. 2(a) and 2(c) show a correlation of the type of substituent next to the nitroxide group with $P_{1/2}$. In general, compounds with methyl substituents (**M1–M9**) exhibit lower $P_{1/2}$ than the compounds **E1–E3** with ethyl substituents. Only **E4** ($P_{1/2} = 6.2$ W) has a lower $P_{1/2}$ than **M6** ($P_{1/2} = 7.1$ W).

In Figs. 2(c) and 2(d), the results for **E3d** and **E4** further illustrate the unresolved coupling caused by the geminal ethyl substituents. As will be discussed below, deuterium has less hyperfine coupling than standard methylene hydrogens.⁵⁷ Radical **E4** is based on a 1,2,3,4,5,6-hexahydrocyclopenta[c]pyrrole ring system

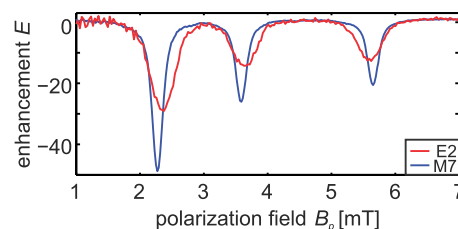


FIG. 3. Influence of neighboring substituents: ODNP spectra of **E2** and **M7**. The compound with ethyl group neighbors to the radical shows a line broadening over their methyl group counterpart. The difference in peak amplitude within one spectrum results from the polarization field dependency of the enhancement, as previously described by Guiberteau and Grucker.¹⁴

with a nearly planar geometry, where averaging of ethyl group conformations can occur and therefore no large couplings are observed. As a result, **E3d** and **E4** show much narrower lines and E_{\max} and $P_{1/2}$ are improved in comparison to other tetraethyl compounds. A similar spectral peculiarity was earlier reported for sterically shielded imidazolidine nitroxides.⁶³ The nitroxide **C1** has a methyl substituent on one side and a spiro-2-(carboxy)cyclopentane moiety on the other side of the nitroxide group. $P_{1/2} = 4.8$ W of **C1** fits into the methyl substituent group and could not be expected for a nitroxide with relatively broad lines. The deviating behavior of **C1** might be related to relaxation, to fast proton exchange by the carboxy group near the radical, or to the remaining geminal methyl group. However, the dispirocyclic nitroxide dicarboxylic acid **C2** did not show any deviation from the general trend, and its ODNP characteristics are similar to those of the tetraethyl compounds. The observed phenomenon deserves further investigation.

Compared to tetramethyl analogs, the four ethyl groups adjacent to the N–O moiety could increase the distance of approach between the free radical electron spin and the targeted protons of water. This would affect the coupling constant ξ and in turn lower $|E_{\max}|$. The influence of bulky substituents upon the accessibility of the nitroxide group has been studied previously.^{39,65,66} These studies showed lower solvent accessible surface areas and a higher volume steric shielding parameter (V_{ss}) for sterically shielded nitroxides. However, there is no evidence that sterical hindrance affects the access of small molecules, such as water, to nitroxide oxygen. Solvation with water implies an interaction of the polar nitroxide moiety with water protons. The interaction efficacy of sterically hindered nitroxides with water was already demonstrated by the similarity of T_1 -relaxivities for organic radical contrast agents based on sterically shielded and tetramethyl-substituted nitroxides.⁶⁷ In our study, the sets of $|E_{\max}|$ data points for tetramethyl- and tetraethyl-substituted nitroxides exhibit a smooth transition, and the observed changes in $|E_{\max}|$ are sufficiently explained by the influence of MW . An effect through a change of accessibility/distance of approach is not observed.

Heterocyclic ring structure

Comparing the pyrrolidine and piperidine based tetramethyl compounds (Fig. 2), the ring structure does not seem to significantly affect E_{\max} . If the ring structure has an influence on E_{\max} , it is not visible in the data since the correlation of E_{\max} with the molecular weight remains the dominating factor.

TABLE II. Improvement of ODNP properties of the ^{15}N -labeled and/or (per)deuterated compounds. The improvement is displayed as a change compared to their conventional counterparts in percent.

Improvement:	$FWHM$ (%)	$P_{1/2}$ (%)	$ E_{\max} $ (%)
M4d	-21	-24	16
M6n	-6	-22	20
M6d	-34	-41	16
M6dn	-38	-48	39
M9n	-2	-28	31
M9d	-25	-36	16
M9dn	-23	-74	16
E3d	-42	-15	18

However, there is a difference in $P_{1/2}$. The unmodified tetraethyl pyrrolidines exhibit $P_{1/2} \leq 5.3$ W and $FWHM \leq 51$ μT , while the structurally similar piperidines all have $P_{1/2} \geq 6.1$ W and $FWHM \geq 55$ μT . Similarly, $P_{1/2} \leq 3.1$ W was observed for all perdeuterated and/or ^{15}N -labeled pyrrolidines and $P_{1/2} \geq 3.5$ W was observed for all perdeuterated and/or ^{15}N -labeled piperidines.

This effect could be explained by an increase in intramolecular interaction within piperidines, which could be caused by an increase in the number of atoms per molecule or by a change of conformational flexibility of the ring. As discussed in the theoretical considerations on saturation and linewidth, any effect that leads to a broadening of lines in the ODNP spectrum will also increase $P_{1/2}$.

(Per)deuteration and ^{15}N -labeling

We measured multiple (per)deuterated and/or ^{15}N -labeled variants of DCP (**M9**) and of TEMPOL (**M6**), marked with “d” and/or “n,” respectively. Additionally, we measured a perdeuterated TEMPO **M4** (**M4d**) and a partially deuterated tetraethyl compound **E3** (**E3d**).

Both variations as well as their combination show a positive effect on the performance of the compound compared to their unmodified counterparts (see [Table II](#)).

All deuterated nitroxides show lower $FWHM$ and $P_{1/2}$ as well as higher $|E_{\max}|$ than their corresponding non-deuterated analogs despite the latter having smaller molecular weights.

In nitroxide radicals, the hyperfine splitting caused by the interaction of the free electron with the nitrogen atom depends on the nitrogen isotope. The six energy levels of the naturally abundant ^{14}N nitroxide radicals are reduced to four levels in ^{15}N -labeled

nitroxides.^{14,61} Therefore, ^{15}N -labeled nitroxide radicals exhibit two ESR lines, while samples with unmodified nitroxides (predominantly ^{14}N) have three ESR lines. This leads to an increased theoretical s_{\max} and therefore improved E_{\max} for ^{15}N -labeled nitroxides, compared to their unmodified versions. Additionally, a reduced number of hyperfine states reduces the amount of mixing between them, thus resulting in narrower lines and an improved $P_{1/2}$ for the ^{15}N -labeled compounds. Furthermore, ^{15}N -labeled nitroxide radicals have longer electron relaxation times than the corresponding unlabeled counterparts,⁶⁸ which also reduces $P_{1/2}$.⁶⁹

The positive effect of (per)deuteration on $P_{1/2}$ is a result of the reduced intramolecular coupling. Deuterium has lower hyperfine coupling than hydrogen, reducing the unresolved hyperfine splitting, which in consequence narrows the ESR linewidth and improves $P_{1/2}$.⁵⁷

Interestingly, the magnitude of the improvement by deuteration or ^{15}N -labeling on E_{\max} and $P_{1/2}$ differs greatly between the different nitroxides and no clear pattern could be determined. Still, deuteration and ^{15}N -labeling of sterically shielded nitroxides certainly are promising ways to improve the ODNP properties of reduction-resistant probes for *in vivo* applications.

Monoradical vs biradical

Here, we compare a monoradical (**E4**) with two biradicals (**B1** and **B2**) of a similar molecular structure. In addition, we measured **B3**, which is a rigid biradical with a greater intramolecular distance between the two radical groups.

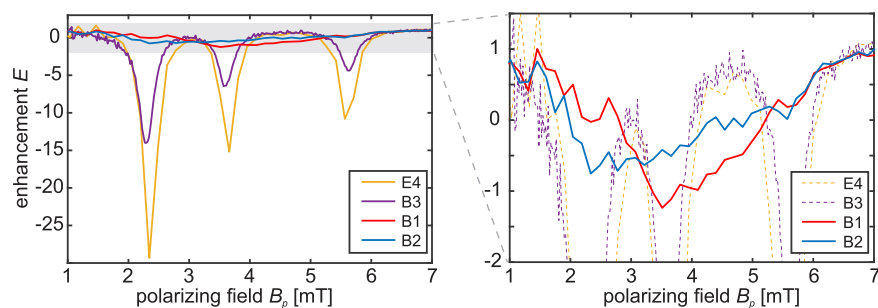
Since the compared compounds differ significantly in MW , any possible biradical-related effect on E_{\max} is likely concealed by the dominant correlation to the MW .

[Figure 4](#) depicts their respective ODNP spectra. While the monoradical **E4** shows a three-peak ODNP spectrum as expected and a $P_{1/2}$ below 7 W, the biradicals **B1** and **B2** show $P_{1/2}$ greater than 60 W (see [Table I](#)). The ODNP spectra of the latter two biradicals show an extreme broadening of the peaks to a degree that the three peaks are not clearly distinguishable anymore.

We attribute this effect to intramolecular electron spin-spin interactions of the radicals, which in turn leads to inhomogeneous broadening of the electron transitions.

In accordance with this, **B3** (biradical) shows a $P_{1/2}$ value of 16.5 W. It has a greater distance between the radicals within one molecule, leading to a weaker intramolecular electron spin-spin interaction and thus less broadening of the ODNP spectra.

In order to obtain a deeper understanding of the performance of biradicals in ODNP experiments, a more quantitative study of the

**FIG. 4.** Broadening for biradicals: ODNP spectra of monoradical **E4** and biradicals **B1**–**B3**. The three separate peaks, visible in the spectra of **E4** and **B3**, are not distinguishable for **B1** and **B2** due to strong line broadening. At finite RF-power, the broadening also significantly reduces $|E_{\max}|$.

magnetic hyperfine-, dipolar-, and g -tensors as well as the exchange interaction of the two unpaired electron spins would be necessary. Such a study was done for the rigid and narrow linewidth biradical TEMPO-bis-ketal, which showed comparable enhancement to monoradicals at 9.2 T.^{46,49}

Ionic compounds

The presented spin probes contain a range of compounds that are ionic in aqueous solution at pH 7.3, in particular compounds containing acid or amino groups and compounds **E4**, **B1**, and **B2** containing a quaternary ammonium group. One could expect a reduced Heisenberg exchange because of repulsion between the ionic nitroxides. Within our data, however, we cannot find a correlation of the ionic charge of a spin probe with their E_{\max} or $P_{1/2}$.

CONCLUSION

The goal of this work is to better understand the various factors that influence the physical properties of free radical spin probes. We investigated a broad range of 26 different nitroxides and their physico-chemical parameters to help in predicting and optimizing the suitability of free radical spin probes for *in vivo* ODNP applications.

For such applications, a high $|E_{\max}|$ by hyperpolarization is required. While a narrow ESR linewidth seems to facilitate a better E_{\max} , our data suggest that the molecular weight of the spin probe has the greatest impact on its maximal enhancement, indicating a correlation to the tumbling rate and translational diffusion of the spin probe. E_{\max} can be improved additionally by using deuterated and ¹⁵N-labeled derivatives of a chosen compound.

To avoid excessive sample or tissue heating, the transmitted RF-power will be limited in most applications. In such cases, a low $P_{1/2}$ ensures sufficient hyperpolarization. A narrow ESR linewidth correlates with low $P_{1/2}$ values and can be achieved by limiting intermolecular and intramolecular interactions. Therefore, strong spin-spin interactions in some biradicals can render them useless. Unresolved hyperfine splitting from geminal ethyl substituents next to the nitroxide group can negatively impact the ODNP performance of such sterically shielded nitroxides. Using ring systems with a more planar geometry seems to circumvent this problem but needs further investigation. Pyrrolidines with a five-membered heterocyclic structure showed better $P_{1/2}$ than six-membered piperidines, but this finding also needs further investigation. Deuteration and ¹⁵N-labeling of the compounds improved $FWHM$ and $P_{1/2}$ for all examples in our study and generally seem to be an effective way of boosting the ODNP-performance of nitroxide spin probes. However, depending on the specific case, a more complex synthesis may be a disadvantage of these modified compounds.

In a nutshell, the ideal nitroxide radical would be a light weight, deuterated ¹⁵N-pyrrolidine monoradical, with neighboring methyl substituents and a narrow linewidth ODNP spectrum.

However, further investigations are needed since we are not looking at the biological context at this stage. Any compound will have to compromise between stability, low molecular concentration, long retention, and low RF-power. While compounds with neighboring methyl groups would need less power for the same level of hyperpolarization, the ones with ethyl groups are expected to be

more stable and resistant against reduction in biological environments.⁷⁰ Small monoradicals are usually rapidly excreted, and thus, their short retention in blood might lower their suitability for *in vivo* ODNP applications. Nanosized delivery systems or the coupling of small radicals to nanosized structures might offer a solution to the problem and can help to protect the radicals against biological inactivation. When coupling multiple small spin probes to such nanosized structures, decoupling of the electron spin-spin interactions of the radicals within one molecule will help to prevent inhomogeneous broadening. Such incorporation in larger structures could also impact the tumbling and translational diffusion of the spin probes. This could lower $|E_{\max}|$ at a given RF-power P but could be mitigated by ensuring a flexible linker between the small radical and nanosized structure to allow for the unhindered movement of the small spin probe.

While technical challenges for ODNP applications differ for different magnetic fields, the coupling factor ξ also changes with the field.² This change is, however, gradual, and therefore, the presented results still provide a point of reference for spin probe selection and spin probe design for applications operating at fields above the ULF-regime.

Ultimately, our study can help to investigate the functionalization of free radicals by incorporation into macromolecules or carrier molecules. The chemical processes involved in such functionalization often require specific chemical features of the radical molecules. Our results provide a list of possible candidates and give a good starting point for these types of experiments.

EXPERIMENTAL SECTION

Syntheses

Compounds **M4** and **M6–M8** were purchased from MERCK. Nitroxides **M2**,⁷¹ **M3**,⁷² **M5**,⁷¹ **M4d**,⁷³ **M6n**,⁷⁴ **M6d**,⁷⁴ **M6nd**,⁷⁴ **M9**,¹⁶ **M9n**,¹⁶ **M9d**,¹⁶ **M9nd**,⁷⁵ **E2**,^{39,76} and **E3**⁶⁴ were prepared according to literature procedures. The synthesis of nitroxides **M1**, **E4**, and **B1–B3** is described in the [supplementary material](#). Preparation of compounds **C1**, **C2**, **E1**, and **E3d** will be published elsewhere. Analytical data for the in-house synthesized nitroxides are shown in the [supplementary material](#).

The solubility of the different nitroxides was not specifically measured but differed slightly during sample preparation. With pH adjustment and sometimes the use of an ultrasonic bath, all samples were soluble in 2 mM concentration at room temperature in PBS.

Hardware

All measurements were performed at the ULF-MRI setup previously described in Ref. 7. The superconducting quantum interference device (SQUID) based sensor is the heart of the system. In combination with a gradiometric pickup coil, the intrinsic noise level of this SQUID based magnetic field sensor lies in the femtoTesla range. The static magnetic field, generated by a tetracoil with a battery-driven current source, was set to $B_0 = 92 \pm 0.8 \mu\text{T}$ for all measurements presented here. The polarization field was generated by a Helmholtz coil with a diameter of 166 mm. The RF-signal for the ODNP excitation is transmitted by a resonator consisting of a single loop of a 1 mm thick copper wire with a diameter of 16.1 mm. It is tuned to $\omega_e = (120 \pm 1) \text{ MHz}$.

The whole setup is placed inside a multilayered magnetic- and RF-shielded chamber. All electrical lines needed for the experiments are fed through relays and/or pi-filters in order to suppress amplifier noise during acquisition of the MR signal.

The sample containers consist of modified microcentrifuge tubes and have a volume of 1.2 ml. The geometry was identical for all measurements to ensure comparability across samples. Larger sample volumes yielded a greater signal-to-noise ratio (SNR), but a limited RF-penetration depth leads to larger systematic errors. With the 1.2 ml samples, a relatively uniform saturation of the whole sample could be achieved.

Preparatory measurements

Ahead of specific characterization measurements, two preliminary measurements have to be performed.

First, the polarization field B_p has to be set to the optimal field strength, where the RF-coil frequency corresponds to the hyperfine splitting transition of the nitroxide radical.

In order to determine the appropriate value, the B_p field strength is varied, while all other parameters are fixed. For each B_p step, the nuclear magnetic resonance (NMR) spectrum is recorded via a simple free-induction decay (FID) sequence (see Fig. 5). The area under the peak of each NMR spectrum as a function of B_p is divided by the non-hyperpolarized area under the peak of the respective field strength, which forms an ODNP spectrum of the sample and shows the number of usable transitions from hyperfine splitting as well as the respective line shapes. Each peak is fitted with a Lorentzian function to determine the *FWHM* from the fit result.

Second, the duration of the hyperpolarization pulse has a critical impact on the sample polarization. By sweeping the polarization time t_{BP} , instead of B_p , and setting B_p to the previously determined optimum of the left ODNP peak, the hyperpolarization buildup time T_{HP} at the polarization field strength can be obtained, by fitting the area under the peak of the NMR spectra as a function of t_{BP} to an exponential buildup function.

For the further measurements, a compromise was made between low measurement durations and a high polarization level. Therefore, the hyperpolarization time t_{BP} is set to $t_{BP,90} = 2.3 \cdot T_{HP}$, where the sample reaches 90% of the maximum polarization.

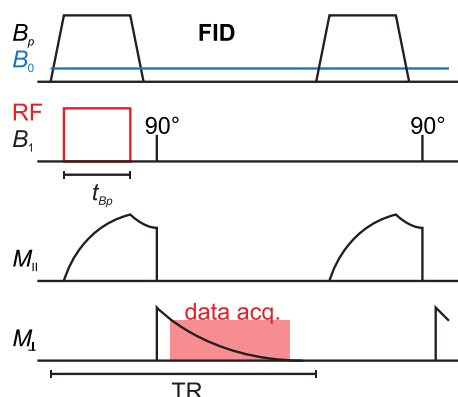


FIG. 5. Schematic representation of the sequences. For the various characterization steps, B_p , t_{BP} , and RF-power were varied.

Characterization measurements

In order to characterize a sample, the leakage factor f , the product of the coupling constant and the maximal saturation factor $\xi \cdot s_{\max}$, the maximal theoretically possible enhancement E_{\max} , and the power $P_{1/2}$ needed to reach $0.5 \cdot E_{\max}$ have to be determined.

The leakage factor f is determined from the longitudinal relaxation times $T_{1,BP}$ and $T_{1,0,BP}$ at the polarization field strength B_p according to Eq. (2).

In order to determine $\xi \cdot s_{\max}$, E_{\max} , and $P_{1/2}$, the power dependency of the enhancement factor has to be measured. This is done by varying the RF-power. The area under the peak of the NMR spectra can be fitted to a model following Eq. (5), which determines $E_{\max, \text{measured}}$ and $P_{1/2}$. Since we use the hyperpolarization time $t_{BP,90}$, the measured $E_{\max, \text{measured}}$ is scaled up to 100% saturation afterward. Inserting E_{\max} into Eq. (4) gives $\xi \cdot s_{\max}$.

All errors presented in Table I represent the statistical errors, determined from the respective fit results.

In Ref. 50, a measurement intensive method to correct for heating effects is presented, altering the theoretical description above. Our sample volumes are in the ml range. The samples are air stream cooled, and a long repetition time TR is used, in order to avoid heating effects and to reduce the systematic error. Therefore, we are not correcting for heating effects.

Precision of measurements

We present the characterization of ODNP properties for 26 different nitroxide radicals. The majority of these are novel and bespoke compounds, synthesized at NIOCH SB RAS for this very purpose. Only limited quantities of these substances were available for measurements at our ULF-MRI system.

We found a decrease in $P_{1/2}$ and an increase in relaxation times within 2 days of sample preparation (dissolving the radical compound in PBS) when repeating measurements of the same sample. This indicates a decrease in the spin probe concentration^{12,44} by degeneration, ruling out repeated measurements of the same samples. The presented samples were therefore prepared and characterized within a day. The degeneration was unexpected for these samples. We suppose that interactions of the radicals with the plastic composition of the modified microcentrifuge tubes as sample containers are the most likely reason. However, further investigation is needed to verify this claim.

The degeneration of samples introduces a systematic error, which depends on the compound's stability and the age of the sample. Since the radical stability is not the focus of this paper and other methods such as ESR are better suited for such tests, we used exemplary data from the commercially obtained compounds to estimate this error. The data suggested a change of $\leq 10\%$ of the measured parameters after 2 days and up to $\leq 25\%$ after 2 weeks of sample preparation.

To assess the precision, we used the commercially obtained compounds (radicals **M4**, **M6**, **M7**, and **M8**) to repeatedly prepare and measure samples of the same radicals for $n = 3$ times (see Table II of the supplementary material). The statistical errors (standard deviation) of those repeated measurements were between ± 2.1 and ± 13 for E_{\max} , ± 0.05 and ± 0.41 W for $P_{1/2}$, and ± 0.53 and ± 1.21 μT for *FWHM*.

SUPPLEMENTARY MATERIAL

The [supplementary material](#) provides a list of the measured samples, providing their chemical structure, their chemical name with common abbreviations (if applicable), and a reference for their synthesis or the source from where they were purchased. Additionally, it contains the dataset of the repeated measurements of commercially available compounds, from which the precision of the characterization measurements was determined. The [supplementary material](#) further describes the synthesis of samples **M1**, **E4**, **B1**, **B2**, and **B3** and contains infrared- and NMR-spectroscopy data of the synthesized samples and gas chromatography–mass spectrometry analyses of compounds **M1** and **M2**.

ACKNOWLEDGMENTS

The financial support of the ERA.Net RUS+ project (No. ST2017-382), NanoHyperRadicals (including RFBR 18-53-76003-ERA-A and BMBF, FKZ: Grant No. 01DJ18009), and the Shanghai Municipal Science and Technology Major Project (Grant No. 2019SHZDZX02) is acknowledged. The authors thank the Multi-Access Chemical Research Center SB RAS for spectral and analytical measurements of nitroxides ([supplementary material](#)). P.F. acknowledges the financial support from the Cusanuswerk e.V. The authors thank the DEAL project for promoting open access to research publications.

AUTHOR DECLARATIONS

Conflict of Interest

The authors have no conflicts to disclose.

DATA AVAILABILITY

The data that support the findings of this study are available within the article and its [supplementary material](#), as well as from the corresponding author upon reasonable request. Data on the chemical synthesis of the used compounds are available in the [supplementary material](#), as well as from I. A. Kirilyuk upon reasonable request.

REFERENCES

- 1 A. W. Overhauser, *Phys. Rev.* **92**, 411 (1953).
- 2 U. L. Günther, "Dynamic nuclear hyperpolarization in liquids," in *Modern NMR Methodology*, Topics in Current Chemistry Vol. 335, edited by H. Heise and S. Matthews (Springer, Berlin, Heidelberg, 2011), pp. 23–69.
- 3 T. Prisner, V. Denysenkov, and D. Sezer, *J. Magn. Reson.* **264**, 68 (2016).
- 4 M. Bennati and T. Orlando, *eMagRes* **8**, 11 (2019).
- 5 M. E. Halse and P. T. Callaghan, *J. Magn. Reson.* **195**, 162 (2008).
- 6 V. S. Zotev, T. Owens, A. N. Matlashov, I. M. Savukov, J. J. Gomez, and M. A. Espy, *J. Magn. Reson.* **207**, 78 (2010).
- 7 K. Buckenmaier, M. Rudolph, P. Fehling, T. Steffen, C. Back, R. Bernard, R. Pohmann, J. Bernarding, R. Kleiner, D. Koelle, M. Plaumann, and K. Scheffler, *Rev. Sci. Instrum.* **89**, 125103 (2018).
- 8 J. B. Hövener, A. N. Pravdivtsev, B. Kidd, C. R. Bowers, S. Glöggler, K. V. Kovtunov, M. Plaumann, R. Katz-Brull, K. Buckenmaier, A. Jerschow, F. Reineri, T. Theis, R. V. Shchepin, S. Wagner, P. Bhattacharya, N. M. Zacharias, and E. Y. Chekmenev, *Angew. Chem., Int. Ed.* **57**, 11140 (2018).
- 9 J. H. Ardenkjær-Larsen, I. Laursen, I. Leunbach, G. Ehnholm, L.-G. Wistrand, J. S. Petersson, and K. Golman, *J. Magn. Reson.* **133**, 1 (1998).
- 10 K. Golman, J. S. Petersson, J.-H. Ardenkjær-Larsen, I. Leunbach, L.-G. Wistrand, G. Ehnholm, and K. Liu, *J. Magn. Reson. Imaging* **12**, 929 (2000).
- 11 N. Kosem, T. Naganuma, K. Ichikawa, N. Phumala Morales, K. Yasukawa, F. Hyodo, K.-i. Yamada, and H. Utsumi, *Free Radical Biol. Med.* **53**, 328 (2012).
- 12 D. E. J. Waddington, M. Sarracanie, N. Salameh, F. Herisson, C. Ayata, and M. S. Rosen, *NMR Biomed.* **31**, e3896 (2018).
- 13 M. C. Krishna, S. English, K. Yamada, J. Yoo, R. Murugesan, N. Devasahayam, J. A. Cook, K. Golman, J. H. Ardenkjær-Larsen, S. Subramanian, and J. B. Mitchell, *Proc. Natl. Acad. Sci. U. S. A.* **99**, 2216 (2002).
- 14 T. Guiberteau and D. Grucker, *J. Magn. Reson., Ser. B* **110**, 47 (1996).
- 15 A. Samouilov, O. V. Efimova, A. A. Bobko, Z. Sun, S. Petryakov, T. D. Eubank, D. G. Trofimov, I. A. Kirilyuk, I. A. Grigor'ev, W. Takahashi, J. L. Zweier, and V. V. Khrantsov, *Anal. Chem.* **86**, 1045 (2014).
- 16 B. Epel, S. V. Sundramoorthy, M. Krzykawska-Serda, M. C. Maggio, M. Tseytlin, G. R. Eaton, S. S. Eaton, G. M. Rosen, J. P. Y. Kao, and H. J. Halpern, *J. Magn. Reson.* **276**, 31 (2017).
- 17 G. Audran, L. Bosco, P. Brémond, J.-M. Franconi, N. Koonjoo, S. R. A. Marque, P. Massot, P. Mellet, E. Parzy, and E. Thiaudière, *Angew. Chem.* **127**, 13577 (2015).
- 18 F. Hyodo, R. Murugesan, K.-i. Matsumoto, E. Hyodo, S. Subramanian, J. B. Mitchell, and M. C. Krishna, *J. Magn. Reson.* **190**, 105 (2008).
- 19 X. Wang, M. Emoto, Y. Miyake, K. Itto, S. Xu, H. Fujii, H. Hirata, and H. Arimoto, *Bioorg. Med. Chem. Lett.* **26**, 4947 (2016).
- 20 T. Manabe, A. Matsumura, K. Yokokawa, T. Saito, M. Fujikura, N. Iwahara, T. Matsushita, S. Suzuki, S. Hisahara, J. Kawamata, H. Suzuki, M. C. Emoto, H. G. Fujii, and S. Shimohama, *J. Alzheimer's Dis.* **67**, 1079 (2019).
- 21 M. C. Emoto, K. Sasaki, K. Maeda, H. G. Fujii, and S. Sato, *Chem. Pharm. Bull.* **66**, 887 (2018).
- 22 H. Sano, M. Naruse, K.-i. Matsumoto, T. Oi, and H. Utsumi, *Free Radical Biol. Med.* **28**, 959 (2000).
- 23 K. H. Hausser and D. Stehlik, *Adv. Magn. Opt. Reson.* **3**, 79 (1968).
- 24 W. Müller-Warmuth and K. Meise-Gresch, *Adv. Magn. Opt. Reson.* **11**, 1–45 (1983).
- 25 T. Niidome, R. Gokuden, K. Watanabe, T. Mori, T. Naganuma, H. Utsumi, K. Ichikawa, and Y. Katayama, *J. Biomater. Sci., Polym. Ed.* **25**, 1425 (2014).
- 26 G. Bačić, A. Pavićević, and F. Peyrot, *Redox Biol.* **8**, 226 (2016).
- 27 A. Pavlova, E. R. McCarney, D. W. Peterson, F. W. Dahlquist, J. Lew, and S. Han, *Phys. Chem. Chem. Phys.* **11**, 6833 (2009).
- 28 R. Kausik, A. Srivastava, P. A. Korevaar, G. Stucky, J. H. Waite, and S. Han, *Macromolecules* **42**, 7404 (2009).
- 29 J. H. Ortony, C.-Y. Cheng, J. M. Franck, R. Kausik, A. Pavlova, J. Hunt, and S. Han, *New J. Phys.* **13**, 015006 (2011).
- 30 B. D. Armstrong, J. Choi, C. López, D. A. Wesener, W. Hubbell, S. Cavagnero, and S. Han, *J. Am. Chem. Soc.* **133**, 5987 (2011).
- 31 R. Kausik and S. Han, *Phys. Chem. Chem. Phys.* **13**, 7732 (2011).
- 32 S. R. Burks, E. A. Legenzov, G. M. Rosen, and J. P. Y. Kao, *Drug Metab. Dispos.* **39**, 1961 (2011).
- 33 E. Parzy, V. Bouchaud, P. Massot, P. Voisin, N. Koonjoo, D. Moncelet, J.-M. Franconi, E. Thiaudière, and P. Mellet, *PLoS One* **8**, e57946 (2013).
- 34 J. Liebmam, J. Bourg, C. Murali Krishna, J. Glass, J. A. Cook, and J. B. Mitchell, *Life Sci.* **54**, PL503 (1994).
- 35 B. C. Dollmann, A. L. Kleschyov, V. Sen, V. Golubev, L. M. Schreiber, H. W. Spiess, K. Münnemann, and D. Hinderberger, *ChemPhysChem* **11**, 3656 (2010).
- 36 M. Dharmarwardana, A. F. Martins, Z. Chen, P. M. Palacios, C. M. Nowak, R. P. Welch, S. Li, M. A. Luzuriaga, L. Bleris, B. S. Pierce, A. D. Sherry, and J. J. Gassensmith, *Mol. Pharmaceutics* **15**, 2973 (2018).
- 37 K.-i. Matsumoto, M. C. Krishna, and J. B. Mitchell, *J. Pharmacol. Exp. Ther.* **310**, 1076 (2004).
- 38 V. Afzal, R. C. Brasch, D. E. Nitecki, and S. Wolff, *Invest. Radiol.* **19**, 549 (1984).
- 39 J. T. Paletta, M. Pink, B. Foley, S. Rajca, and A. Rajca, *Org. Lett.* **14**, 5322 (2012).
- 40 I. A. Kirilyuk, A. A. Bobko, S. V. Semenov, D. A. Komarov, I. G. Irtegora, I. A. Grigor'ev, and E. Bagryanskaya, *J. Org. Chem.* **80**, 9118 (2015).
- 41 E. A. Legenzov, S. Muralidharan, L. B. Woodcock, G. R. Eaton, S. S. Eaton, G. M. Rosen, and J. P. Y. Kao, *Bioconjugate Chem.* **27**, 2923 (2016).

- ⁴²R. D. Bates, E. H. Poindexter, and B. E. Wagner, *J. Chem. Phys.* **59**, 3031 (1973).
- ⁴³K. Meise, W. Müller-Warmuth, and H.-W. Nientiedt, *Ber. Bunsenges. Phys. Chem.* **80**, 584 (1976).
- ⁴⁴R. D. Bates and W. S. Drozdowski, *J. Chem. Phys.* **67**, 4038 (1977).
- ⁴⁵M. J. Prandolini, V. P. Denysenkov, M. Gafurov, B. Endeward, and T. F. Prisner, *J. Am. Chem. Soc.* **131**, 6090 (2009).
- ⁴⁶M. Gafurov, S. Lyubanova, V. Denysenkov, O. Ouari, H. Karoui, F. Le Moigne, P. Tordo, and T. Prisner, *Appl. Magn. Reson.* **37**, 505 (2010).
- ⁴⁷M. Bennati, C. Luchinat, G. Parigi, and M.-T. Türke, *Phys. Chem. Chem. Phys.* **12**, 5902 (2010).
- ⁴⁸O. Haze, B. Corzilius, A. A. Smith, R. G. Griffin, and T. M. Swager, *J. Am. Chem. Soc.* **134**, 14287 (2012).
- ⁴⁹Y. Matsuki, T. Maly, O. Ouari, H. Karoui, F. Le Moigne, E. Rizzato, S. Lyubanova, J. Herzfeld, T. Prisner, P. Tordo, and R. G. Griffin, *Angew. Chem., Int. Ed.* **48**, 4996 (2009).
- ⁵⁰J. M. Franck, A. Pavlova, J. A. Scott, and S. Han, *Prog. Nucl. Magn. Reson. Spectrosc.* **74**, 33 (2013).
- ⁵¹J. S. Hyde, J. C. W. Chien, and J. H. Freed, *J. Chem. Phys.* **48**, 4211 (1968).
- ⁵²B. D. Armstrong and S. Han, *J. Chem. Phys.* **127**, 104508 (2007).
- ⁵³A. Abragam, *Principles of Nuclear Magnetism* (Clarendon Press, 1961).
- ⁵⁴R. E. Richards and J. W. White, *Proc. R. Soc. London, Ser. A* **283**, 459 (1965).
- ⁵⁵M. D. Lingwood, I. A. Ivanov, A. R. Cote, and S. Han, *J. Magn. Reson.* **204**, 56 (2010).
- ⁵⁶B. L. Bales, *Spin Labeling* (Springer, Boston, 1989), pp. 77–130.
- ⁵⁷M. P. Ferroud-Plattet, E. Belorizky, Y. Berchadsky, and P. Tordo, *Ber. Bunsenges. Phys. Chem.* **96**, 1851 (1992).
- ⁵⁸P. Knowles, M. Derek, and H. Rattle, *Magnetic Resonance of Biomolecules: An Introduction to the Theory and Practice of NMR and ESR in Biological Systems* (Wiley-Interscience, London, 1976).
- ⁵⁹M. Miyake, S. R. Burks, J. Weaver, P. Tsai, W. Liu, D. Bigio, K. S. Bauer, K. J. Liu, G. M. Rosen, and J. P. Y. Kao, *J. Pharm. Sci.* **99**, 3594 (2010).
- ⁶⁰M.-T. Türke and M. Bennati, *Phys. Chem. Chem. Phys.* **13**, 3630 (2011).
- ⁶¹C. Polyon, D. J. Lurie, W. Youngdee, C. Thomas, and I. Thomas, *J. Phys. D: Appl. Phys.* **40**, 5527 (2007).
- ⁶²K.-i. Yamada, Y. Kinoshita, T. Yamasaki, H. Sadasue, F. Mito, M. Nagai, S. Matsumoto, M. Aso, H. Suemune, K. Sakai, and H. Utsumi, *Arch. Pharm.* **341**, 548 (2008).
- ⁶³A. A. Bobko, I. A. Kirilyuk, N. P. Gritsan, D. N. Polovyanenko, I. A. Grigor'ev, V. V. Khramtsov, and E. G. Bagryanskaya, *Appl. Magn. Reson.* **39**, 437 (2010).
- ⁶⁴S. A. Dobrynin, Y. I. Glazachev, Y. V. Gatilov, E. I. Chernyak, G. E. Salnikov, and I. A. Kirilyuk, *J. Org. Chem.* **83**, 5392 (2018).
- ⁶⁵T. Yamasaki, F. Mito, Y. Ito, S. Pandian, Y. Kinoshita, K. Nakano, R. Murugesan, K. Sakai, H. Utsumi, and K.-i. Yamada, *J. Org. Chem.* **76**, 435 (2011).
- ⁶⁶J. Naganuma, Y. Yamazaki, and H. Gotoh, *Struct. Chem.* **30**, 2085 (2019).
- ⁶⁷S. Dobrynin, S. Kutseikin, D. Morozov, O. Krumkacheva, A. Spitsyna, Y. Gatilov, V. Silnikov, G. Angelovski, M. K. Bowman, I. Kirilyuk, and A. Chubarov, *Molecules* **25**, 1709 (2020).
- ⁶⁸J. R. Biller, V. Meyer, H. Elajaili, G. M. Rosen, J. P. Y. Kao, S. S. Eaton, and G. R. Eaton, *J. Magn. Reson.* **212**, 370 (2011).
- ⁶⁹W. Youngdee, G. Planinsic, and D. J. Lurie, *Phys. Med. Biol.* **46**, 2531 (2001).
- ⁷⁰F. Hyodo, K.-i. Matsumoto, A. Matsumoto, J. B. Mitchell, and M. C. Krishna, *Cancer Res.* **66**, 9921 (2006).
- ⁷¹W. R. Couet, R. C. Brasch, C. Sosnovsky, J. Lukszo, I. Prakash, C. T. Gnewech, and T. N. Tozer, *Tetrahedron* **41**, 1165 (1985).
- ⁷²E. G. Rozantsev, B. J. Hazzard, and H. Ulrich, *Free Nitroxyl Radicals* (Plenum Press, New York, 1970).
- ⁷³M. Y. Ivanov, S. A. Prikhod'ko, N. Y. Adonin, I. A. Kirilyuk, S. V. Adichtchev, N. V. Surovtsev, S. A. Dzuba, and M. V. Fedin, *J. Phys. Chem. Lett.* **9**, 4607 (2018).
- ⁷⁴B. L. Bales, M. M. Bakirov, R. T. Galeev, I. A. Kirilyuk, A. I. Kokorin, and K. M. Salikhov, *Appl. Magn. Reson.* **48**, 1399 (2017).
- ⁷⁵A. A. Gorodetsky, I. A. Kirilyuk, V. V. Khramtsov, and D. A. Komarov, *Magn. Reson. Med.* **76**, 350 (2016).
- ⁷⁶S. A. Dobrynin, Y. V. Khoroshunova, and I. A. Kirilyuk, RU patent No. 2702331 (2019).

Erratum to publication 4

Erratum: “The effects of nitroxide structure upon ^1H Overhauser dynamic nuclear polarization efficacy at ultralow-field” [J. Chem. Phys. 155, 144203 (2021)]

Cite as: J. Chem. Phys. 156, 089901 (2022); doi: 10.1063/5.0085601

Submitted: 18 January 2022 • Accepted: 25 January 2022 •

Published Online: 23 February 2022











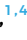


View Online



Export Citation



CrossMark

Paul Fehling,¹  Kai Buckenmaier,^{1,a)}  Sergey A. Dobrynin,²  Denis A. Morozov,²  Yuliya F. Polienko,² 
Yulia V. Khoroshunova,^{2,3}  Yulia Borozdina,¹  Philipp Mayer,¹  Jörn Engelmann,¹  Klaus Scheffler,^{1,4} 
Goran Angelovski,^{1,5}  and Igor A. Kirilyuk² 

AFFILIATIONS

¹Max Planck Institute for Biological Cybernetics, 72076 Tübingen, Germany

²N. N. Vorozhtsov Institute of Organic Chemistry SB RAS, 630090 Novosibirsk, Russia

³Novosibirsk State University, 630090 Novosibirsk, Russia

⁴Department for Biomedical Magnetic Resonance, University of Tübingen, 72074 Tübingen, Germany

⁵Laboratory of Molecular and Cellular Neuroimaging, International Center for Primate Brain Research (ICPBR), Center for Excellence in Brain Science and Intelligence Technology (CEBSIT), Chinese Academy of Sciences (CAS), Shanghai 200031, People's Republic of China

^{a)} Author to whom correspondence should be addressed: kai.buckenmaier@tuebingen.mpg.de

<https://doi.org/10.1063/5.0085601>

In the original article,¹ we present characteristic parameters of the Overhauser dynamic nuclear polarization (ODNP)-efficacy of 27 nitroxide radical samples.

A typing error in a MATLAB-script led to an incorrect scaling factor, affecting the parameters E_{\max} , $P_{1/2}$, and $\xi \cdot s_{\max} \cdot E_{\max}$ and $\xi \cdot s_{\max}$ have to be increased by a factor of ~ 1.5 compared to the previously presented values, while $P_{1/2}$ is only slightly affected ($\sim 3\%$ change). Due to limited RF-power, the fit model did not converge for compounds **B1** and **B2**. Only a lower bound for the corresponding parameters could be estimated.

A quantitative inspection of the corrected values reveals that the losses in our setup/samples are much lower than previously assumed. The agreement of the corrected E_{\max} values with calculations described in the literature^{2,3} is improved after revision.

Since all values for these parameters are equally affected, the qualitative analysis, discussion, and conclusion of the publication remain valid.

The following list specifies the passages of the original article that contain erroneous values, along with the

respective corrections. The revised versions of [Tables I and II](#) and [Fig. 2](#) of the original publication are presented below.

- (i) On p. 5 (section titled RESULTS AND DISCUSSION), regarding compound **M6dn**, “($E_{\max} = -126.2$)” must be replaced by “($E_{\max} = -191.1$).”
- (ii) On p. 5 (section titled RESULTS AND DISCUSSION), regarding TEMPO (**M4**), “ $|E_{\max}|$ of 101.9” must be replaced by “ $|E_{\max}|$ of 153.7.”
- (iii) On p. 5 (section titled RESULTS AND DISCUSSION), regarding PCA (**M7**), “ $P_{1/2}$ of 5.3 W” must be replaced by “ $P_{1/2}$ of 5.4 W.”
- (iv) On p. 6 (section titled Neighboring substituents to the nitroxide group), the sentence “Only **E4** ($P_{1/2} = 6.2$ W) has a lower $P_{1/2}$ than **M6** ($P_{1/2} = 7.1$ W).” must be replaced by “Only **E4** ($P_{1/2} = 6.4$ W) has a lower $P_{1/2}$ than **M6** ($P_{1/2} = 7.2$ W).”
- (v) On p. 6 (section titled Neighboring substituents to the nitroxide group), the passage “ $P_{1/2} = 4.8$ W of **C1**[...]” must be replaced with “ $P_{1/2} = 4.9$ W of **C1**[...]”.

TABLE I. Spin probe properties and characterization results. For their chemical structures, refer to Fig. 1.

	$B_{p,RF}$ (mT)	f		$P_{1/2}$ (W)		E_{max}		$\xi \cdot s_{max}$		$FWHM$ (μ T)		MW (g/mol)
M1	2.27	0.81	± 0.01	6	± 0.2	-154.6	± 13.4	0.292	± 0.025	54	± 0.6	140.2
M2	2.27	0.73	± 0.01	4.8	± 0.1	-166.1	± 6.7	0.346	± 0.015	44.7	± 0.5	142.2
M3	2.14	0.78	± 0.01	3.9	± 0.2	-165.7	± 10	0.326	± 0.02	39.9	± 0.6	144.2
M4	2.12	0.73	± 0.01	6.2	± 0.3	-153.7	± 5.6	0.321	± 0.012	55.1	± 0.6	156.3
M5	2.30	0.82	± 0.01	4.9	± 0.2	-134.6	± 12.3	0.252	± 0.023	47	± 0.5	158.2
M6	2.15	0.74	± 0.01	7.2	± 0.3	-138.7	± 6.8	0.284	± 0.014	61.9	± 0.9	172.2
M7	2.28	0.74	± 0.01	5.4	± 0.2	-134.4	± 5.7	0.277	± 0.012	50.6	± 0.6	185.2
M8	2.14	0.75	± 0.01	6.2	± 0.3	-117.7	± 6.7	0.24	± 0.014	60.1	± 1	200.3
M9	2.30	0.71	± 0.02	4.4	± 0.2	-102.9	± 4.1	0.222	± 0.01	48.6	± 1.1	228.2
M4d	2.13	0.74	± 0.02	4.7	± 0.2	-178.2	± 8.3	0.368	± 0.019	43.6	± 0.5	174.4
M6n	2.64	0.74	± 0.02	5.6	± 0.2	-163	± 11.5	0.336	± 0.025	58.5	± 0.8	173.2
M6d	2.15	0.74	± 0.02	4.2	± 0.2	-161.2	± 5	0.334	± 0.012	40.6	± 0.4	188.3
M6dn	2.64	0.7	± 0.02	3.7	± 0.2	-191.1	± 6.8	0.416	± 0.019	38.6	± 0.4	189.3
M9n	2.75	0.75	± 0.01	3.1	± 0.2	-131.9	± 5.6	0.268	± 0.012	47.5	± 2.3	229.2
M9d	2.29	0.74	± 0.01	2.8	± 0.1	-117.8	± 8.8	0.242	± 0.018	36.7	± 5.9	242.3
M9dn	2.74	0.65	± 0.01	1.1	± 0.1	-123.3	± 2	0.29	± 0.006	37.3	± 0.9	243.3
E1	2.40	0.71	± 0.02	9.5	± 0.6	-96.7	± 3.5	0.207	± 0.009	117.2	± 11	228.4
E2	2.37	0.77	± 0.01	8.2	± 0.4	-96.3	± 3.1	0.193	± 0.007	104.3	± 4.8	241.3
E3	2.42	0.76	± 0.02	10.9	± 0.9	-81.2	± 4.8	0.164	± 0.011	130.1	± 10.1	258.4
E3d	2.42	0.83	± 0.01	9.2	± 0.4	-98.6	± 5.6	0.181	± 0.01	75.7	± 1.4	269.4
E4	2.36	0.74	± 0.01	6.4	± 0.3	-114.5	± 4.6	0.236	± 0.01	62.1	± 2.8	342.5
C1	2.30	0.7	± 0.01	4.9	± 0.3	-105.9	± 10.2	0.231	± 0.022	74.1	± 4.7	212.3
C2	2.39	0.81	± 0.01	8.2	± 0.4	-82.2	± 7.8	0.157	± 0.015	94	± 2.4	280.3
B1 ^a	3.66	0.69	± 0.11	$\gg 15$	\dots	< -10	\dots	\dots	\dots	> 700	\dots	458.7
B2 ^a	3.22	0.76	± 0.07	$\gg 15$	\dots	< -8	\dots	\dots	\dots	> 500	\dots	462.7
B3	2.29	0.7	± 0.03	17.7	± 0.7	-86.2	± 3.5	0.189	± 0.011	76.5	± 1.8	630.8

^aDue to strong inhomogeneous line broadening, or insufficient RF-power, the fit model did not converge for these compounds. Only a lower bound for the corresponding parameters could be estimated, and no standard error could be derived from the fit.

(vi) On p. 7 (section titled Heterocyclic ring structure), the sentence “The unmodified tetramethyl pyrrolidines exhibit $P_{1/2} \leq 5.3$ W and $FWHM \leq 51$ μ T, while the structurally similar piperidines all have $P_{1/2} \geq 6.1$ W and $FWHM \geq 55$ μ T. Similarly, $P_{1/2} \leq 3.1$ W was observed for all perdeuterated and/or ¹⁵N-labeled pyrrolidines and $P_{1/2} \geq 3.5$ W was observed for

all perdeuterated and/or ¹⁵N-labeled piperidines.” must be replaced by “The unmodified tetramethyl pyrrolidines exhibit $P_{1/2} \leq 5.4$ W and $FWHM \leq 51$ μ T, while the structurally similar piperidines all have $P_{1/2} \geq 6.2$ W and $FWHM \geq 55$ μ T. Similarly, $P_{1/2} \leq 3.1$ W was observed for all perdeuterated and/or ¹⁵N-labeled pyrrolidines and $P_{1/2} \geq 3.7$ W was observed for all perdeuterated and/or ¹⁵N-labeled piperidines.”

(vii) On p. 6 (section titled Monoradical vs biradical), the passage “the biradicals **B1** and **B2** show $P_{1/2}$ greater than 60 W” must be replaced with “the biradicals **B1** and **B2** have $P_{1/2}$ much greater than 15 W.”

(viii) On p. 6 (section titled Monoradical vs biradical), regarding compound **B3**, “a $P_{1/2}$ value of 16.5 W” must be replaced by “a $P_{1/2}$ value of 17.7 W.”

(ix) On p. 9 (section titled Precision of measurements), the sentence “The statistical errors (standard deviation) of those repeated measurements were between ± 2.1 and ± 13 for E_{max} , ± 0.05 and ± 0.41 W for $P_{1/2}$, and ± 0.53 and ± 1.21 μ T for $FWHM$.” must be replaced with “The statistical errors (from the standard deviation) of those repeated measurements were between ± 3.9 and ± 14.3 for E_{max} , ± 0.06 and ± 0.40 W for $P_{1/2}$, and ± 0.53 and ± 1.21 μ T for $FWHM$.”

TABLE II. Improvement of ODNF properties of the ¹⁵N-labeled and/or (per)deuterated compounds. The improvement is displayed as a change compared to their conventional counterparts in percent.

	$FWHM$	$P_{1/2}$	E_{max}
M4d	-21	-24	16
M6n	-5	-22	18
M6d	-34	-42	16
M6dn	-38	-49	38
M9n	-2	-30	28
M9d	-24	-36	14
M9dn	-23	-75	20
E3d	-42	-16	21

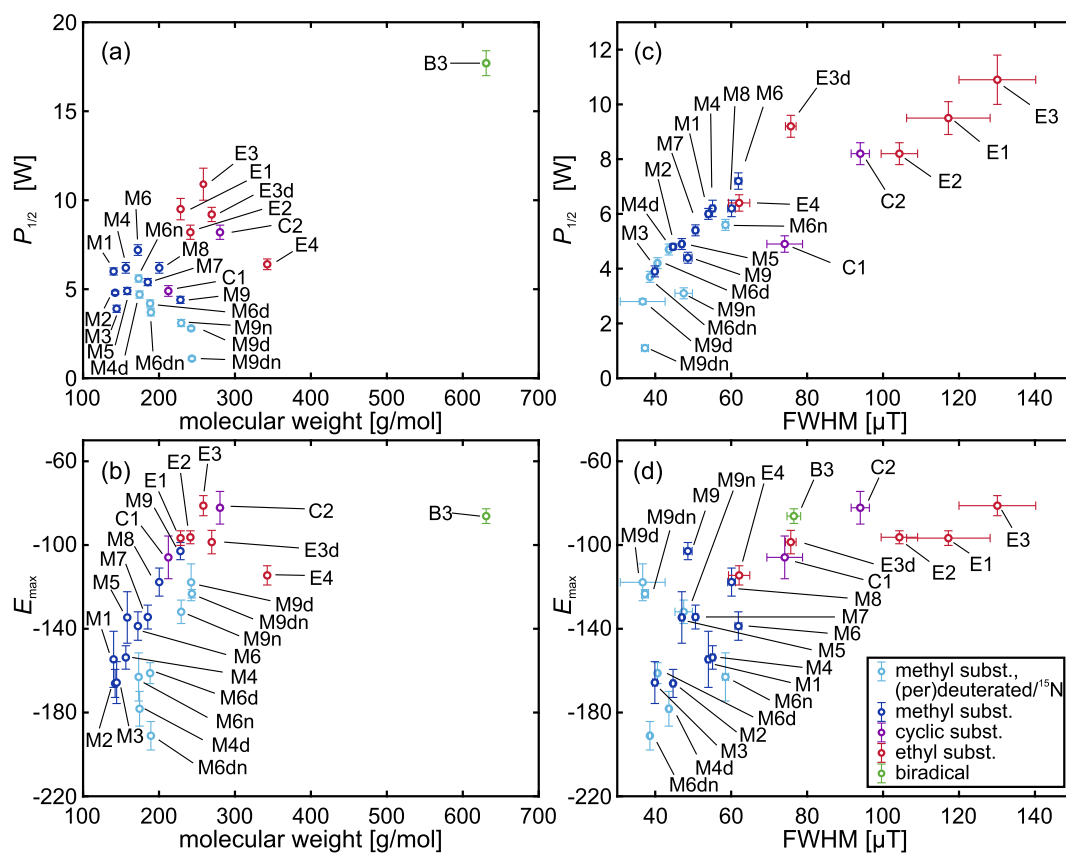


FIG. 2. Efficiency of the different groups of spin probes: (a) $P_{1/2}$ vs molecular weight (MW), (b) E_{\max} vs MW, (c) $P_{1/2}$ vs FWHM, and (d) E_{\max} vs FWHM, measured at the first peak of the ODNP spectrum. For assignment and structures of the compounds, refer to Fig. 1.

REFERENCES

¹P. Fehling, K. Buckenmaier, S. A. Dobrynin, D. A. Morozov, Y. F. Polienko, Y. V. Khoroshunova, Y. Borozdina, P. Mayer, J. Engelmann, K. Scheffler, G. Angelovski, and I. A. Kirilyuk, *J. Chem. Phys.* **155**, 144203 (2021).

²T. Guiberteau and D. Grucker, *J. Magn. Reson. Ser. B* **110**, 47 (1996).

³C. Polyon, D. J. Lurie, W. Youngdeed, C. Thomas, and I. Thomas, *J. Phys. D: Appl. Phys.* **40**, 5527 (2007).